Towards a Measurement of the Electric Dipole Moment of ^{223}Rn

by

Eric R. Tardiff

A dissertation submitted in partial fulfillment
of the requirements for the degree of
Doctor of Philosophy
(Physics)
in The University of Michigan
2009

Doctoral Committee:

Professor Timothy E. Chupp, Chair
Professor Emeritus Henry C. Griffin
Professor Wolfgang B. Lorenzon
Associate Professor Finn Larsen
Assistant Professor Aaron E. Leanhardt

ACKNOWLEDGEMENTS

Many people aided me in the work contained in this thesis. First among these is my advisor, Tim, whose patience and guidance is infused in all of the work presented here and has been much appreciated. Professor Lorenzon has been almost a second advisor to me, providing insightful feedback on my analysis techniques and invaluable assistance in the Stony Brook runs. Sarah Nuss-Warren was my partner in the early development and measurements, and was a pleasure to work with. Matt Pearson and John Behr were instrumental in the work done at both TRIUMF and Stony Brook, and were constant sources of laboratory know-how. The Stony Brook measurements couldn't have been done without the Nuclear Structure Laboratory students and staff: Gene Sprouse, Georgi Rainovski, Richard Lefferts, Jerry Sell, and Kerim Gulyuz really went beyond the call of duty. Along with Matt and John, the TRIUMF transfer studies were aided by Carl Svensson, Mike Hayden, Tim Warner, Gene Hackman, and Gordon Ball.

Others had little to no direct influence on the studies contained in this thesis but are no less deserving of thanks for their intangible contributions. Robert Cooper put up with years of psychological abuse, but always gave almost as good as he got. Behzad Ebrahimi's impenetrable accent never deterred him from talking my ear off about something or other. Hao Fu's visits to my office were always a welcome occasion, even when he just stared out the window for a bit and left again. Claudiu Genes and Monisha Sharma made the office a little more interesting each in their

own inimitable ways. Nick, Agi, and Dylan always gave me a place to crash when I needed to get out of Michigan. Brenton Knuffman was gracious enough to take a shot at helping me get the external cavity to work right. Since I seem to be thanking practically everyone I've ever met, I might as well add to the list: my parents; the Ann Arbor Royals, Astros, and Orioles; the awkward turtles; everyone I've played soccer, softball, or flag football with; and Louis Deslauriers. If I've forgotten anyone, I apologize, and please know that there is a piece of you in my heart always.

TABLE OF CONTENTS

LIST OF FIGURES

Figure

LIST OF TABLES

Table

CHAPTER I

Introduction

1.1 Motivation

It has been demonstrated that any Lorentz-invariant quantum field theory constructed with a Hermitian Hamiltonian must be invariant under the CPT transformation [Pes95]. This property of quantum field theories is referred to as the CPT theorem. The CPT transformation is the combination of three discrete symmetries: charge conjugation, C, transforms particles into their antiparticles; parity transformation, P, is a mirror transformation that acts on spacetime as $(t, \mathbf{x}) \rightarrow (t, -\mathbf{x})$; and time reversal, T, reverses the directions of all momenta and spins by acting on spacetime as $(t, \mathbf{x}) \rightarrow (-t, \mathbf{x})$ and reverses the initial and final states. These symmetries are conserved by all observed interactions mediated by the strong and elecromagnetic forces. The weak interaction appears to act only on left-handed particles, and the theory constructed to describe this interaction (the Glashow-Weinberg-Salam theory) maximally violates both C and P such that CP and T (and thus CPT) are conserved. CP-violation has been observed in the kaon and B-meson systems, a phenomenon that can be described through the Cabibbo-Kobayashi-Maskawa (CKM) matrix formalism. The CKM matrix contains mixing angles for the probability that one flavor of fermion will transform into another during some process, and it can

accommodate a CP-violating phase δ_{CKM}. This phase cannot be derived from any other fundamental parameters and instead its magnitude is determined from the amount of experimentally observed CP-violation. A global fit to all experimental data performed by the CKMfitter group found the value $\delta_{CKM} = 1.08^{+0.17}_{-0.21}$ radians [Cha05].

The importance of CP-violation to the process of baryogenesis was first noted by Sakharov [Sak67]. One would expect that, given symmetric interactions between particles, equal amounts of matter and antimatter would have been created after the big bang. Collisions between particles and their antiparticles would annihilate the same percentage of both, such that equal amounts of matter and antimatter would exist in the universe. All astronomical observations indicate that the visible universe consists of matter, a condition which could result from some amount of CP violation in fundamental interactions. As the amount of CP violation necessary to account for that observed in the kaon and B-meson systems is not sufficient to account for the amount of matter in the universe, there should be other systems that will violate CP symmetry through an independent mechanism.

Permanent electric dipole moments (EDMs) were first proposed by Purcell and Ramsey [Pur50] as a possible result of P-violating interactions, but an EDM would also violate T, and by the CPT theorem would thus violate CP symmetry. The CP violation in the CKM matrix can produce EDMs in fundamental particles, nucleons, atoms, and molecules, but these systems could be sensitive to a wide range of other, hypothetical CP-violating interactions as well. Thus, any measurement of an EDM above the tiny Standard Model (SM) background would be evidence of new physics. EDM searches in various systems have been undertaken since they were first proposed in 1950, but thus far they have all obtained null results. The upper limits on

EDMs continue to improve, leading to stricter limits on the possibilities for extensions to the SM. Further, as the limits continue to move toward the SM background, the probability of obtaining a non-zero result (given the theoretical motivation for additional sources of CP violation) in a more-sensitive measurement would seem to improve. The absence of an EDM above the SM background could require the reconsideration of the theoretical motivation for EDMs, and would severely restrict the possibilities for extensions to the SM.

One EDM experiment with potential for discovery is the Radon EDM experiment under development for measurements starting in 2010/11 at the TRI-University Meson Facility (TRIUMF) in Vancouver, BC. This experiment will use nuclear magnetic resonance (NMR) techniques coupled with gamma-ray or beta radiation detection, utilizing the anisotropy of radiation emitted by polarized nuclei to measure their precession frequency. Any difference in the precession frequency with the orientation of a large electric field applied parallel or anti-parallel to the magnetic field would be an EDM signal. Beyond the advantages of the high precision possible in atomic physics measurements, some isotopes of radon (such as ^{223}Rn) are expected to exhibit nuclear deformations that would enhance the effects of fundamental CP-violating interactions. This results in a sensitivity to those interactions a factor of 400-600 times that of ^{199}Hg [Spe97, Fla03], for which the current best-limit on an EDM exists.

1.2 Summary of Thesis

In anticipation of radon production at TRIUMF, we have undertaken a series of studies meant to investigate aspects of the design and expected sensitivity of the apparatus. TRIUMF will produce the radon in the form of a beam, so we will need to be able to collect a sample over a period of time, then efficiently transfer it to a

measurement cell. We have completed the following:

- We designed a system, consisting of a thin collection foil and a cryopump- and nitrogen-jet-based gas transfer apparatus, and tested it at TRIUMF using ^{120}Xe in August 2003.
- We performed a series of polarization measurements from 2004 to 2006 using ^{209}Rn at SUNY Stony Brook to extract information on radon relaxation rates that would enable us to estimate the achievable EDM sensitivity of our measurement technique.
- In order to remove some of the theoretical uncertainty from the model used to analyze this radon polarization data, in 2007 we measured the rubidium polarization in the optical pumping cells used at Stony Brook under similar experimental conditions.
- Finally, we constructed a narrow-band laser that should allow improved rubidium (and thus radon) polarization and used it to investigate the temperature dependence of ^{129}Xe and ^{131}Xe polarization signals. As ^{131}Xe and ^{209}Rn experience the same types of relaxation mechanisms, these preliminary measurements were useful in strengthening the conclusions drawn from the Stony Brook data.

1.2.1 General EDM Theory

We begin this dissertation with an overview of the theoretical motivations and implications of the search for permanent EDMs. Since radon is a diamagnetic system, we emphasize those aspects of the theory with influence on the permanent EDMs of diamagnetic atoms. We discuss the origins of the SM EDM background and the possible contributions from some proposed extensions to the SM: Supersymmetry, left-right symmetry, and multi-Higgs models. We also discuss atomic EDMs

in general in terms of the CP-odd octupole and Schiff moments, and describe how octupole nuclear deformations and/or vibrations can enhance the effect of CP-odd fundamental interactions at the atomic scale.

1.2.2 Radon EDM Experiment Motivation and Design

Following the general foundation laid in Chapter II, Chapter III provides the motivation of the search for a radon EDM in particular, including the details of the octupole enhancements of ^{223}Rn relative to ^{199}Hg. We provide the basic design of the Radon EDM experiment, focusing on the method of polarizing the radon nuclei through spin-exchange collisions with optically pumped rubidium vapor and measuring the precession frequency of the polarized radon atoms in magnetic and electric fields using the anisotropy in the radiation emitted as these polarized nuclei decay. The initial phase of the Radon EDM experiment will use the anisotropy in the radon gamma-ray distribution to determine the precession frequency and thus the EDM.

1.2.3 Xenon Transfer

Chapter IV covers the development and testing of the apparatus dedicated to collecting a radon sample and transferring it to a measurement cell. Our collaborators performed diffusion studies to determine the optimum material for a thin metal collector foil that could be resistively heated to release a noble gas sample. We designed and built a gas transfer system, including a liquid-nitrogen-cooled coldfinger, to cryo-pump the released noble gas into a different volume in the vacuum system. This volume was connected to a purified nitrogen inlet from which a jet of nitrogen gas pushed the noble gas into the measurement cell. We tested this process using ^{120}Xe at TRIUMF, and found that it transferred about 40% of the collected

xenon into the cell. Based on our observations of the deficiencies of this design, improvements have been made to the coldfinger and pushing system that, in studies performed in August of 2008, transferred ^{121}Xe from the foil to the cell with over 90% efficiency.

1.2.4 Rubidium Polarization

In Chapter V, we discuss the rubidium electron spin resonance (ESR) measurements performed to experimentally determine the rubidium polarization in the cells used in the ^{209}Rn polarization measurements. We present a method, adapted from Ref. [Wag89], of calculating the rubidium polarization based on a range of input parameters. Comparison of the results of these calculations to the results of the ESR measurements cause us to conclude that the model does not accurately reflect the observed rubidium polarization. This could be due to uncertainties in the input parameters, or other limiting factors not accounted for in the model, such as imperfectly polarized laser light or skew light effects.

1.2.5 Radon Polarization Measurements and Analysis

Chapter VI contains a discussion of the experimental equipment and techniques used to obtain our ^{209}Rn polarization data, and Chapter VII covers the analysis methods used to study this data. Since TRIUMF cannot yet produce radon, we performed these measurements at the Stony Brook Francium Laboratory, which could produce ^{209}Rn as a decay product of ^{209}Fr. We chose this isotope due to its sensitivity to the same kinds of relaxation processes as ^{223}Rn as well as its similar half-life. We built an apparatus at Stony Brook that allowed us to collect ^{209}Rn samples in a foil, transfer them to an optical pumping cell, polarize them through spin-exchange collisions with laser-polarized rubidium, and measure the $0^\circ/90^\circ$ gamma-

ray anisotropy using a pair of high-purity germanium detectors. These measurements used both coated and uncoated cells (silane-based cell coatings have been shown to improve the polarization lifetimes of noble gases with $I = 1/2$ [Bre00]) at a range of temperatures, which would allow us to extract information on the temperature dependence of the ^{209}Rn relaxation processes.

We construct a theoretical model for the observed ^{209}Rn gamma-ray anisotropies by first solving a set of rate equations that describe the combined effects on the ^{209}Rn sublevel populations of spin-exchange collisions with rubidium atoms, dipole relaxation processes, and quadrupole relaxation processes. Since the quadrupole processes dominate the relaxation of ^{209}Rn polarization, for simplicity we set the dipole relaxation rate to zero. We assume an Arrhenius temperature distribution for the quadrupole relaxation rate. This results in equations for the sublevel populations in terms of the Rb-^{209}Rn spin-exchange cross section, the ^{209}Rn wall-binding energy, the rubidium polarization, the cell temperature, and the infinite-temperature quadrupole relaxation rate. We use the appropriate Clebsch-Gordan coefficients to determine the populations of the parent states of the observed gamma-rays. We insert the results into the gamma-ray angular distribution function corresponding to the spin difference and multipolarity of the transition resulting in the observed gamma ray, obtaining equations for the $0°/90°$ anistropy for the gamma rays of interest in terms of the above parameters.

We used the results from the rubidium ESR measurements for the rubidium polarization at each cell temperature investigated, and performed a grid search over a reasonable range of the parameter space of the three remaining dependent variables. These fits focused on determining the best-fit value of the infinite-temperature quadrupole relaxation rate, as that result would allow us to estimate the achievable

precision of the Radon EDM experiment. Our fits were not able to determine a single best-fit result for the entire range of spin-exchange cross-sections and wall-binding energies considered, but the results did indicate smaller relaxation rates in general for coated cells. If we use the spin-exchange cross section calculated in Ref. [Wal89] and the wall-binding energy measured in Ref. [Wu90] for ^{131}Xe (which, as a spin-3/2 isotope, is sensitive to the same types of wall interaction as is the spin-5/2 ^{209}Rn), we find infinite-temperature relaxation rates of 0.14 ± 0.02 Hz in uncoated cells and 0.042 ± 0.012 Hz in coated ones. The coated-cell result implies a coherence time that makes an EDM measurement precision on the order of $10^{-26} e \cdot \text{cm}$ achievable. Coupled with the effects of the octupole enhancements, this confirms the potential of the Radon EDM experiment to have an improved sensitivity to CP-violation relative to the ^{199}Hg measurement. Our results could also be used to improve the limits on the multipole mixing ratios of some of the ^{209}Rn gamma rays.

1.2.6 Xenon Polarization Measurements and Analysis

Since ^{131}Xe experiences quadrupole wall interactions while ^{129}Xe does not, we performed a series of polarization measurements using natural xenon in coated and uncoated cells. This allowed us to investigate whether the temperature dependence of the ^{131}Xe polarization was qualitatively consistent with what we observed in ^{209}Rn, and to corroborate our observation that wall coatings appear to be beneficial for isotopes sensitive to quadrupole relaxation processes. Our xenon polarization measurements, performed using an external-cavity narrow-band diode laser, were consistent with our ^{209}Rn results. These measurements could provide the foundation for a more detailed study of the factors influencing the polarization of isotopes experiencing dipole-only and dipole-and-quadrupole relaxation mechanisms.

CHAPTER II

EDM Theory

2.1 Introduction

Here we present an overview of the theoretical motivations and implications of the search for permanent EDMs. We introduce the main hypothetical interactions that could lead to a measurable EDM and summarize their expected magnitudes in the Standard Model (SM). The EDM predictions of beyond-the-standard-model (BTSM) theories demonstrate the utility of EDM experiments in the search for new physics, as these theories allow EDMs at orders of magnitude above that allowed in the SM. As the work described in this thesis was undertaken in preparation for a radon EDM measurement, we discuss these theories with a focus on their application to the physics of atomic EDM generation. Beyond the various EDM-generating interactions that could be present in an atomic system, one must consider the many nuclear interactions that could either enhance or reduce the collective effect of the constituent EDMs.

2.2 EDMs and CP Violation

A permanent EDM in any quantum mechanical system must be aligned with the angular momentum of that system. Otherwise, the EDM would be detectable through the presence of the corresponding quantized states. An EDM, denoted $\mathbf{d}$, is

a polar vector and thus even under time-reversal (T) and odd under space inversion (P) transformations. Angular momentum is an axial vector, however, and so it is T-odd and P-even. As they must be aligned, the expectation values of $\mathbf{d}$ and $\mathbf{J}$ can be related:

$$\langle \mathbf{d} \rangle = g_{\mathbf{d}} \langle \mathbf{J} \rangle . \tag{2.1}$$

Given the behavior of $\mathbf{d}$ and $\mathbf{J}$ under the T- and P-transformations, we see that a nonzero $g_{\mathbf{d}}$ (which implies an nonzero $\langle \mathbf{d} \rangle$) violates T- and P-symmetry. By the CPT theorem [Pes95], a nonzero $\langle \mathbf{d} \rangle$ violates CP symmetry.

In Sakharov's model of baryogenesis [Sak67, Sak91], the matter-antimatter asymmetry in the universe requires CP-violating interactions between fundamental particles. The amount of CP violation discovered thus far is not enough to explain the magnitude of this asymmetry, motivating the continued search for additional CP-odd interactions. An EDM, as a CP-odd observable, must be generated by CP-odd fundamental interactions (which could include interactions independent of those already observed in the SM) and so is seen as a promising avenue in this search.

2.3 Fundamental EDMs in the Standard Model

It is possible to generate EDMs through interactions involving only SM particles, although predictions of the magnitudes of these EDMs are much smaller than those possible in BTSM theories. An EDM-generating lagrangian could contain terms describing the following types of CP-odd interaction: the electron EDM, the quark EDM, the quark chromo-EDM, the theta term, the Weinberg 3-gluon interaction, and CP-odd quark-quark and quark-electron interactions. The BTSM EDM calculations are constructed around these interactions as well, and differ through the inclusion of hypothetical particles and phases in the loop diagrams.

2.3.1 Quark and Electron EDMs

The lagrangian terms for quark and electron EDMs are general CP-odd operators describing an interaction between a quark or an electron with a photon. The EDM operator is [Pos05]

$$\mathcal{L}_{\text{EDM}} = -\frac{\imath}{2} d_i \bar{\psi}_i \sigma_{\mu\nu} \gamma_5 \psi_i F^{\mu\nu}, \tag{2.2}$$

where ψ_i represents the wave function of either the quark or the electron, and d_i parametrizes the strength of the interaction.

2.3.2 Quark CEDM

The quark chromoelectric dipole moment (CEDM) is the strong analogue of the quark EDM, describing a CP-odd interaction between a quark and a gluon. The operator is written as [Pos05]

$$\mathcal{L}_{\text{CEDM}} = -\frac{\imath}{2} d_q^C \bar{q} \sigma_{\mu\nu} \gamma_5 T^a q G^{a\mu\nu}, \tag{2.3}$$

where d_q^C parametrizes the strength of the interaction.

2.3.3 The Theta Term

The only four-dimensional operator in the EDM lagrangian, the theta term describes the vacuum expectation value of the gluon field, written as [Pos05]

$$\mathcal{L}_{\theta_{QCD}} = \bar{\theta} \frac{g_s^2}{32\pi^2} G^a_{\mu\nu} \tilde{G}^{a\mu\nu}. \tag{2.4}$$

Neutron EDM measurements have already provided the limit $\left|\bar{\theta}\right| < 10^{-9}$. The small size of this parameter is the essence of what is known as the strong CP problem. There is no *a priori* reason why the strong force would conserve CP, so a significant amount of theoretical tuning is necessary to result in such a small value for $\left|\bar{\theta}\right|$. Also of note is that this is the only possible source of CP violation in the Standard Model that would not be a result of the Kobayashi-Maskawa mechanism (see Chapter I).

2.3.4 Weinberg's 3-Gluon Operator

Weinberg introduced a CP-odd interaction between three gluons [Wei89],

$$\mathcal{L}_G = \frac{1}{6} d^G f_{abc} G_{a\mu\rho} G^{\rho}_{b\nu} G_{c\lambda\sigma} \epsilon^{\mu\nu\lambda\sigma}, \tag{2.5}$$

where the interaction strength is parametrized by d^G. While this is a six-dimensional operator, unlike the lower-dimensional operators above it has nonzero contributions from two-loop diagrams [Pos94] and so could have an appreciable contribution to an observable EDM.

2.3.5 Quark-Electron and Quark-Quark Interactions

Another set of six-dimensional interactions that must be considered are general CP-odd four-fermion interactions of the form [Pos05]

$$(\bar{\psi}_i \Gamma \psi_i)(\bar{\psi}_j \imath \Gamma \gamma_5 \psi_j), \tag{2.6}$$

where Γ represents the various possible gamma-matrix constructions. These interactions contribute significantly to possible CP-odd interactions in the nucleus and thus must be considered when investigating possible EDMs at the atomic scale.

2.4 SM Order-of-Magnitude EDM Calculations

Unsurprisingly, the most reliable SM EDM calculations to date have been done in the systems wherein the QCD contributions are absent or relatively straightforward, these being the electron, quark, and nucleon EDMs. There is significant uncertainty even in the order of magnitude of SM atomic EDM predictions due to their dependence on nuclear structure.

2.4.1 Electron EDMs

In the Cabbibo-Kobayashi-Maskawa (CKM) model of SM CP-violation, non-vanishing contributions to the electron EDM first appear at the four-loop level,

leading to a theoretical upper limit of $d_e \leq 10^{-38} e \cdot \text{cm}$ [Pos91]. It appears that neutrinos have mass, however, and thus there could be a CP-violating phase in the MNS matrix (the neutrino analogue of the CKM matrix). The largest possible contribution to an electron EDM from this effect allows $d_e \simeq 10^{-33} e \cdot \text{cm}$ [Arc04], but this result requires a fine-tuning of the neutrino masses.

2.4.2 Quark EDMs

It has been discovered that all quark EDMs and CEDMs vanish at the two-loop level [Sha78]. Calculations at the three-loop level, involving diagrams such as that in Fig. 2.1, have found expressions for non-vanishing SM EDMs. The leading-log expression for the down quark EDM is [Cza97]

$$d_d = e \frac{m_d m_c^2 \alpha_s G_F^2 \delta_{\text{CKM}}}{108\pi^5} \ln^2\left(m_b^2/m_c^2\right) \ln\left(M_W^2/m_b^2\right), \tag{2.7}$$

and for the up quark is

$$d_u = -e \frac{m_u m_s^2 \alpha_s G_F^2 \delta_{\text{CKM}}}{216\pi^5} \ln^2\left(m_b^2/m_s^2\right) \ln\left(M_W^2/m_b^2\right). \tag{2.8}$$

Here δ_{CKM} is the CP-violating phase from the CKM matrix, G_F is the Fermi coupling constant, and α_s is the strong interaction coupling. Ref. [Cza97] goes on to make numerical estimates for the quark EDMs, finding $d_d = -0.7 \times 10^{-34} e \cdot \text{cm}$ and $d_u = -0.15 \times 10^{-34} e \cdot \text{cm}$.

2.4.3 Neutron EDMs

Neutron EDMs arise primarily through a CP-odd pion-exchange vertex, as in Fig. 2.2. In terms of the strong-CP parameter θ, $d_n = 3.6 \times 10^{-16} \theta e \cdot \text{cm}$ [Cre79, Cre80]. This relation leads to the experimental limit on θ cited in section 2.3.3. The neutron EDM in the CKM model arises from diagrams like Fig. 2.3, and has been calculated

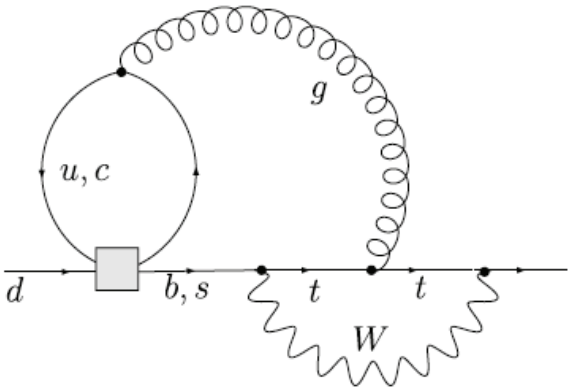

Figure 2.1: A 3-loop diagram contributing to the down-quark EDM, taken from Ref. [Pos05]. An external photon line can be attached to any charged particle in the figure.

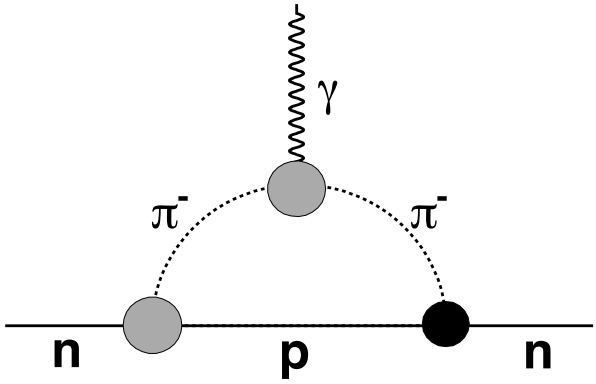

Figure 2.2: A penguin diagram contributing to the neutron EDM [Cre79]. The black circle represents the CP-odd pion-nucleon-nucleon vertex, with CP-violation mediated by θ_{QCD}.

to be $d_n \simeq 2 \times 10^{-32} e \cdot \text{cm}$ [Khr82]. This is about 6 orders of magnitude below the current experimental limit.

2.4.4 Atomic EDMs

Atomic systems, due to the collective effects of the various possible interactions between their constituent particles, involve much more complex calculations than do the electron, quark, and nucleon EDMs. Paramagnetic atoms have an unpaired electron, which implies a strong dependence on the electron EDM. While the Schiff theorem [Sch63] implies that this EDM would be shielded in the lowest-energy config-

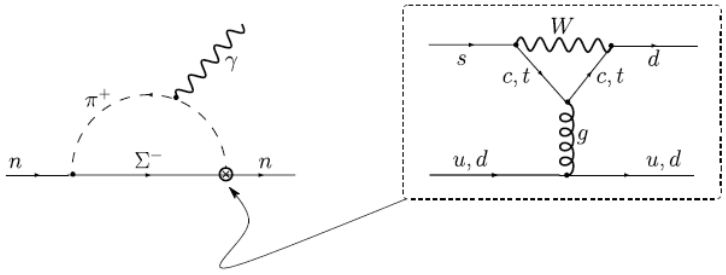

Figure 2.3: A Feynman diagram illustrating the leading SM contribution to the neutron EDM, taken from Ref. [Pos05].

uration, finite-size and relativistic effects overcome that shielding to a certain extent. Diamagnetic atoms (such as ^{199}Hg and ^{223}Rn) have paired electrons, so one expects the effects of the various electron EDMs to cancel each other out. The atomic EDM in this case is generated by CP-odd nuclear forces that contribute to the Schiff moment [Sch63], a measure of the difference between the distribution of charge and dipoles in the nucleus. Octupole effects in large nuclei also serve to enhance the effects of these CP-odd forces. There can be significant variations in the Schiff moments and enhancement factors of different atomic systems, making it difficult to quote a single value for the SM atomic EDM background. We discuss these effects in more detail in section 2.7.

2.5 EDMs in Supersymmetry

Under Supersymmetry (SUSY) [Mar08], a supersymmetric partner is introduced for every standard model particle such that every SM fermion has a corresponding SUSY boson and every SM boson has a SUSY fermion. Along with the myriad new particles that could contribute to the EDM-generating Feynman diagrams, the theory also contains numerous possibly-CP-violating phases. All of the above SM EDM mechanisms would have additional SUSY contributions, but with the number of

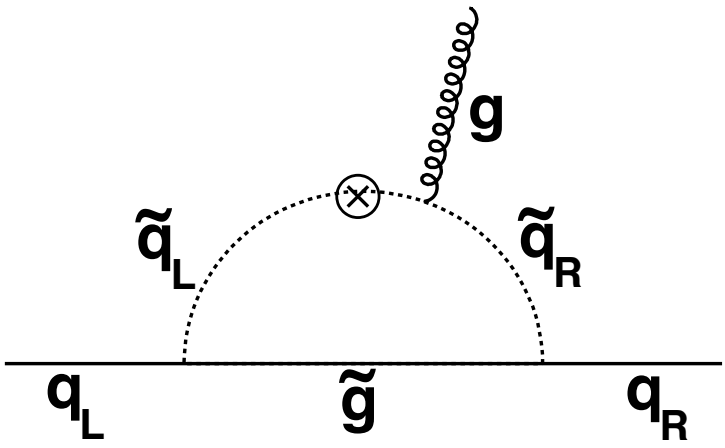

Figure 2.4: A Feynman diagram for a one-loop contribution to the quark CEDM. $\tilde{q}_L$ and $\tilde{q}_R$ are left- and right-handed squarks, $\tilde{g}$ is a gluino, and $\otimes$ represents the insertion of a CP-violating phase.

free parameters in the theory (on the order of 100) SUSY EDM predictions generally span several decades of orders of magnitude.

2.5.1 Quark CEDM Under SUSY

The largest fundamental contribution to the EDM of a diamagnetic atom comes from the quark CEDM [Fal99]. As mentioned above, quark CEDMs in the SM are non-vanishing only at the three-loop level, but SUSY contributions are present at the one-loop level as in Fig. 2.4. It is impossible to cite a specific value for the SUSY quark CEDM prediction due to the many unknown parameters in the theory, but the existence of one-loop contributions implies it could be significantly larger than the SM value.

2.5.2 EDM Limits on SUSY

Experimental values are already well below the maximum possible level, thus providing some restrictions on the allowed SUSY parameter space. Fig. 2.5 shows the limits imposed by experiment on a minimal version of SUSY in which various

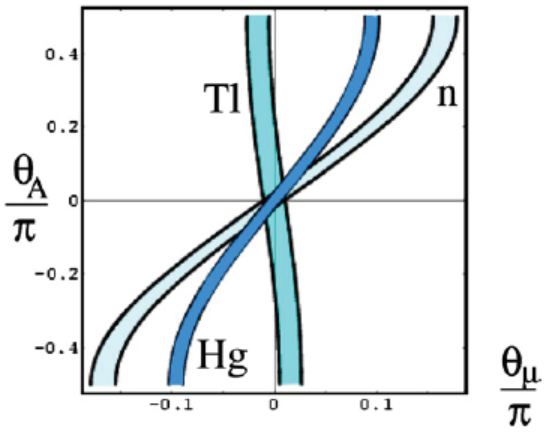

Figure 2.5: The limits on the CP-violating phases in a simplified version of SUSY from the three best, complimentary EDM measurements. Taken from Ref. [Pos05].

assumptions and phase redefinitions result in a SUSY theory with only two CP-violating phases, θ_A and θ_μ. We see that in this version of SUSY the combined restrictions set by the three best EDM measurements to date force the phases to be near $\theta_A = \theta_\mu = 0$. The calculations in Fig. 2.5 assume the characteristic mass scale for symmetry breaking to be $M_{SUSY} = 500$ GeV. A larger M_{SUSY} would weaken the phase restrictions. Thorough explorations of the larger SUSY parameter space in search of regions where the various CP-violating phases would induce effects that would cancel have not found candidates consistent with the EDM data.

In some cases the limit on SUSY from EDM experiments is given in terms of parameters of the type [Bar93]

$$\varepsilon_q^{SUSY} \equiv |A_q/m_{\tilde{g}}^3| \sin\left(\phi_{A_q} - \phi_{\tilde{g}}\right) f(m_{\tilde{q}}/m_{\tilde{g}})^2, \tag{2.9}$$

where ϕ_{A_q} is a phase in the mass parameter coupling left- and right-handed squarks, $\phi_{\tilde{g}}$ is a phase in the gluino mass $m_{\tilde{g}}$, and the function f is $\mathcal{O}(1)$. This parameter can be used to quantify the SUSY contribution to the quark CEDM. Similar parameters are used for the SUSY contribution to the other CP-odd interactions.

2.6 Other BTSM Sources of EDMs

While SUSY is the most popular possible extension to the SM, others have been proposed that predict above-SM-background EDMs. One of these is the reintroduction of a symmetry between left-handed and right-handed interactions. The weak interaction, as observed thus far, maximally violates parity, and the proposed extension introduces heavy right-handed gauge bosons for the weak force that would restore parity conservation above some mass scale. This left-right symmetry implies the existence of left- and right-handed Kobayashi-Maskawa-type mixing matrices, introducing a second CP-violating phase and leading to larger EDMs. A parameter commonly quoted to express the limit an experiment makes on LR models is x^{LR}, defined as [Bar93]

$$x^{LR} \equiv \left(\frac{\sin 2\zeta}{8 \times 10^{-3}}\right) \mathrm{Im}(V_{\mathrm{Lud}} V^*_{\mathrm{Rud}}), \tag{2.10}$$

where ζ is the CP-violating phase that mixes left- and right-handed W bosons and the V's are the appropriate elements of the left- and right-handed CKM matrices. The scalar-pseudoscalar nucleon-nucleon interaction is described by the Hamiltonian [Fis92]

$$\mathcal{H}_{nn} = \eta \frac{G_F}{\sqrt{2}} (\bar{N}\tau N)(\bar{N}\imath\gamma_5\tau N), \tag{2.11}$$

where η parameterizes the strength of the interaction. The relation between x^{LR} and this interaction, which contributes strongly to atomic EDMs, is estimated as [Bar93]

$$\eta \sim (2.7 \times 10^{-1}) x^{LR}. \tag{2.12}$$

Another possible extension is the introduction of multiple Higgs doublets. There could be a CP-violating phase between the doublets, which would allow for more

EDM-contributing Feynman diagrams and thus larger EDM predictions. The parameter quoted in experimental limits on this model is [Bar93]

$$\varepsilon^{Higgs} \equiv \left(\frac{1}{2}\tan\beta\right)^{-1} (f_t \tan^2\beta \ \mathrm{Im}Z_2 - g_t \cot^2\beta \ \mathrm{Im}Z_1), \tag{2.13}$$

where f_t and g_t are functions of m_t^2/m_H^2 of order one (m_t is the top mass and m_H is the mass of the lightest Higgs), $\mathrm{Im}Z_1$ and $\mathrm{Im}Z_2$ are dimensionless parameters describing CP violation in the neutral Higgs propagators, and $\tan\beta$ is the ratio of the Higgs masses. The equation

$$\eta \sim \varepsilon^{Higgs} \tan\beta (9.2 \times 10^{-4}) e \cdot \mathrm{cm} \tag{2.14}$$

connects ε^{Higgs} to the atomic EDM.

2.7 Atomic EDMs

The mechanisms through which CP-violating interactions at the particle scale manifest themselves at the atomic scale require a more detailed discussion here. There are multiple fundamental interactions that could generate a nuclear EDM, and these would translate differently into an atomic EDM for different systems. For certain isotopes, the Schiff moment and octupole nuclear deformations enhance the collective effect of the CP-odd nuclear interactions.

2.7.1 Interactions Generating Nuclear and Atomic EDMs

The flow chart in Fig. 2.6 illustrates the paths through which hypothetical fundamental CP-violating interactions at high energy scales manifest themselves in EDMs at the lower energy scales of the nucleus and atom, where they are measured. We focus here on the generation of EDMs in diamagnetic atoms. As mentioned in the section on EDM order-of-magnitude calculations in the SM, the EDMs of diamagnetic atoms are expressed in terms of the Schiff moment. This is a property of the

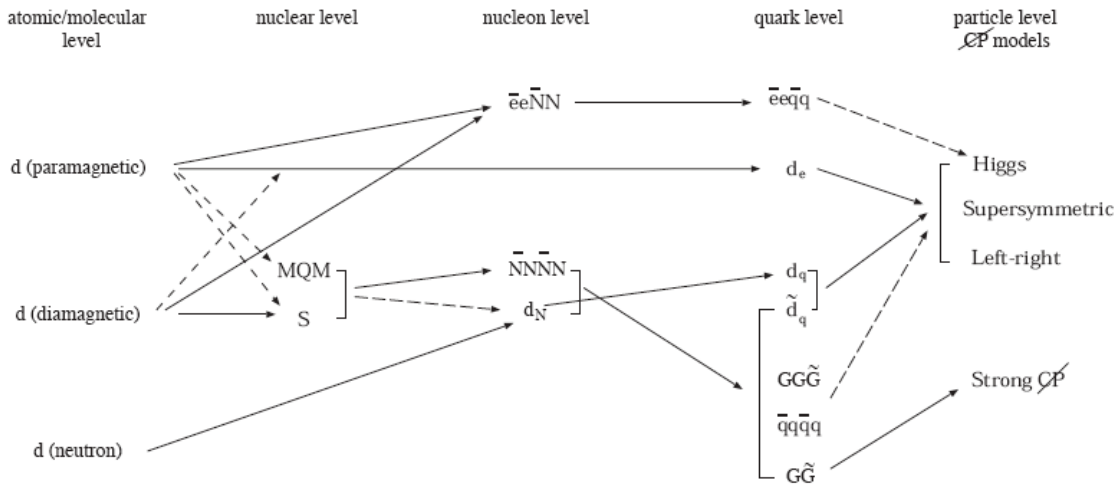

Figure 2.6: The interdependence of CP-violating interactions at different length scales, taken from Ref. [Gin04]. Solid arrows denote dominant contributions.

nucleus describing the difference in the distributions of charge and EDMs that prevents the EDMs of the constituent particles from being screened by their collective arrangement in the nucleus. The Schiff moment must be generated either by CP-odd nuclear interactions or by the EDM of an external nucleon [Pos05]. The collective effects of the CP-odd interactions generally outweigh the contribution of a single nucleon EDM. Since nucleon-nucleon interactions are dominated by pion exchange, an effective interaction with a CP-odd pion-nucleon vertex is introduced in theoretical descriptions of these interactions. The other contribution to diamagnetic-atom EDMs is a possible CP-odd electron-nucleon interaction, which generates an atomic EDM independently of the presence or absence of a nuclear EDM.

The CP-Odd Nucleon-Nucleon Interaction

The coupling constant for the CP-odd pion-nucleon vertex is written $\bar{g}_{\pi NN}$, and has significant contributions from four quark-level CP-odd interactions. These include the quark CEDM, the Weinberg 3-gluon interaction, CP-odd 4-quark inter-

actions, and θ_{QCD}. According to Ref. [Gin04], the quark EDM has no significant contribution to the CP-odd nucleon-nucleon interaction, and it's contribution to the diamagnetic-atom EDM comes through the external-nucleon EDM's contribution to the Schiff moment. Through the corresponding parameters for these CP-odd interactions, diamagnetic atoms are sensitive to all of the models of CP violation discussed in this chapter.

CP-Odd Electron-Nucleon Interactions

There are three main forms a CP-odd interaction between an electron and a nucleon can take, illustrated in the Hamiltonian [Gin04]

$$\mathcal{H} = \frac{G}{\sqrt{2}} \sum_N C^{SP} \bar{N} N \bar{e} \imath \gamma_5 e + C^{PS} \bar{N} \imath \gamma_5 N \bar{e} e + C^T \bar{N} \imath \gamma_5 \sigma_{\mu\nu} N \bar{e} \sigma_{\mu\nu} e, \tag{2.15}$$

where the coefficients C^{SP}, C^{PS}, and C^T parametrize the scalar-pseudoscalar, pseudoscalar-scalar, and tensor nucleon-electron interactions. All of these interactions are induced through CP-odd electron-quark interactions, which can be generated in multi-Higgs models.

2.7.2 The Octupole and Schiff Moments

Consideration of the electrostatic potential of the nucleus, taking into account the screening caused by the atomic electrons, leads to expressions for the octupole and Schiff moments of the nucleus. Both of these aid in the translation of CP-odd interactions at the nucleon level to a CP-odd moment of the nucleus as a whole. This potential can be written as [Spe97]

$$\varphi(\mathbf{R}) = \int \frac{e\rho(\mathbf{r})}{|\mathbf{R}-\mathbf{r}|} \mathrm{d}^3 r + \frac{1}{Z} (\mathbf{d} \cdot \nabla) \int \frac{\rho(\mathbf{r})}{|\mathbf{R}-\mathbf{r}|} \mathrm{d}^3 r, \tag{2.16}$$

where $\rho(\mathbf{r})$ is the nuclear charge density and the nuclear EDM is

$$\mathbf{d} = \int e\mathbf{r}\rho(\mathbf{r}) \mathrm{d}^3 r = \mathrm{d}\frac{\mathbf{I}}{I}. \tag{2.17}$$

Under the assumption of a point-like nucleus, when Eq. 2.16 is expanded in terms of r/R the first non-zero CP-odd term is [Spe97]

$$\varphi^{(3)} = \varphi_{\text{octupole}} + \varphi_{\text{Schiff}}, \tag{2.18}$$

where

$$\varphi_{\text{octupole}} = -\frac{1}{6} O_{ijk} \nabla_i \nabla_j \nabla_k \frac{1}{R} + \frac{1}{e} \frac{1}{2Z} Q_{ij} \left(\mathbf{d} \cdot \nabla\right) \nabla_i \nabla_j \frac{1}{R} \tag{2.19}$$

and

$$\varphi_{\text{Schiff}} = 4\pi \mathbf{S} \cdot \nabla \delta^3 \left(\mathbf{R}\right). \tag{2.20}$$

Here O_{ijk} and Q_{ij} are the nuclear electric octupole and quadrupole moments, respectively. In terms of a perturbation in the atomic states, the EDM generated by $\varphi^{(3)}$ is [Spe97]

$$\mathbf{d}_{atom} = -e\langle\tilde{\psi}|\mathbf{r}|\tilde{\psi}\rangle = -2e \sum_{|k_2\rangle} \frac{\langle k_1|\mathbf{r}|k_2\rangle\langle k_1| - e\varphi^{(3)}|k_2\rangle}{E_{k_1} - E_{k_2}}, \tag{2.21}$$

where $|k_1\rangle$ is the electron ground state and $\{|k_2\rangle\}$ is the set of opposite parity states mixed with the ground state by $\varphi^{(3)}$. The Schiff moment, denoted $\mathbf{S}$, is [Spe97]

$$\mathbf{S} = \frac{1}{10}\left[\int e\rho(\mathbf{r})\mathbf{r}r^2 \mathrm{d}^3 r - \frac{5}{3}\mathbf{d}\frac{1}{Z}\int \rho(\mathbf{r}) r^2 \mathrm{d}^3 r\right] = S\frac{\mathbf{I}}{I}, \tag{2.22}$$

and the octupole moment is [Spe97]

$$O_{ijk} = \int e\rho(\mathbf{r}) \left[r_i r_j r_k - \frac{1}{5} r^2 (r_i \delta_{jk} + r_j \delta_{ik} + r_k \delta_{ij})\right] \mathrm{d}^3 r. \tag{2.23}$$

In general, the octupole moment contributes much less to the atomic EDM than does the Schiff moment. The dominance of the Schiff moment's contribution to an atomic EDM relative to that of the octupole moment is due to the fact that the octupole moment is a rank 3 tensor while the Schiff moment is rank 1. This requires

that the contribution of O_{ijk} to Eq. 2.21 involves electron states with $j \geq 3/2$, which spend less time close to the nucleus than lower-angular-momentum electrons, causing the octupole contribution to be suppressed. The Schiff moment can be calculated in terms of the CP-odd pion-exchange vertex [Pos05], allowing measured atomic EDMs to be connected to the fundamental CP-violating parameters generating that interaction.

2.7.3 Octupole Enhancement

Some nuclei have octupole deformations that can result in an enhancement of the Schiff moment and thus the EDM. The parity doublets created by the existence of CP-odd nuclear moments can be written as [Spe97]

$$\Psi^{\pm} = \frac{1}{\sqrt{2}} \left(|IMK\rangle \pm |IM-K\rangle \right), \tag{2.24}$$

where $\mathbf{I}$ is the nuclear spin, $M = I_z$, and K is the projection of $\mathbf{I}$ along the nuclear axis. In the absence of a CP-odd interaction, the effect of the intrinsic (body-frame) Schiff moment averages out. However, in the presence of a CP-odd interaction the two parity states are mixed, leading to a non-zero time average. The intrinsic Schiff moment in nuclei with octupole deformation can be written as [Spe97]

$$S_{\text{intr}} = eZR_0^3 \frac{9}{20\pi\sqrt{35}} \beta_2 \beta_3, \tag{2.25}$$

where R_0 is the nuclear radius and β_2 and β_3 are the lowest-order deformation parameters. In the presence of a T-, P-odd nuclear potential V^{PT}, the states in Eq. 2.24 mix such that the positive parity state becomes [Spe97]

$$\Psi = \frac{1}{\sqrt{2}} \left[(1+\alpha)|IMK\rangle + (1-\alpha)|IM-K\rangle \right], \tag{2.26}$$

where

$$\alpha = \frac{\langle \Psi^- | V^{PT} | \Psi^+ \rangle}{E^+ - E^-} \tag{2.27}$$

parametrizes the mixing between the two states. The laboratory-frame expectation value for the Schiff moment in the nuclear ground state ($M = K = I$) is

$$\langle \Psi | S | \Psi \rangle = 2\alpha \frac{I}{I+1} S_{\text{intr}}. \tag{2.28}$$

A two-body potential is necessary to completely describe a CP-odd interaction between two nucleons, but for the purposes of estimating the Schiff moment it is unnecessarily complex. An effective one-body potential constructed from the two-body potential describing the CP-odd nucleon-nucleon interaction is given by [Spe97]

$$V^{PT} = -\eta \frac{3G}{8\pi\sqrt{2} m r_0^3} \delta(R_0 - r'), \tag{2.29}$$

where G is the Fermi constant, r_0 is the internucleon distance, and η parametrizes the strength of the potential as in Eq. 2.11. The collective Schiff moment in the laboratory frame can be estimated from this as [Spe97]

$$S \sim \alpha S_{\text{intr}} \sim \frac{0.05 e \beta_2 \beta_3^2 Z A^{2/3} \eta r_0^3}{|E^+ - E^-|}, \tag{2.30}$$

which illustrates the dependence of the Schiff moment on the deformation parameters as well as on the energy splitting between the parity states. Since the Schiff moment is generally considered the dominant contribution to the EDM of diamagnetic atoms, predictions for these EDMs are often given as a simple function of S of the type

$$d = k \times \left(\frac{S}{e \cdot \text{fm}^3} \right) e \cdot \text{cm}. \tag{2.31}$$

The value of k depends on the specific isotope. Different isotopes have different values for the deformation and energy splitting, so one could search for systems which feature largely deformed nuclei coupled with closely-spaced parity states. These systems would have an enhanced sensitivity to CP-violating interactions.

More recent investigations have looked into the possibility that octupole nuclear vibrations could provide an additional enhancement to the sensitivity to CP-odd

forces. These vibrations contribute to the Schiff moment through two proposed mechanisms [Fla03]: mixing between the ground state of an odd-A nucleus with an octupole phonon state (analogous to the mixing of parity states above) and a CP-odd contribution to the valence nucleon wavefunction from the octupole vibrations. While these studies are in their initial stages, the resulting enhancements appear to be comparable to those due to static octupole deformations alone.

2.8 EDM Theory Summary

Diamagnetic atoms are sensitive to a wide range of possible CP-violating interactions. Measurements of their EDMs can be used to place limits on the parameters of many BTSM theories, including SUSY, multi-Higgs models, and LR-symmetric models. Many of the limits on these theories are set by the ^{199}Hg measurement, currently the most precise EDM experiment. As a diamagnetic atom, radon is sensitive to the same CP-violating parameters as mercury. Some isotopes of radon, such as ^{221}Rn and ^{223}Rn, are expected to exhibit octupole deformation and/or vibration and thus their EDMs could be enhanced relative to ^{199}Hg. The details of these enhancements for radon will be presented in section 3.2. Due to this increased sensitivity to CP-odd interactions, EDM measurements in radon are an attractive avenue in the search for a positive signal of CP-violation outside the known CKM effects.

CHAPTER III

The Radon EDM Experiment

3.1 Introduction

An experimental program working towards the measurement of the radon EDM is under way at the TRI-University Meson Facility (TRIUMF) in Vancouver, Canada. As radon is a diamagnetic atom, it is sensitive to the same sources of CP violation as is ^{199}Hg, for which the current best-limit on an atomic EDM exists. Certain isotopes of radon, such as ^{221}Rn and ^{223}Rn, are expected to feature octupole-deformed nuclei which could lead to a significant enhancement to their sensitivity to fundamental CP-violating interactions [Spe97]. These enhancements could be large enough that an EDM experiment with a sensitivity within two orders of magnitude of the ^{199}Hg result would have an improved sensitivity to CP violation. As the observation of a non-zero EDM at the sensitivities currently accessible to experiment would be experimental evidence of beyond the standard model (BTSM) physics, the Radon EDM experiment is an attractive candidate for the discovery of a source of CP violation outside the standard model (SM).

The EDMs of atomic systems can be, and have been [Ros01, Rom01], measured with great sensitivity though nuclear magnetic resonance (NMR) techniques. Since the radon isotopes featuring the greatest potential octupole enhancements are not

naturally occurring, they will be produced at TRIUMF's Isotope Separator and ACcelerator (ISAC) facility. They cannot be produced in quantities large enough to perform standard NMR measurements, however, so we will extract precession frequency data from the angular distribution of the radiation emitted as part of the radon decay process. In the presence of a strong electric field, this precession frequency will have a dependence on the magnitude of both the electric and magnetic dipole moments of the atoms. This will allow us to extract a value for the radon EDM from the measured precession frequencies.

3.2 Radon EDM Enhancements

The magnitude of an atomic EDM (generated by CP-violating fundamental interactions) in a diamagnetic isotope is proportional to the nuclear Schiff moment, which can be enhanced by octupole nuclear deformations (see section 2.7). Calculations of the expected EDM for a variety of isotopes can be found in Table 3.1, taken from Ref. [Spe97]. An important point to note from the table is that there is currently no experimental value for the ^{223}Rn energy splitting. While the ^{223}Rn energy splitting calculations differ greatly for the Woods-Saxon nuclear potential versus the Nilsson potential, comparison of the calculated and experimental energy splittings for the other isotopes indicates that the Woods-Saxon results are usually fairly accurate. This allows for some confidence in the magnitude of the predicted ^{223}Rn EDM value, but we won't be able to determine the enhancement relative to ^{199}Hg with any precision until we measure the energy splitting.

As mentioned in section 2.7, octupole vibrations have been proposed as an additional source of atomic EDM enhancement. Calculations in Ref. [Fla03] found a ^{223}Rn EDM of $3300 \times 10^{-25} \eta e \cdot$ cm due to octupole vibrations, whereas the value of

Table 3.1: Calculations from Ref. [Spe97]. The admixture coefficients α are defined in Eq. 2.27, and η is the coefficient of the potential describing the CP-odd nucleon-nucleon interaction of the type given by Eq. 2.29. Ref. [Spe97] calculated these values for both Woods-Saxon (WS) and Nilsson (Nl) nuclear potentials. The Schiff moment calculations used the WS potential, d is the induced EDM, and the ^{199}Hg and ^{129}Xe values come from Refs. [Fla86] and [Dzu85], respectively.

	^{223}Ra	^{225}Ra	^{223}Rn	^{221}Fr	^{223}Fr	^{225}Ac	^{229}Pa	^{199}Hg	^{129}Xe
$\alpha(WS)(10^7\eta)$	1	2	4	0.7	2	3	34		
$\Delta E(WS)$ (keV)	170	47	37	216	75	49	5		
$\alpha(Nl)(10^7\eta)$	2	5	2						
$\Delta E(Nl)$ (keV)	171	55	137						
ΔE_{expt} (keV)	50.2	55.2		234	160.5	40.1	0.22		
$S_{\text{intr}}(e \cdot \text{fm}^3)$	24	24	15	21	20	28	25		
$S(10^8\eta e \cdot \text{fm}^3)$	400	300	1000	43	500	900	12000	-1.4	1.75
$d(10^{25}\eta e \cdot \text{cm})$	2700	2100	2000	240	2800			5.6	0.47

$2000 \times 10^{-25}\eta e \cdot \text{cm}$ from Table 3.1 depends only on octupole deformation. The parameter η is the coefficient of the one-body potential for the CP-odd nucleon-nucleon interaction given in Eq. 2.27. Compared to the ^{199}Hg value of $5.6 \times 10^{-25}\eta e \cdot \text{cm}$, these results imply enhancement factors of about 600 and 400, respectively. These properties make ^{223}Rn much more sensitive to CP-odd fundamental interactions than is ^{199}Hg, allowing an experiment with a lower sensitivity to radon EDMs to have a higher sensitivity to CP violation. Systems with octupole enhancements are considered good candidates for EDM discovery, but they have the disadvantage that the increased complexity of their nuclear structure makes it more difficult to translate the results of an EDM experiment into limits on the CP-odd fundamental parameters [Pos05]. Other systems, such as ^{223}Ra and ^{223}Fr, have larger octupole enhancement factors than does ^{223}Rn. Noble gases have a proven track record in EDM experiments, however, and can be contained and polarized in measurement cells in a fairly straightforward manner.

The current experimental picture in terms of the limits on fundamental CP-odd parameters set by EDM experiments is illustrated in Table 3.2. As is evident from

Table 3.2: The best upper limit on various CP-odd fundamental parameters and the systems from which they were derived. The parameter η_q is the coefficient of the CP-odd four-quark interaction. For definitions of the rest of these parameters, see Chapter II. A recently announced improvement to the ^{199}Hg result improved some of the limits, as shown.

Parameter	Best Upper Limit	System	Reference
d_n	$6.3 \times 10^{-26} e \cdot \text{cm}$	neutron	[Har99]
d_e	$1.6 \times 10^{-27} e \cdot \text{cm}$	Tl	[Reg02]
d_p (old)	$1 \times 10^{-23} e \cdot \text{cm}$	TlF	[Cho91]
d_p (new)	$7.9 \times 10^{-25} e \cdot \text{cm}$	Hg	[Gri09]
d_d^C (old)	$7 \times 10^{-27} e \cdot \text{cm}$	Hg	[Rom01]
d_d^C (new)	$6 \times 10^{-27} e \cdot \text{cm}$	Hg	[Gri09]
Θ_{QCD}	1.5×10^{-10}	neutron and Hg	[Har99, Rom01]
ε_q^{SUSY}	2×10^{-3}	Hg	[Rom01]
ε^{Higgs}	$0.3/\tan\beta$	Tl	[Reg02]
x^{LR}	1×10^{-3}	Hg	[Rom01]
η	1.6×10^{-3}	Hg	[Jac95]
C^T (old)	1×10^{-8}	Hg	[Rom01]
C^T (new)	1.5×10^{-9}	Hg	[Gri09]
C^S (old)	3×10^{-7}	Hg	[Rom01]
C^S (new)	5.2×10^{-8}	Hg	[Gri09]
η_q	3.4×10^{-6}	Hg	[Jac95]

this, the ^{199}Hg result is the source of the best upper limit on a majority of these parameters. Since ^{223}Rn is also diamagnetic, it is sensitive to the same set of CP-odd parameters as is ^{199}Hg. Thus, if we are able to perform an EDM experiment with enough sensitivity to overcome the increased theoretical complexity of the ^{223}Rn nucleus, we could improve on many of these limits.

3.3 Measuring Atomic EDMs Using NMR Techniques

Atomic physics experiments can measure frequencies with great precision, allowing NMR techniques to be used to measure atomic EDMs at levels competitive with or better than those possible for other species. The procedure for measuring an EDM in this manner begins with polarizing the nuclei of the atoms of interest.

3.3.1 Spin-Exchange Optical Pumping

Samples of noble gas atoms can be polarized through spin-exchange collisions with laser-polarized alkali-metals [Wal97]. Our optical pumping cells (see Fig. 3.1) contain

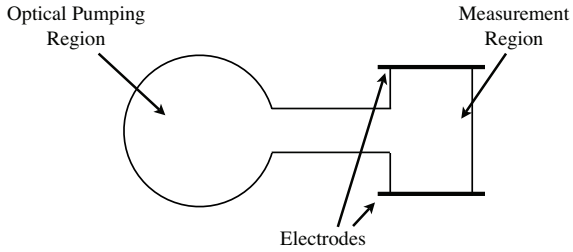

Figure 3.1: A sketch of the relevant features of the cells to be used for a radon EDM measurement. The optical pumping region contains a sample of alkali-metal to permit spin-exchange polarization of radon atoms.

natural rubidium. The final design for these cells has not been set, but, as illustrated in the sketch, they will incorporate an optical pumping region and a measurement region. The optical pumping region will be illuminated by laser light to polarize the radon gas through spin exchange. The measurement region will include electrodes to generate the electric field necessary for the EDM measurements. If we ignore the hyperfine interaction, the rubidium optical pumping process can be described by Fig. 3.2. Circularly polarized light tuned to the ^{85}Rb D1 line (794.8 nm) illuminates the cell, located in a uniform magnetic field. This drives the transition from the $m_j = -1/2$ ground state to the $+1/2$ excited state. The Clebsch-Gordan coefficents are such that, if the rubidium atoms were allowed to undergo spontaneous emission, it would require on average three photon absorptions to transfer one atom to the $+1/2$ ground state. We fill the cells with a buffer of about 1 atm of nitrogen gas. Nitrogen-rubidium collisions mix and quench the excited states, preventing radiation trapping and increasing the optical pumping efficiency. With properly polarized light, high rubidium polarizations can be obtained.

Spin-exchange collisions transfer the rubidium polarization to the noble gas nu-

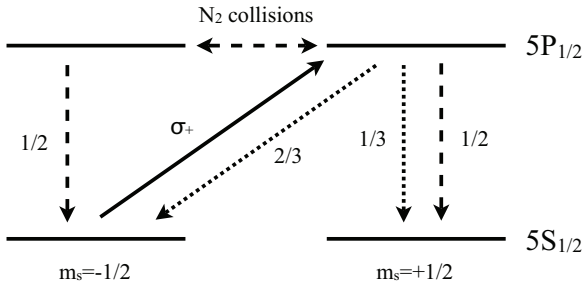

Figure 3.2: An illustration of the optical pumping process for ^{85}Rb, neglecting nuclear spin. Circularly polarized laser light drives the D1 transition and collisions with the buffer gas mix and quench the excited state populations, giving a 50% probability that an electron pumped out of the $m_s = -1/2$ state will end up in the $m_s = +1/2$ state. This increases the efficiency over the Clebsch-Gordan coefficients by a factor of 1.5.

cleus. This interaction can be characterized by the Hamiltonian [Hap84]

$$\mathcal{H} = A\mathbf{I}\cdot\mathbf{S} + \gamma\mathbf{N}\cdot\mathbf{S} + \alpha\mathbf{K}\cdot\mathbf{S} + g_S\mu_B\mathbf{B}\cdot\mathbf{S} + g_I\mu_B\mathbf{B}\cdot\mathbf{I} + g_K\mu_B\mathbf{B}\cdot\mathbf{K} + \ldots, \tag{3.1}$$

where $\mathbf{I}$ is the rubidium nuclear spin, $\mathbf{S}$ is the spin of the rubidium valence electron, $\mathbf{N}$ is the rotational angular momentum of the rubidium-noble gas van der Waals molecule, $\mathbf{K}$ is the noble gas nuclear spin, and $\mathbf{B}$ is the external magnetic field. The exchange of angular momentum between a rubidium valence electron and a noble gas nucleus occurs either during the existence of a short-lived van der Waals molecule or during a binary collision between the two atoms. The creation and destruction of van der Waals molecules in the cells requires three-body collisions between a rubidium atom, a noble gas atom, and a buffer gas molecule. The rates of creation and destruction depend on the buffer gas pressure. Due to the high buffer gas pressure we usually use in our cells (about 1 atm), collisions with nitrogen suppress the lifetime of these molecules and thus binary collisions dominate the spin-exchange process. The spin-exchange method has been used to successfully polarize both ^{209}Rn and ^{223}Rn at the ISOLDE isotope separator at CERN [Kit88].

3.3.2 EDM Measurement

Once the atoms have been polarized, we can measure the EDM through its effect on the precession frequency. As mentioned above, the optical pumping cells illustrated in Fig. 3.1 will feature a measurement region with electrodes allowing us to apply an electric field across this region of the cell. This will be oriented along the magnetic field axis such that, after the application of an RF pulse, the atoms will precess at the frequency

$$\hbar\omega_{\pm} = 2\mu\mathrm{B} \pm 2d\mathrm{E}, \tag{3.2}$$

where μ is the magnetic dipole moment and $+(-)$ corresponds to the electric field oriented parallel (anti-parallel) to the magnetic field direction. We can thus obtain a measure of the atomic EDM through the change in the precession frequency with electric field direction:

$$d = \hbar\Delta\omega/4\mathrm{E}. \tag{3.3}$$

Given a non-zero EDM, a larger electric field would result in a larger frequency difference, which could be measured more accurately. This would imply that atomic EDM measurements could be improved by increasing the magnitude of the electric field indefinitely, but if the field is too high leakage currents can become an issue. Small currents through the glass between the two electrodes would create magnetic fields which would depend on the electric field orientation, thus mimicking the EDM signal. A comagnetometer (another species introduced to the measurement cell, which is expected to have no EDM and thus any change in its frequency could be attributed to a change in the magnetic field) can be used to correct for this systematic effect. However, it is best to operate at a level where leakage currents are expected

to be minimal. Our current experimental design uses an electric field of 5 kV/cm. The collaboration is investigating different cell materials and designs for the purpose of minimizing leakage currents, and will also use a comagnetometer, with the exact species still under consideration.

3.4 Measuring the Precession Frequency Using the Angular Distribution of Radiation

The ISAC facility cannot produce radon in the quantities necessary for the collective effects of precessing spins to be detectable through standard NMR measurement techniques. However, when polarized nuclei decay they emit radiation with a directional distribution dependent on the angle with respect to the polarization direction (defined by the magnetic field). By measuring this angular distribution we can determine the direction of the nuclear spins, and with a high enough count rate coupled with efficient detectors we can use the radiation signal to measure the precession frequency. The radon isotopes we are considering decay to francium through beta decay followed by the emission of one or more gamma rays. While beta-decay would have an anisotropy that could provide a frequency signal, we would need to integrate beta detectors into the measurement cell or the signal would be greatly reduced by betas interacting with the glass. Thus, the first stage of the experiment will use gamma-ray anisotropies as the precession frequency signal.

3.4.1 Detecting Gamma-Ray Anisotropies

The gamma-ray anisotropy detection scheme utilizes a ring of TIGRESS [Sve05] detectors as illustrated in Fig. 3.3. The combination of active and passive magnetic shielding will make the magnetic field as uniform as possible over the cell volume. The electrodes built into the cell to generate the electric field are not represented

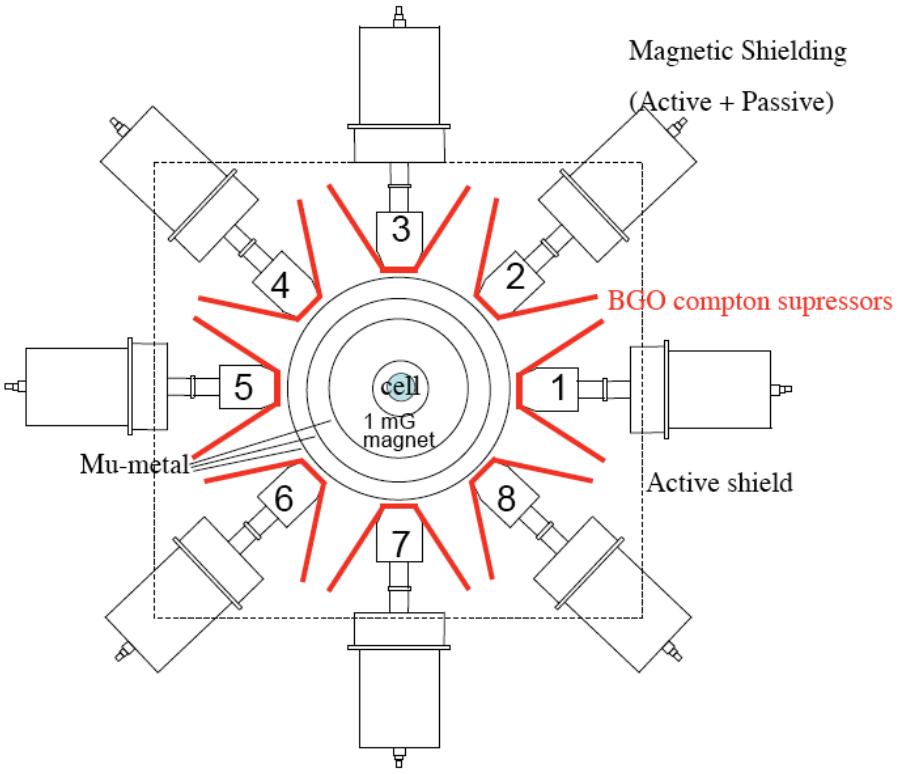

Figure 3.3: A sketch of the Radon EDM gamma-ray detection scheme.

in Fig. 3.3. We plan to run with a magnetic field of only 1 mGauss, which will provide a precession frequency slow enough to be measured via the TIGRESS detectors. Different gamma rays will have different anisotropies, so we can increase the statistical strength of our precession signal by monitoring the changing anisotropies in multiple gamma-ray lines simultaneously. The gamma-ray signal is still limited by the count rate of the detectors relative to what could be obtained using beta detectors in current mode, however.

3.4.2 Beta Asymmetry

The measurement of the radon precession frequency using the asymmetry in the distribution of the emitted beta particles requires a measurement cell that allows the beta particles to reach the detectors with minimal attenuation. Cells with thin

glass windows for beta transmission are under consideration. If we are able to design cells that will be structurally sound while still allowing for beta detection, we would be able to run in current-mode instead of the discrete photon-counting required by the gamma-ray detection. Being competitive with the ^{199}Hg results will require the beta-detection technique.

CHAPTER IV

Xenon Transfer Studies

4.1 Introduction

The first experimental work done in preparation for the radon EDM experiment was a feasibility study of the noble gas collection and transfer techniques proposed. TRIUMF's ISAC facility will provide us with a beam of radon atoms that we will need to move into a glass optical pumping cell. Our proposed mechanism accomplishes this task in two stages. First, we direct the beam to and implant it in a thin metal foil for a predetermined length of time (usually about two half-lives of the isotope being collected). Second, after we have ceased implantation, we heat the foil (forcing the atoms to diffuse out) and transfer the released noble gas atoms to the measurement cell. The transfer procedure involves moving the noble gas into a separate volume through the use of a coldfinger and pushing the noble gas in this volume into the measurement cell using a jet of nitrogen. Diffusion studies determined the optimum foil material, and a test of the transfer system was done to measure the efficiency of this process. TRIUMF could not produce radon beams at the time of these measurements, so we used ^{120}Xe (from a beam of ^{120}Cs, $T_{1/2} = 64$ s) as an experimentally equivalent alternative.

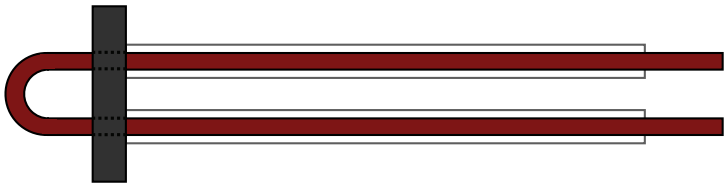

Figure 4.1: A sketch of the coldfinger prototype. The arms are 10 cm long thin-walled stainless steel tubes welded to two feed-through holes drilled in the mini conflat flange. Prototypes were built using 1/8" copper and stainless steel tubing for the liquid nitrogen flow.

4.2 Transfer Studies Using a Coldfinger

Our collaborators at TRIUMF undertook a study of the time-dependence of the release of noble gas atoms from three potential foil materials: tantalum, platinum, and zirconium [War05]. On the basis of these measurements, we decided that zirconium was the optimum material to use for the collection foil in our subsequent work. We directed a beam of ^{120}Cs onto the foil, located in a high-vacuum chamber, for about two half-lives of ^{120}Xe ($T_{1/2}$ = 40 m). A high-purity germanium (HPGe) detector monitored the activity at the foil.

Once we have finished collecting a sample of noble gas in the foil, we must efficiently transfer that sample to our measurement cell. The procedure for accomplishing this includes driving the diffusion from the foil by resistively heating it to about 1000°C (measured with a pyrometer), cryopumping to a coldfinger elsewhere in the vacuum system, and pushing the noble gas into the cell with a jet of nitrogen. A prototype coldfinger and pushing apparatus were designed and built at the University of Michigan and tested using ^{120}Xe at TRIUMF.

4.2.1 Coldfinger Prototype

The concept for the coldfinger prototype is a metal (stainless steel or copper) tube running through the vacuum system, cooled with a flow of liquid nitrogen. The outer

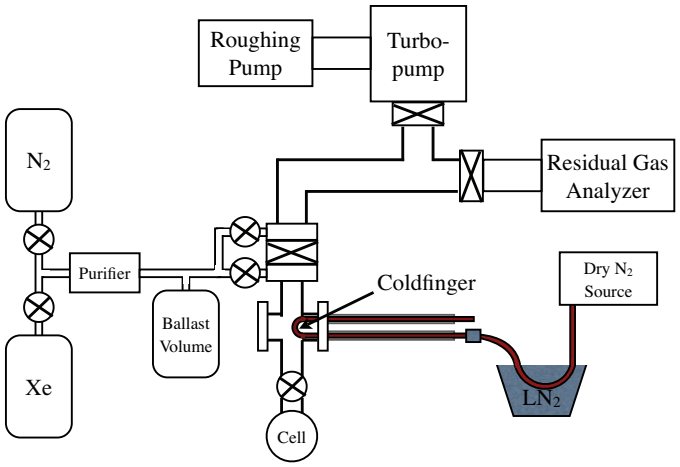

Figure 4.2: A diagram of the vacuum system used for the coldfinger prototype tests using natural xenon at the University of Michigan.

surface of the tube would reach temperatures low enough that the gas released by the foil would freeze to it. Fig. 4.1 shows a diagram of the prototype built at the University of Michigan. It consists of a loop of 1/8-inch copper tubing attached, via Swagelok fittings [Swa], at the ends of two 10 cm long thin-walled stainless steel tubes welded to a mini-conflat flange. The fittings are necessary to make the equipment vacuum-tight, but it also creates a heat sink connected to the liquid nitrogen tube that could limit the temperature we can reach. This motivates the length of the arms, which ensure that the bend in the tube (expected to be the locus for most of the frozen noble gas) reaches the lowest possible temperature. We designed the arms to have only a small volume between the outer surface and the liquid nitrogen tube in order to minimize the amount of dead space for the pushing process.

Prior to taking it to TRIUMF for the gas transfer system tests, we performed adsorption tests using natural xenon at the University of Michigan to confirm that the copper exposed to the vacuum system would reach temperatures low enough to freeze the xenon. Fig. 4.2 shows a sketch of the vacuum system used. Figs. 4.3 and 4.4 show examples of these measurements, observing the freezing process

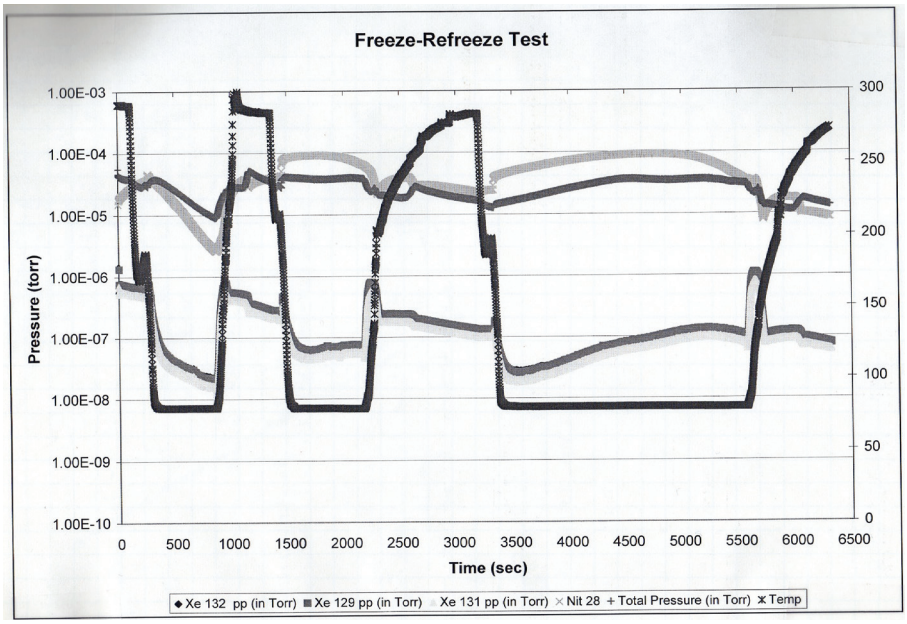

Figure 4.3: The partial pressure data from tests in which we cooled and warmed the coldfinger multiple times to freeze, release, and refreeze the same sample of natural xenon. The temperature, in Kelvin, was measured at the coldfinger outlet. The partial and total pressure readings were from the RGA.

in isolation as well as testing the full pushing procedure. In the tests performed to obtain the data in Fig. 4.3, we began with about 1×10^{-6} torr natural xenon in the vacuum system, with the coldfinger and residual gas analyzer (SRS-RGA200) [Sta] in a contiguous volume closed off from the vacuum pumps. We then cooled and warmed the coldfinger multiple times while continuously observing the xenon partial pressures with the RGA.

The data in Fig. 4.4 illustrate the results of a test of the pushing process. We let some natural xenon into the coldfinger chamber, cooled the coldfinger to freeze the xenon, and pumped out the rest of the vacuum system. We then filled the ballast volume with about 600 torr of nitrogen while allowing the coldfinger to warm up, filling the coldfinger volume with gaseous xenon. Once the coldfinger was warm enough that we were confident all the adsorbed xenon had been released, we opened the ballast valve to push the xenon into the cell, quickly closing the valve at the

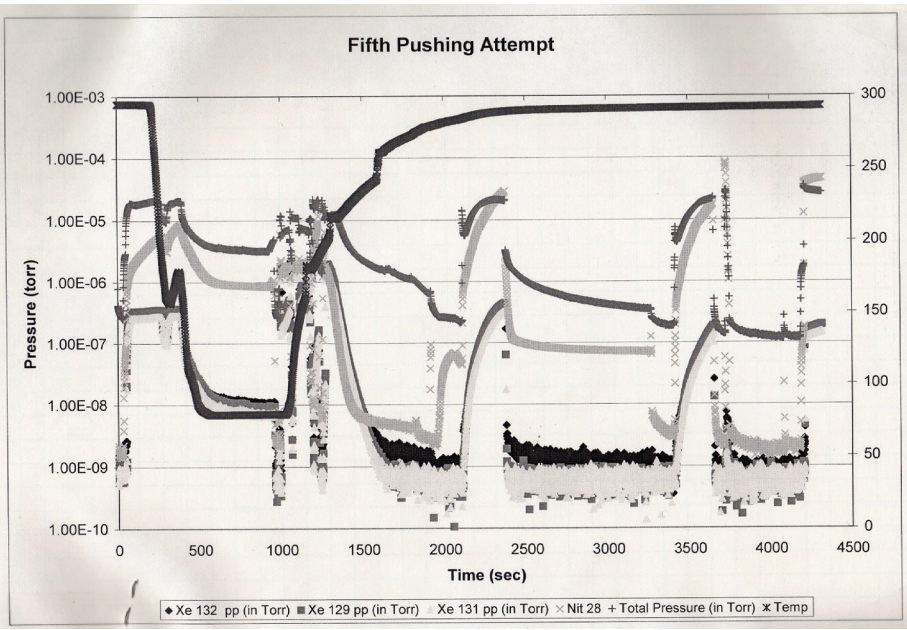

Figure 4.4: The partial pressure data from a test of the pushing procedure. At around 70 sec, we let xenon gas into the system. At about 200 sec, we began cooling the coldfinger. At about 960 sec, we closed off the coldfinger chamber from the rest of the vacuum system (including the RGA) and allowed it to warm up. At about 2100 sec, we used a jet of nitrogen to push the xenon into the cell, closed the cell, and pumped out the coldfinger volume. At 2400 sec, immersed the cell in liquid nitrogen. At 3400 sec, opened the cell, still in LN2, to release the nitrogen gas. At 3670 sec, monitoring the pressure with the RGA while pumping on the frozen cell. At 3700 sec, closed the cell and stopped freezing. At 4200 sec, we closed off the vacuum system from the turbopump, and opened the cell. The pressure reading at the RGA indicated that 50% of the original sample of xenon remained.

cell afterwards. As we pumped out the rest of the vacuum system, we immersed the cell in liquid nitrogen to freeze the xenon, allowing us to pump out the nitrogen and measure in isolation the amount of xenon transferred to the cell. By comparing the initial and final xenon partial pressures as measured by the RGA, we calculated a pushing efficiency of about 50%.

We had intended to place a temperature sensor at the bend in the liquid nitrogen tube so we could observe the xenon adsorption's dependence on coldfinger temperature. However, we found that the presence of the sensor functioned as a heat source that prevented the coldfinger from reaching temperatures below 95 K, so we began

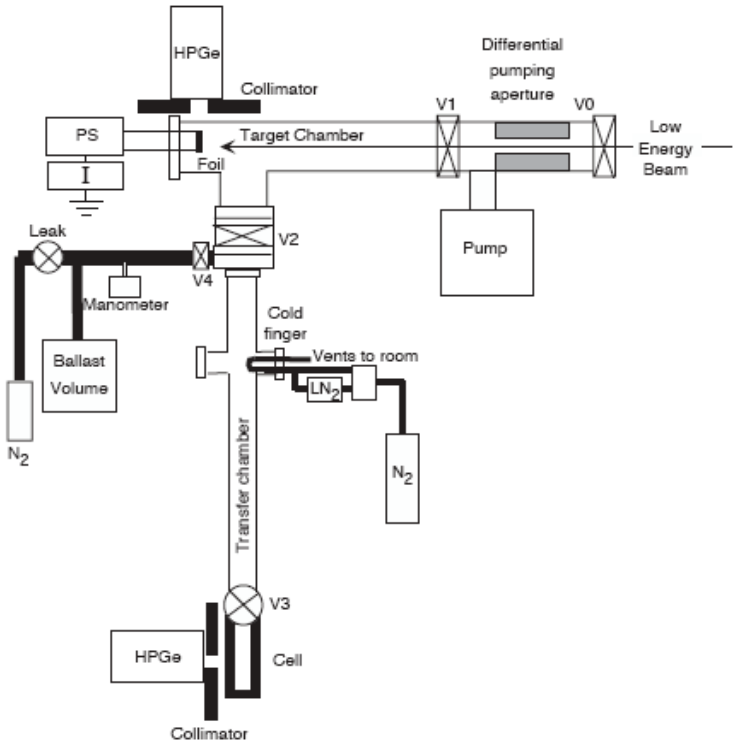

Figure 4.5: The apparatus built at TRIUMF for ^{120}Xe collection and transfer efficiency tests. The jet of nitrogen entered the vacuum system through valve V4, the coldfinger liquid nitrogen tubes were located in the cross in the transfer chamber as shown, and the cell was a stainless steel mini-conflat nipple.

measuring the temperature only at the outlet tube and assumed that the temperature at the bend must be less than or equal to that at the outlet, which reached 80 K.

4.2.2 The Gas Transfer Efficiency Test

We built the apparatus illustrated in Fig. 4.5 at TRIUMF in order to measure the efficiency of the prototype gas transfer equipment, work reported in Ref. [Nus04]. As in the foil diffusion studies, we implanted a beam of ^{120}Cs for about two half-lives of ^{120}Xe. We monitored the activity at the zirconium foil with a HPGe detector collimated to observe only the foil. After we finished collecting a sample, we turned off the beam, waited about 10 minutes to allow all the ^{120}Cs to decay, and closed valve

V1 to isolate the target and transfer chambers from the vacuum pump. Resistively heating the foil to about 1350 K released the xenon, and with liquid nitrogen flowing through the coldfinger we were able to observe the transfer of activity through the changing gamma-ray rates in the HPGe detector at the foil. We closed valve V2, heated the coldfinger to fill the transfer chamber and cell with ^{120}Xe gas, and loaded nitrogen gas in the ballast volume. Upon opening valve V4, the nitrogen gas expanded into the transfer chamber, pushing most of the xenon down into the cell. We then closed valve V3, and a second HPGe detector monitored the activity transferred to the cell. Immediately after pushing, the activity was at the very bottom of the cell. As can be inferred from Fig. 4.6, there was a delay between the completion of the pushing process and the detection of increased activity by the HPGe detector. We concluded that the collimation for the HPGe detector at the cell blocked activity originating from the bottom of the cell, so there was some delay between the push and the detection of increased activity as the xenon diffused through the nitrogen. This diffusion occurred with a time constant of about one minute. In order to prevent the possibility of the jet of nitrogen causing the cell to break, we used a stainless steel nipple instead of a glass sphere as the cell in these tests.

We sorted the spectra from the HPGe detectors located at the foil and cell into 4 keV bins. Fig. 4.7 shows the activity in the cell before and after a push. The peak at around 175 keV is a combination of four gamma rays from ^{120}Xe decay, with energies from 172.2 to 178.1 keV. We used these gamma rays as our measure of the ^{120}Xe activity. In order to subtract a time-dependent background from the bins of interest, we divided each run into a number of shorter segments with durations ranging from 90 to 400 s. The lengths of these time segments correspond to the stages of the ^{120}Xe transfer process as in Fig. 4.6. For each time segment we determined the average

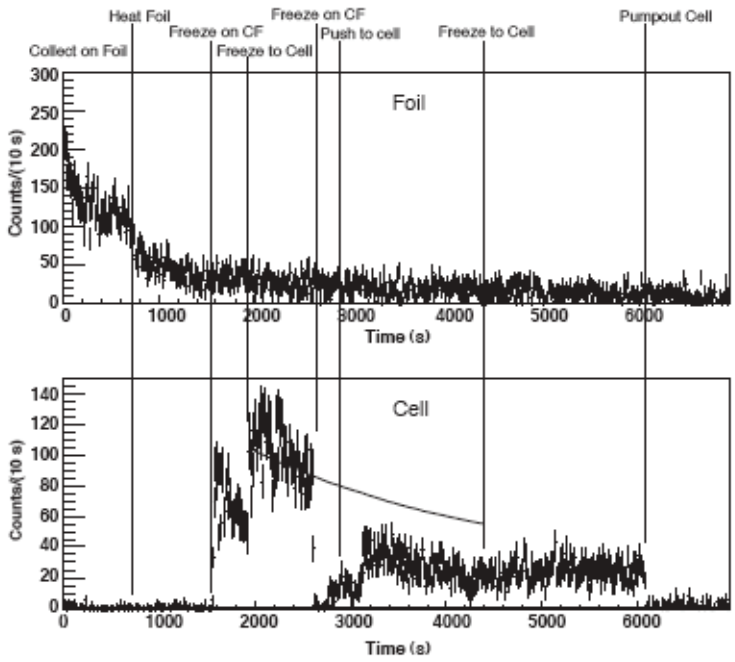

Figure 4.6: The background-corrected count rates for 172-178 keV gamma rays for the HPGe detectors in the foil and cell positions (top panel and bottom panel, respectively) for one cycle of collection and transfer. Freezing the gas to the cell at about 2000 s was done to calibrate against the cold finger (CF) freezing efficiency. The solid line in the bottom panel indicates the expected decay based on the calibration sample.

background over an energy range of about 70 keV (centered on 175 keV) from a linear fit. The main source of background counts was ^{120}I, which has a half-life of 81 minutes and thus would have an essentially constant count rate over the time scales of our segments. We then subtracted the background under the 172-178 keV peak from each time bin and fit the count rate to a decaying exponential with a time constant given by the ^{120}Xe half-life of $T_{1/2} = 40 \pm 1$ min [And64].

In order to calibrate the rates so that we would know how much activity we should observe in the cell if all of the xenon released from the foil made it into the cell, in two runs we froze the xenon in the transfer chamber into the cell by immersing it in liquid nitrogen. Once all the xenon had been cryopumped into the cell, we closed valve V3 and warmed the cell to release the xenon into the gas phase. We measured

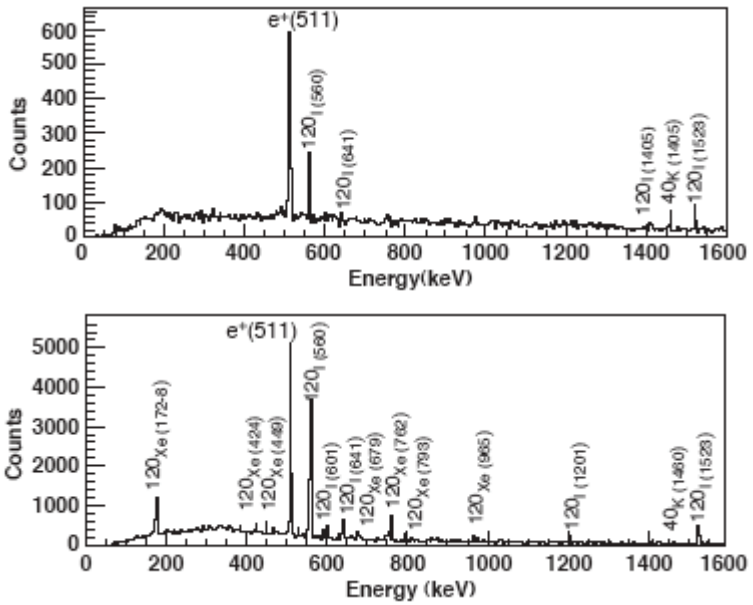

Figure 4.7: Gamma-ray spectra at the cell taken over 500 s intervals before (top) and after (bottom) we transferred xenon to the measurement cell. Note the different vertical scales. The ^{120}I background present prior to pushing is a decay product of ^{120}Xe from an earlier transfer.

the activity for 10-15 mins, then refroze the xenon onto the coldfinger, warmed the coldfinger, and pushed the xenon back into the cell as described above. In three additional runs, we determined the relative amount of xenon in the transfer chamber using the ratio of the measurement cell volume to the entire transfer chamber volume as determined from the calibration runs.

In order to allow data from different runs to be combined in the efficiency analysis, we extrapolated the count rates in the measurement cell to a fixed time t_0. We defined the transfer efficiency as the ratio of the extrapolated count rate after transfer to the extrapolated count rate for the ^{120}Xe measured in the calibration runs. We also used these runs to determine the ratio of the measurement cell volume to that of the total transfer chamber. The resulting weighted average of the transfer efficiency from the calibration runs was $\varepsilon = 0.43 \pm 0.01$, and for the remaining three runs was $\varepsilon = 0.39 \pm 0.03$. The uncertainties in these numbers are the combined statistical

uncertainties from the data and background determination. The major contribution to the estimated systematic uncertainty (2.5% of ε) is due to the ^{120}Xe half-life uncertainty.

In the course of these measurements we obtained a significant amount of ^{120}Xe decay data. Further, at the very end of the run we collected a sample of ^{120}Xe and allowed it to decay in the foil for multiple half-lives while monitoring the activity. The combined data from all of the samples used in the transfer tests and the final sample contained enough statistics to allow the half-life value from Ref. [And64] to be improved. The corrected value, reported in Ref. [Phi06], was $T_{1/2} = 46.0 \pm 0.6$ min.

4.3 Conclusions from the Xenon Transfer Studies

Our studies of the gas transfer system using ^{120}Xe at TRIUMF demonstrated the validity of the overall design of this facet of the radon EDM experimental equipment. We determined that zirconium is the optimum material for the thin metal foil used to collect a sample of noble gas atoms. As observed in the foil diffusion studies in Ref. [War05], about 80% of the collected xenon diffused from the foil when heated to 1350 K. The remnant activity was most likely due to xenon implanted on collimators and other parts of the apparatus and xenon diffusing deeper into the foil. We successfully used the coldfinger and nitrogen pushing technique to transfer about 40% of the xenon released from the foil into the measurement cell. This functions as a proof of principle for the gas transfer system.

Our observations during the course of these studies suggested adjustments that could lead to large improvements in the transfer efficiency. First, improved beam optics and foil design could prevent the beam from impacting any part of the appa-

ratus aside from the foil, allowing an increase in the percentage of collected noble gas released upon heating the foil. The area where most improvement can be made is the coldfinger and transfer chamber design. The arms of the mini-conflat cross and the inlet and outlet coldfinger arms (see Fig. 4.1) provide extra volumes into which some of the xenon could have been pushed upon release of the nitrogen. Redesigning the coldfinger to eliminate these blind alleys could improve efficiency greatly. Finally, creating a smooth path for the nitrogen to follow into the cell could lessen the turbulence generated by the injection of a high pressure of nitrogen into what is essentially a vacuum. The concern is that eddies in a turbulent flow could cause some mixing of the xenon into the nitrogen before it reaches the cell. This would prevent the nitrogen from acting like a piston, pushing the xenon ahead of it into the cell. An adjusted design taking into account these considerations features a cooled copper ring incorporated into the side walls of the transfer tube to function as the freezing surface, and nitrogen released into the transfer chamber from above so that there are no changes in the direction of the nitrogen flow. A collaborator has designed and built a coldfinger to the above specifications, and in tests with ^{121}Xe and ^{123}Xe at TRIUMF in the summer of 2008 (using a system with a smooth path for the nitrogen flow) we achieved a transfer efficiency of above 90%.

CHAPTER V

Rubidium Polarization Studies

5.1 Introduction

We polarized samples of ^{209}Rn in glass optical pumping cells containing a small amount of rubidium and nitrogen in measurements performed at SUNY Stony Brook (discussed in Chapter VI). Circularly polarized laser light tuned to the ^{85}Rb D1 transition polarized the rubidium atoms and spin-exchange collisions transfered this polarization to the radon nuclei, a process discussed in Chapter III. Our signal in the Stony Brook measurements was the anisotropy of the gamma rays emitted following ^{209}Rn electron capture decay to ^{209}At. This anisotropy depends on the alignment (the 2nd moment of the polarization) of the ^{209}Rn nuclear sublevels. Thus, a calculation of the expected ^{209}Rn alignment in our cells requires knowledge of the rubidium polarization. If we can determine the rubidium polarization at the cell temperatures used in the Stony Brook measurements, we can eliminate that as an unknown parameter in our analysis of the ^{209}Rn anisotropy data.

The physics of rubidium laser-polarization is well understood, but models are important. We performed numerical calculations of the temperature dependence of the rubidium polarization in our cells. These calculations involve numerous input parameters, such as spin-destruction rates and the incident laser power, that intro-

duce uncertainties into the results. Thus, we concluded that it would be beneficial to recreate the relevant experimental parameters of the Stony Brook measurements at the University of Michigan and measure the rubidium polarization directly using electron spin resonance (ESR). The results of these measurements differed significantly from the calculations. Since the ESR measurements correspond to the conditions of the Stony Brook measurements much more accurately than do the calculations, we used the measured values as input parameters in the ^{209}Rn anisotropy data analysis.

5.2 Rubidium Polarization Calculation

We modeled rubidium polarization for our cells by adapting the work of Ref. [Wag89] to the temperatures, cell size, and laser profile used in the ^{209}Rn runs. The cells were spherically shaped glass of about 2.5 cm radius containing a small amount of natural rubidium, about one atmosphere nitrogen, and on the order of one million radon atoms. They were heated to temperatures from 130 to 220°C in the Stony Brook measurements, so we were interested in the rubidium polarization over that temperature range.

We discretized the relevant expressions in Ref. [Wag89] to facilitate a numerical calculation of the rubidium polarization, a procedure discussed in detail below. The resulting expression gave the rubidium polarization as a function of the distance from the surface of the cell along the axis defined by the direction of the laser light. Thus, for a cell of arbitrary geometry, the polarization function simply needed to be averaged over the volume of the cell to obtain the average rubidium polarization. The differential equation for the photon flux (in units of photons per unit area per unit frequency per unit time) at the frequency ν and depth z (along the axis defined by the direction of the laser light, parallel or antiparallel to the direction of the applied

magnetic field) was adapted from the continuous form

$$\frac{d\Phi(\nu,z)}{dz} = -\lambda_{\sigma_+}^{-1}(\nu,z)\Phi(\nu,z) \tag{5.1}$$

to the discrete form

$$\frac{\delta\Phi(\nu,z)}{\delta z} = -\lambda_{\sigma_+}^{-1}(\nu,z)\Phi(\nu,z). \tag{5.2}$$

Here $\lambda_{\sigma_+}(\nu,z)$ is the absorption length of the incident, right circularly polarized light. The photon flux at a cell depth $z+\delta z$ can be calculated from the flux at z since, for small δz, Eq. 5.2 implies that

$$\Phi(\nu,z+\delta z) = \Phi(\nu,z)(1-\lambda_{\sigma_+}^{-1}(\nu,z)\delta z). \tag{5.3}$$

If we divide the cell into segments of width δz along the z-axis, the flux at the nth segment is

$$\Phi(\nu,n) = \Phi(\nu,0)\prod_{k=0}^{n-1}(1-\lambda_{\sigma_+}^{-1}(\nu,k)\delta z), \tag{5.4}$$

where $\Phi(\nu,0)$ is the flux at the surface of the cell. The absorption length for polarized photons is given by

$$\lambda_{\sigma_+}^{-1}(\nu,z) = \lambda_0^{-1}(\nu)\frac{\Gamma_{\mathrm{SD}}}{\gamma_{\mathrm{opt}}(z)+\Gamma_{\mathrm{SD}}}, \tag{5.5}$$

where the rubidium spin destruction rate Γ_{SD} is given by the combination of the contributions of rubidium-rubidium collisions and rubidium-nitrogen collisions,

$$\Gamma_{\mathrm{SD}} = k_{\mathrm{Rb-Rb}}\left[\mathrm{Rb}\right] + k_{\mathrm{Rb-N_2}}\left[\mathrm{N_2}\right]. \tag{5.6}$$

The radon pressure in our cells was so low that the effect of Rb-Rn collisions was negligible. The inverse of the absorption length for unpolarized light in an unpolarized vapor is $\lambda_0^{-1}(\nu) = [\mathrm{Rb}]\sigma_{\mathrm{s}}(\nu)$, and the scattering rate of circularly polarized

photons per alkali-metal atom in an unpolarized vapor at the nth segment is

$$\gamma_{\text{opt}}(n) = \sum_{\nu} \Phi(\nu, n)\sigma_s(\nu). \tag{5.7}$$

The cross section for scattering unpolarized light, $\sigma_s(\nu)$, is given by

$$\sigma_s(\nu) = \frac{(\Gamma/2)^2}{(\nu - \nu_0)^2 + (\Gamma/2)^2}\sigma_0, \tag{5.8}$$

where ν_0 is the center of the laser frequency spectrum and Γ is the Rb D1 absorption linewidth. For the rubidium number density as a function of temperature we use [Alc84]

$$[\text{Rb}] = 10^{9.318 - \frac{4040}{T}}/k_B T. \tag{5.9}$$

The rubidium polarization at the nth segment in the cell can thus be written as

$$P_{\text{Rb}}(n) = \frac{\gamma_{\text{opt}}(n)}{\gamma_{\text{opt}}(n) + \Gamma_{\text{SD}}}. \tag{5.10}$$

We used this to define a step function $RbP(z)$ that described the rubidium polarization as a stepwise continuous function of cell depth that must be averaged over the volume of the cell. For a spherical cell (radius R),

$$\bar{P}_{\text{Rb}} = \frac{1}{\frac{4}{3}\pi R^3} \int_0^{2R} RbP(z)\pi \left(R^2 - \frac{z^2}{4}\right) \mathrm{d}z. \tag{5.11}$$

In order to ensure that this equation converged properly (equivalent to ensuring that δz was small enough that Eq. 5.3 was valid), we set $\delta z = 2\max\left(\lambda_0^{-1}(\nu)\right)$ at each cell temperature. This provided three digits of precision in the average rubidium polarization values. Using the values $k_{\text{Rb-Rb}} = 3.9 \times 10^{-14}$ [Bar98] and $k_{\text{Rb-N}_2} = 9.4 \times 10^{-18}$ [Wag91] to obtain the value of Γ_{SD} at the cell temperature under consideration and the parameters listed in Table 5.1, we obtained numerical values for the average rubidium polarization at each cell temperature studied. Fig. 5.1 shows

Table 5.1: The parameters used in the calculation of temperature-dependent rubidium polarization.

Param.	Description	Value
σ_0	peak scattering cross section	2.82×10^{-13} cm^2
Γ	rubidium absorption linewidth	15 GHz
P_{N_2}	nitrogen pressure	1 atm
Γ_{laser}	FWHM, gaussian laser spectrum	1000 GHz
ν_0	mean laser frequency	3.77×10^{14} Hz
I	laser intensity	0.5 W/cm^2

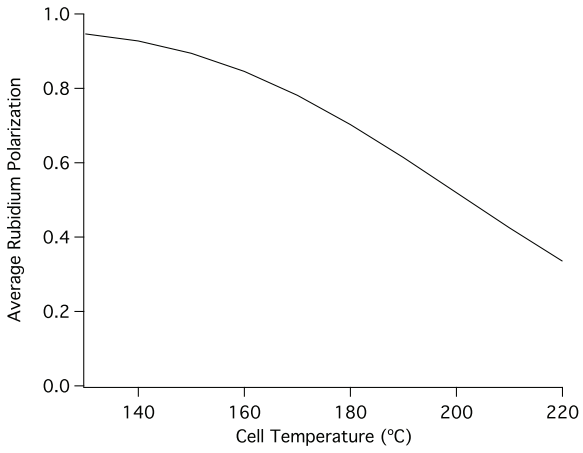

Figure 5.1: The result of the rubidium polarization calculation over the range of cell temperatures used in the radon polarization measurements.

the results of this calculation, illustrating the decrease in the rubidium polarization with increasing temperature. This model does not accommodate wall effects, so there are not separate calculations for coated and uncoated cells.

It was not possible to determine the validity of some of these parameters quantitatively. For example, the actual laser profile was much more complex than a simple gaussian, and the laser intensity was an estimate (based on the laser power and the cross-section of the cell). Further, the method above does not contain a mechanism to account for the possibility that the tail of the laser profile could overlap with the rubidium D2 line. This would effectively cause the laser to depolarize the rubidium concurrent to polarizing it, preventing the rubidium polarization from reaching 100% polarization at any temperature. Imperfect polarization of the laser light would also

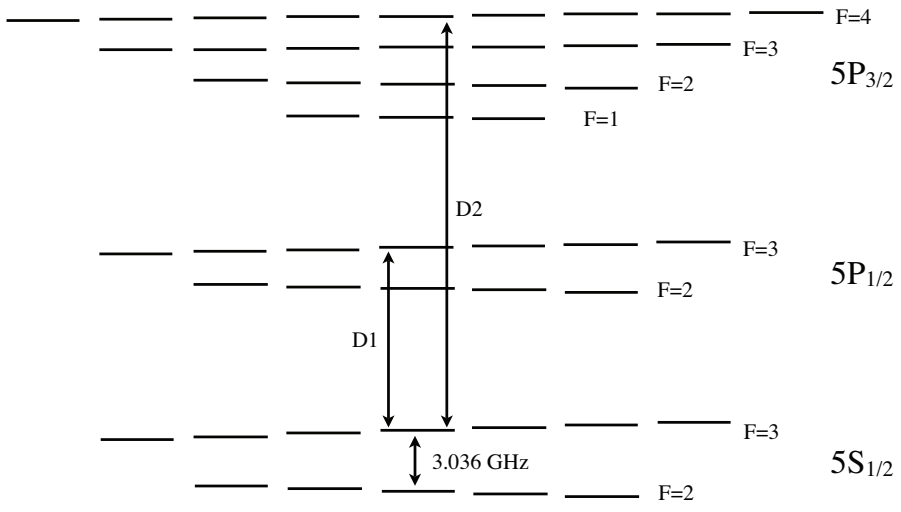

Figure 5.2: The hyperfine structure of ^{85}Rb, including the hyperfine splitting of the $5S_{1/2}$ state. The D1 and D2 transitions are illustrated.

limit the achievable rubidium polarization, as would skew light effects [Cha02], in which there is a small angle between laser and magnetic field axes. In order to obtain rubidium polarization values not subject to these weaknesses, rubidium fluorescence polarimetry measurements were made on the same cells under similar experimental conditions as experienced at Stony Brook.

5.3 Rubidium Electron Spin Resonance Measurements

We used ESR to measure the rubidium polarization in the same cells and temperatures used in the Stony Brook radon measurements. ESR as performed here utilizes the light emitted by an alkali-metal in the optical pumping process to generate a signal dependent on the populations of the alkali-metal's hyperfine levels. The relevant hyperfine states for ^{85}Rb are shown in Fig. 5.2. Circularly polarized D1 light depopulates all but the $m_F = 3$ state, populating the $5P_{1/2}$ and $5P_{3/2}$ states, which are collisionally mixed. As these states decay back to the ground state, they emit D1 and D2 light as fluorescence. Spin-exchange collisions between alkali-metal

atoms induce transitions between the ground-state hyperfine levels. The pumping and spin-exchange processes achieve an equilibrium in which the populations can be described by a spin temperature β [And60], where the ratios of the populations of neighboring hyperfine levels are

$$\rho_{m_F}/\rho_{m_F-1} = e^{\beta}. \tag{5.12}$$

An RF signal tuned to the splitting between two of the ground state hyperfine levels would drive a transition between them, increasing the absorption of laser light from the ground state and thus the number of atoms in an excited state. This is accompanied by an increase in fluorescence from the atoms proportional to the population difference between the levels. Following the derivation in Ref. [Bab05], the Hamiltonian for a rubidium (or other alkali-metal) atom in a uniform magnetic field, exposed to a transverse RF field of amplitude B_x, is given by

$$\mathcal{H} = \sum_m E_m|m\rangle\langle m| + g_s\mu_B S_x B_x \cos(\omega t) = \mathcal{H}_0 + V_0\cos(\omega t). \tag{5.13}$$

The equation of motion is

$$\imath\hbar\frac{d\rho}{dt} = -[\rho, \mathcal{H}], \tag{5.14}$$

where ρ is the density matrix

$$\rho = \sum_{m,n} \rho_{mn}|m\rangle\langle n|. \tag{5.15}$$

The potential V is proportional to the operator S_x, which connects neighboring angular momentum states, and $\mathcal{H}_0$ is diagonal, so the elements of ρ are nonzero for $m = n$ and $m = n \pm 1$. The equation of motion for neighboring elements of the

density matrix is

$$\begin{aligned}
\imath\hbar\frac{d\rho_{m,m-1}}{dt} &= \langle m|\left(-\rho(\mathcal{H}_0+V)+(\mathcal{H}_0+V)\rho\right)|m-1\rangle \\
&= \langle m|\left[-\rho\left(\sum_n E_n|n\rangle\langle n|\right)+\left(\sum_n E_n|n\rangle\langle n|\right)\rho\right]|m-1\rangle \\
&\quad +\langle m|-\rho V|m-1\rangle+\langle m|V\rho|m-1\rangle \\
&= \left(E_m-E_{m-1}\right)\rho_{m,m-1}+V_{m,m-1}\left(\rho_{m-1}-\rho_m\right), \qquad (5.16)
\end{aligned}$$

where $V_{m,m-1}=\langle m|V|m-1\rangle$, $\rho_m\equiv\rho_{m,m}$, and $\rho_{m-1}\equiv\rho_{m-1,m-1}$. In order to provide for the decay in the coherence between these neighboring states, we add the term $-\imath\gamma\rho_{m,m-1}$ to Eq. 5.16. If we assume the coherence has the form $\rho_{m,m-1}=\sigma e^{-\imath\omega t}$, we get

$$\begin{aligned}
\imath\hbar\frac{d\sigma}{dt}e^{-\imath\omega t} &= (E_m-E_{m-1}-\hbar\omega)\sigma e^{-\imath\omega t}-\imath\gamma\sigma e^{-\imath\omega t} \\
&\quad +\langle m|V_0|m-1\rangle(\rho_{m-1}-\rho_m)\left(\frac{e^{\imath\omega t}+e^{-\imath\omega t}}{2}\right). \qquad (5.17)
\end{aligned}$$

Multiplying both sides by $e^{\imath\omega t}$ and eliminating the $e^{2\imath\omega t}$ term through the rotating wave approximation (thus ignoring the Bloch-Siegert shift [Blo40]), we get

$$\imath\hbar\frac{d\sigma}{dt} = (E_m-E_{m-1}-\hbar\omega)\sigma-\imath\gamma\sigma+\langle m|V_0|m-1\rangle\left(\frac{\rho_{m-1}-\rho_m}{2}\right). \qquad (5.18)$$

The steady state solution to this equation is

$$\sigma=\frac{\langle m|V_0|m-1\rangle(\rho_{m-1}-\rho_m)}{2(\Delta+\imath\gamma)}, \qquad (5.19)$$

where $\Delta=\hbar\omega-(E_m-E_{m-1})$. The conjugate of this expression is

$$\sigma^*=\frac{\langle m-1|V_0|m\rangle(\rho_{m-1}-\rho_m)}{2(\Delta-\imath\gamma)}. \qquad (5.20)$$

We now turn our attention to the equations of motion for the diagonal elements of

the density matrix. We find

$$\begin{aligned} \imath\hbar\frac{d\rho_m}{dt} &= \langle m|V|m-1\rangle\langle m-1|\rho|m\rangle - \langle m|\rho|m-1\rangle\langle m-1|V|m\rangle \\ &= \langle m|V|m-1\rangle\sigma^* e^{\imath\omega t} - \sigma e^{-\imath\omega t}\langle m-1|V|m\rangle \\ &= \frac{\langle m|V_0|m-1\rangle\sigma^* - \langle m-1|V_0|m\rangle\sigma}{2}, \end{aligned} \tag{5.21}$$

using

$$\langle m|\rho|m-1\rangle = \rho_{m,m-1} = \sigma e^{-\imath\omega t} \Rightarrow \langle m-1|\rho|m\rangle = \sigma^* e^{\imath\omega t}.$$

Similarly,

$$\imath\hbar\frac{d\rho_{m-1}}{dt} = \frac{\langle m-1|V_0|m\rangle\sigma - \langle m|V_0|m-1\rangle\sigma^*}{2}. \tag{5.22}$$

As we drive the transition between neighboring states, the observed signal will be proportional to $dF_z/dt \equiv d(\rho_m - \rho_{m-1})/dt$, the change in the population difference between the states. We find

$$\frac{dF_z}{dt} = \frac{|\langle m|V_0|m-1\rangle|^2}{\hbar}\left(\frac{\gamma}{\Delta^2+\gamma^2}\right)(\rho_{m-1} - \rho_m). \tag{5.23}$$

Since the angular momentum eigenstates are the z-projection of F, the matrix element is

$$|\langle m|V_0|m-1\rangle|^2 = (g_s\mu_B B_x)^2\,|\langle F, m_F|S_x|F, m_F-1\rangle|^2\,, \tag{5.24}$$

and we must decompose the eigenstates into the nuclear and electronic parts,

$$|F, m_F\rangle = |I, m_I\rangle \oplus |S, m_S\rangle. \tag{5.25}$$

Since $m_F = m_I + m_S = m_I \pm 1/2$, we use $m_I = m_F \mp 1/2$ and $m_S = \pm 1/2$ to write

$$\begin{aligned} |F, m_F\rangle &= \left|I, m_F - \frac{1}{2}\right\rangle \oplus \left|\frac{1}{2}, \frac{1}{2}\right\rangle \langle I, \frac{1}{2}; m_F - \frac{1}{2}, \frac{1}{2} \mid F, m_F\rangle \\ &\quad + \left|I, m_F + \frac{1}{2}\right\rangle \oplus \left|\frac{1}{2}, -\frac{1}{2}\right\rangle \langle I, \frac{1}{2}; m_F + \frac{1}{2}, -\frac{1}{2} \mid F, m_F\rangle \end{aligned} \tag{5.26}$$

and

$$
\begin{aligned}
|F, m_F - 1\rangle &= \left|I, m_F - \frac{3}{2}\right\rangle \oplus \left|\frac{1}{2}, \frac{1}{2}\right\rangle \langle I, \frac{1}{2}; m_F - \frac{3}{2}, \frac{1}{2} \mid F, m_F - 1\rangle \\
&\quad + \left|I, m_F - \frac{1}{2}\right\rangle \oplus \left|\frac{1}{2}, -\frac{1}{2}\right\rangle \langle I, \frac{1}{2}; m_F - \frac{1}{2}, -\frac{1}{2} \mid F, m_F - 1\rangle. \qquad (5.27)
\end{aligned}
$$

So

$$
\begin{aligned}
|\langle F, m_F|S_x|F, m_F - 1\rangle|^2 &= \frac{1}{4}\langle F, m_F|S_+|F, m_F - 1\rangle\langle F, m_F - 1|S_-|F, m_F\rangle \\
&= \frac{\hbar^2}{4}\left(\langle I, \frac{1}{2}; m_F - \frac{1}{2}, \frac{1}{2} \mid F, m_F\rangle\langle I, \frac{1}{2}; m_F - \frac{1}{2}, -\frac{1}{2} \mid F, m_F - 1\rangle\right)^2. \qquad (5.28)
\end{aligned}
$$

In the case $F = I + 1/2$, the expressions for the Clebsch-Gordan coefficients are

$$
\begin{aligned}
\langle F - \frac{1}{2}, \frac{1}{2}; m_F - \frac{1}{2}, -\frac{1}{2} \mid F, m_F - 1\rangle &= \frac{(-1)^{2(F+m_F)}\sqrt{1 + F - m_F}}{\sqrt{2I + 1}} \qquad (5.29) \\
\langle F - \frac{1}{2}, \frac{1}{2}; m_F - \frac{1}{2}, \frac{1}{2} \mid F, m_F\rangle &= \frac{(-1)^{2(F+m_F)}\sqrt{F + m_F}}{\sqrt{2I + 1}}, \qquad (5.30)
\end{aligned}
$$

and for $F = I - 1/2$, they are

$$
\begin{aligned}
\langle F + \frac{1}{2}, \frac{1}{2}; m_F - \frac{1}{2}, -\frac{1}{2} \mid F, m_F - 1\rangle &= \frac{\sqrt{F + m_F}}{\sqrt{2I + 1}} \qquad (5.31) \\
\langle F + \frac{1}{2}, \frac{1}{2}; m_F - \frac{1}{2}, \frac{1}{2} \mid F, m_F\rangle &= -\frac{\sqrt{1 + F - m_F}}{\sqrt{2I + 1}}. \qquad (5.32)
\end{aligned}
$$

In both cases the matrix element reduces to the same expression, and we find

$$
\frac{dF_z}{dt} = \frac{\hbar}{4}\left(\frac{\gamma}{\Delta^2 + \gamma^2}\right)\left(\frac{g_s\mu_B B_x}{2I + 1}\right)^2 (F(F + 1) - m_F(m_F - 1))(\rho_{m-1} - \rho_m), \qquad (5.33)
$$

which illustrates the dependence of the ESR signal on the angular momentum quantum numbers and the difference in the populations of the two hyperfine levels involved.

5.3.1 Apparatus and Measurement Procedure

We placed the cells, containing rubidium and about 1 atm of nitrogen, in a glass clamshell oven at the center of a pair of Helmholtz coils. A flow of hot air heated them

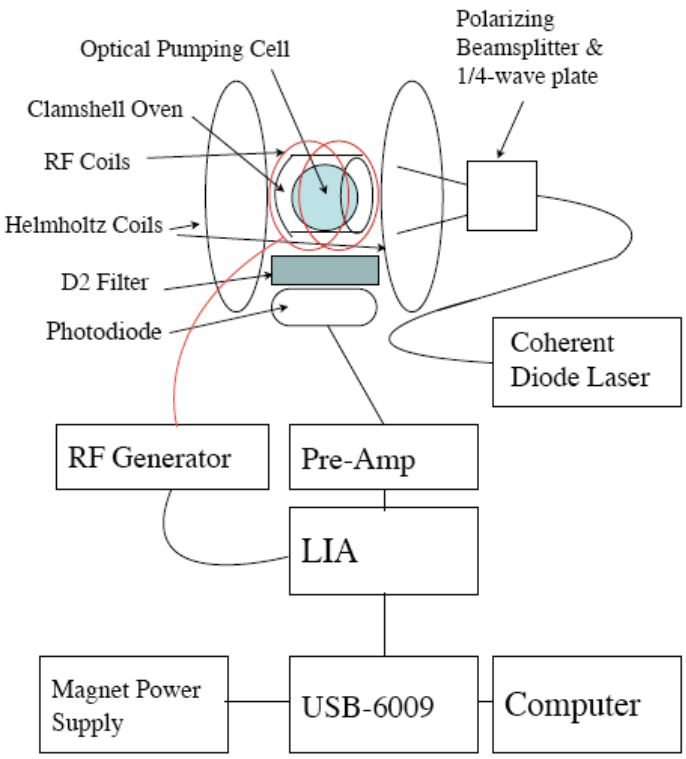

Figure 5.3: The rubidium fluorescence polarimetry apparatus.

to the desired temperatures. A pair of RF coils were placed around the oven, the cell was illuminated by circularly polarized D1 light from a Coherent diode laser (FAP System) [Coh], and a photodiode behind a D2 filter was placed near the cell to detect the fluorescence light (see Fig. 5.3). We set the RF to 15 MHz with an amplitude chopped with a square wave at a frequency of 3 Hz. As the magnetic field swept from high to low or low to high through all of the rubidium hyperfine resonances, the lock-in ampifier (locked to the RF amplitude modulation frequency) outputs a signal proportional to the change in the fluorescence seen by the photodiode with the RF on and off. When the RF was on and the magnetic field was swept across one of the hyperfine resonances, the RF field drove the transition between two hyperfine states, resulting in an increase in the rate of rubidium excitation from the laser light and a corresponding increase in the amount of D2 fluorescence light emitted. Since

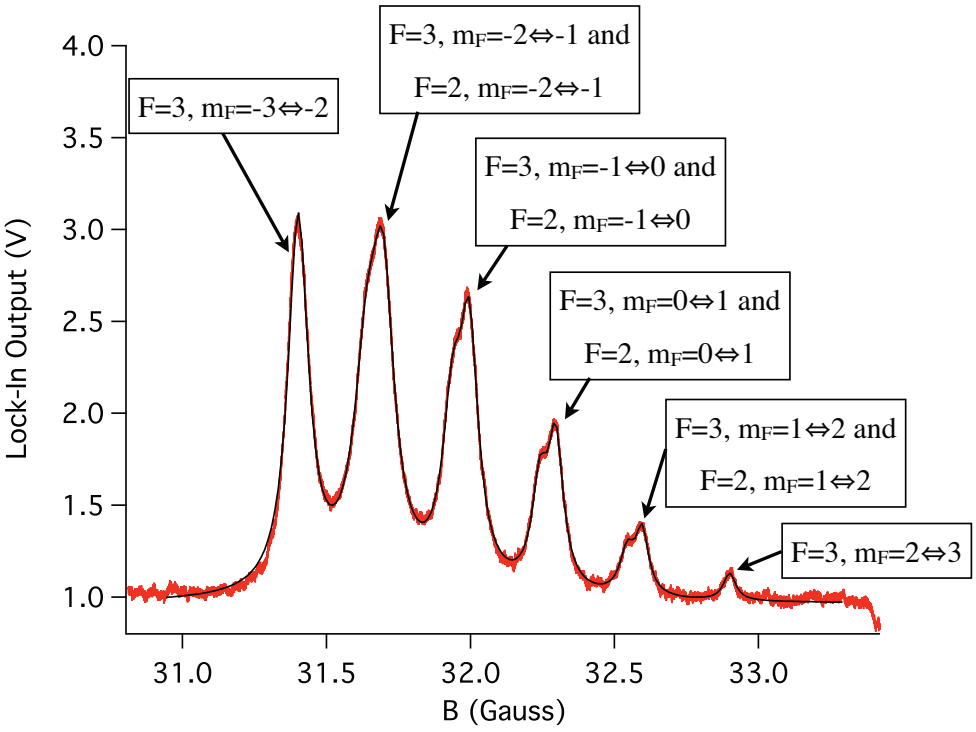

Figure 5.4: A ^{85}Rb ESR spectrum obtained with low optical pumping power, allowing the peaks from all possible hyperfine transitions to be visible. The black line is a fit to the spectrum using ten Lorentzian functions on a flat background.

the signal was the difference in the amount of fluorescence with the RF on and off, it was relatively insensitive to any differences in the placement of the photodiode from one run to another. Fig. 5.4 shows an example spectrum involving all possible peaks, generated by performing an ESR measurement using a low optical pumping power. The magnetic field used for that measurement was strong enough for the $F = 2$ transitions to be just distinguishable from the $F = 3$ ones. The laser power at the cell was reduced by using a lens to expand the beam.

The above ESR measurement procedure using normal laser power produced spectra like the one shown in Fig. 5.5, which includes labels of the hyperfine transitions giving rise to the peaks. An increase in fluorescence indicated partial destruction of the polarization of the rubidium, the extent of which was dependent on the RF

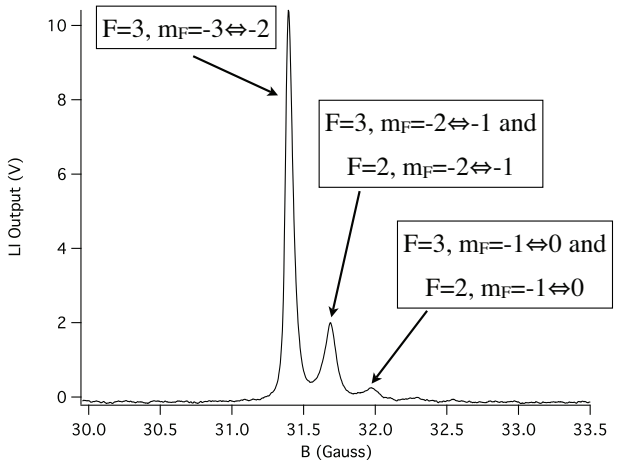

Figure 5.5: A ^{85}Rb ESR spectrum measured in an uncoated cell at 170°C and 7 V RF power. The peaks are labeled with the corresponding hyperfine transitions.

power. It was therefore necessary to extrapolate the RF power to zero. Thus we obtained spectra in each cell type and temperature over a range of applied RF voltages (between 1 and 10 V).

5.3.2 Data Analysis and Results

The ^{85}Rb polarization can be extracted from the relative areas of the ESR peaks. Since we are assuming a spin-temperature distribution for the hyperfine state populations, the polarization is [Bab05]

$$P = \frac{e^{\beta} - 1}{e^{\beta} + 1}, \tag{5.34}$$

where e^{β} is as defined in Eq. 5.12. If we can extract a value for e^{β} from our data, we can determine the rubidium polarization. The area of a single peak in an ESR spectrum is given by Eq. 5.33. As the $F = 3$ and $F = 2$ peaks in our data were nearly degenerate (see Fig. 5.5), we determined the ratio of the area of the $F = 3, m_F = 3 \leftrightarrow 2$ peak to the combined areas of the $F = 3, m_F = 2 \leftrightarrow 1$ and $F = 2, m_F = 2 \leftrightarrow 1$ peaks. We find that this ratio, denoted A, is $3/7e^{\beta}$. The ^{85}Rb

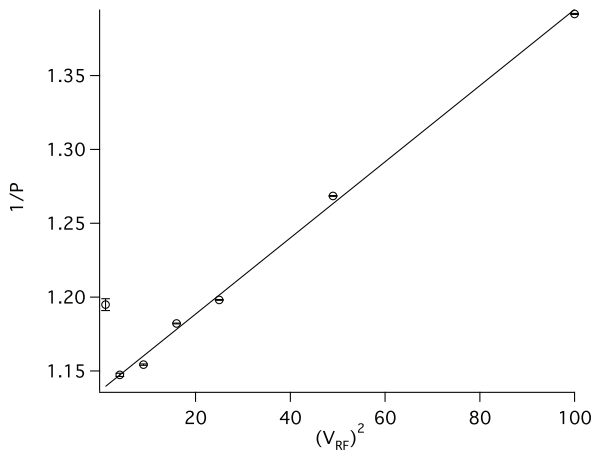

Figure 5.6: An illustration of the dependence of the rubidium polarization on the magnitude of the applied RF voltage. The data points are from an uncoated cell at 180°C. The smaller signal size at low RF voltage made those points more difficult to measure.

polarization is then

$$P_{\mathrm{Rb}} = \frac{7A - 3}{7A + 3}. \tag{5.35}$$

We fit the spectra to a function with multiple Lorentzian shapes and a constant background as in Fig. 5.4. The number of peaks resolvable above background varies from 3 to 7. We obtain polarization values for each cell at each temperature and RF voltage by averaging the results from the upward and downward magnetic field sweeps.

The data in Fig. 5.6 illustrate the dependence of the ESR signal on the RF power applied to the cell. The rubidium polarization is inversely proportional to the square of the RF voltage, a relation that allows us to extrapolate to zero RF power. We fit the values of $1/P_{\mathrm{Rb}}$ to a linear function of V_{RF}^2. We compensate for the poor fit (see Fig. 5.6) by multiplying the intercept error by the square root of the χ^2 for the fit, since the large deviation from the fit at low V_{RF}^2 appears to be due to an underestimation of the errors. While the low-RF points in some of the data give the appearance of a systematic shift away from the fit line, inspection of the data for

different temperatures indicates that the low-RF deviation is actually random scatter from the fit line. We therefore can conclude that the fitting procedure underestimates the uncertainties in the Lorentzian peak areas. We use this procedure, with corrected uncertainties, to determine the rubidium polarization at a particular temperature for each cell.

We average the data from the two coated and two uncoated cells to obtain one set of rubidium polarization values for each cell type. The results, presented in Figs. 5.7 and 5.8, indicate that the rubidium polarization does not approach unity as the cell temperature decreases. This could be due to a skew-light effect [Cha02]. Since our polarization optics emit two beams of light that we direct so that they both illuminate the cell, these beams must necessarily be propagating through the cell at slightly different angles. A percentage of the beam would then act to depolarize the rubidium atoms, limiting the maximum achievable polarization. We also considered the possibility that the nitrogen was attenuating the fluorescence light, which could affect the size of the first peak more than the second. To test this possibility, we performed a couple ESR measurements with the laser blocked from the half of the cell nearer the photodetector. The resulting spectra actually had a slightly higher overall intensity with no significant effect on the polarization result, invalidating the attenuation hypothesis. One other possible mechanism that could limit the achievable rubidium polarization involves a possible flaw in the construction or design of the polarization module. Since these contain two $\lambda/4$ plates, it is possible that they are not both perfectly aligned to circularly polarize the laser light. If one or both of the plates allow some amount of linearly polarized light through, there would be some percentage of the light illuminating the cell that would actively depolarize the rubidium by driving transitions out of the $m_s = +1/2$ state. If one the beamsplitter

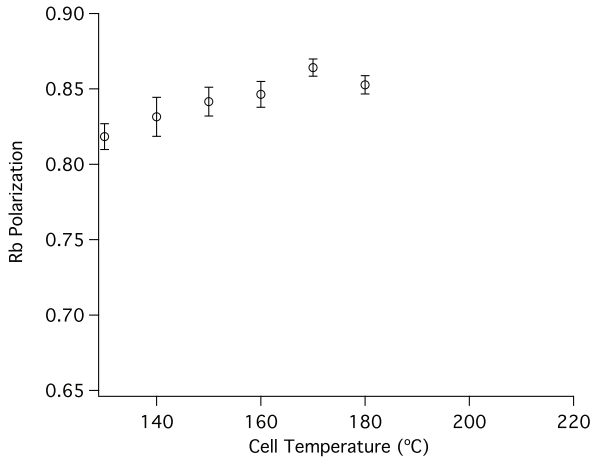

Figure 5.7: The rubidium polarization in OTS-coated cells measured at the same temperatures as were used for the ^{209}Rn coated-cell measurements. The behavior at low temperatures is addressed in the text.

cube does not produce 100% linear polarization in both axes, it would cause a similar effect.

Figs. 5.7 and 5.8 appear to have lower rubidium polarizations at lower cell temperatures. While this indicates the possibility of a small systematic effect, this trend is only present in one point in the uncoated-cell data and, given the size of the error bars, on pair of points in the coated-cell data. We would need to perform more measurements at lower temperatures to confirm that this perceived effect is more than a statistical fluctuation.

5.4 Rubidium Polarimetry Conclusions

As can be seen in Fig. 5.9, there is significant disagreement between the calculated rubidium polarization values and the measured ones. The calculated values approach $P = 1$ as the temperature decreases, while the measured values saturate at around $P = 0.85$. The point where rubidium spin destruction begins to overwhelm the ability of the laser to maintain the polarization occurs at a much higher temperature in the measured values. Since the measurements were done with the same cells and

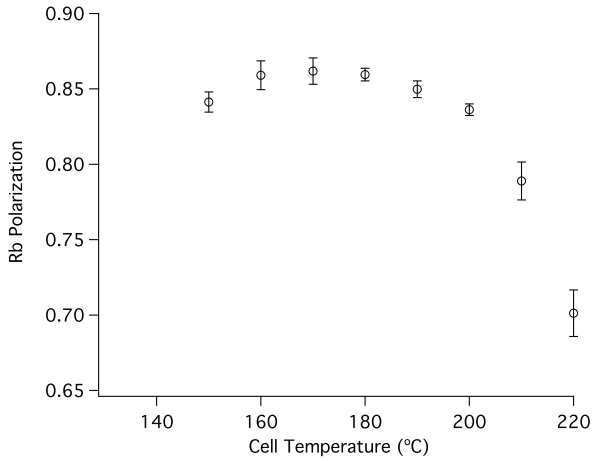

Figure 5.8: The rubidium polarization in uncoated cells measured at the same temperatures as were used for the ^{209}Rn uncoated-cell measurements. The behavior at low temperatures is addressed in the text.

laser as the radon polarization measurements, these rubidium polarization values are much more likely to reflect the rubidium polarization during the radon measurements. Thus, in the analysis of the radon polarization data (discussed in Chapter VII) we used the measured values as inputs for the radon polarization model.

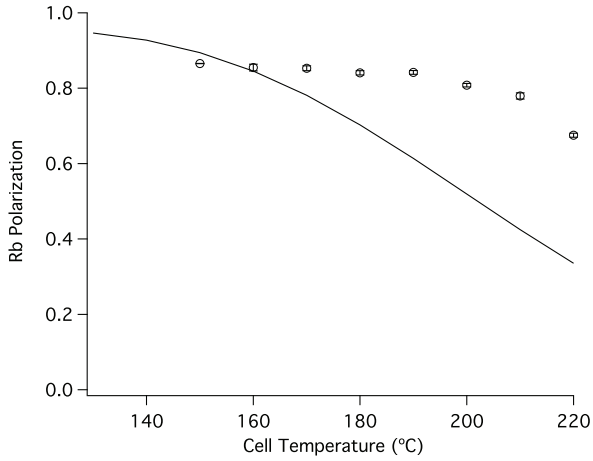

Figure 5.9: The calculated (solid line) and measured rubidium polarization in uncoated cells. The disagreement between the two is discussed in the text.

CHAPTER VI

Radon Polarization Measurements

6.1 Introduction

The TRIUMF ISAC facility cannot produce radon until an actinide target is installed, so we were unable undertake any development work there using ^{221}Rn or ^{223}Rn. SUNY Stony Brook's Nuclear Structure Laboratory (NSL) can produce lighter isotopes of radon through electron capture decay from francium. One particular isotope, ^{209}Rn, has a similar half-life and spin to ^{223}Rn (28.5 min, $I = 5/2$ and 23 min, $I = 7/2$, respectively). This implies that it will be affected by the same wall relaxation mechanisms (both dipole and quadrupole) and that the transfer and measurement procedure will have to be performed over the same time scale. Since ^{209}Fr decays to ^{209}Rn with an 11% branching ratio, we tuned the Stony Brook francium beam for that isotope and constructed an isotope collection and transfer apparatus similar to that used in the xenon collection and transfer tests at TRIUMF. We used glass optical pumping cells in these tests, and studied the polarization and relaxation of ^{209}Rn in order to draw conclusions on what we will be able to achieve with the heavier radon isotopes in an EDM experiment.

6.2 Production and Transport of ^{209}Fr

The NSL featured a van de Graaf generator which could accelerate oxygen isotopes (^{16}O or ^{18}O) to energies on the order of 100 MeV. Collisions with a heated, solid gold target produced francium. By monitoring the α spectrum with a detector in the Francium Lab, we could determine the isotopic content of the beam produced for various energies of either oxygen beam. We found the optimum yield of ^{209}Fr relative to the other francium isotopes in the beam to be for an incident beam of 91 MeV ^{16}O. The francium atoms created in the target are surface ionized, accelerated to 5 keV, and electrostatically focussed into a beam that we implant in a thin zirconium foil. The ^{209}Fr ($T_{1/2} = 50.0$ s) undergoes electron-capture decay to ^{209}Rn while embedded in the foil.

6.3 First Stony Brook Run

Our first attempt to polarize ^{209}Rn at the NSL took place in May of 2005. Due to the combination of high backgrounds, low production rates, and difficulties in efficiently transporting the francium beam from the target to the collection foil, the statistics were such that only one of the four main gamma-ray lines from ^{209}Rn decay displayed evidence of an anisotropy.

6.3.1 Apparatus and Techniques

The only available opening for our equipment on the NSL vacuum system involved connecting to a mini-conflat (CF) flange in the target hall about 4 m from the target chamber. The apparatus is similar to that built for the xenon transfer studies at TRIUMF (see Fig. 4.5), but without a coldfinger for gas transfer. In the Stony Brook measurements, we immerse the cell in liquid nitrogen to transfer the radon,

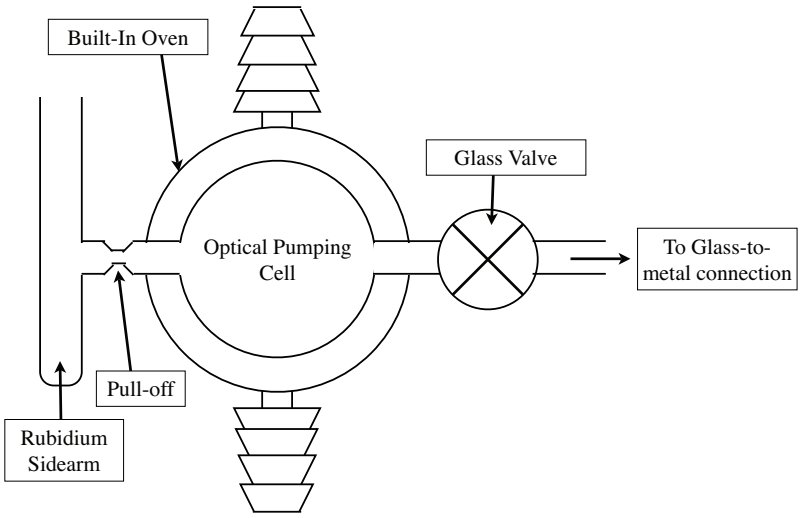

Figure 6.1: A sketch of the optical pumping cells used in the first Stony Brook run. These cells included a built-in oven. All components in the drawing are made of glass, aside from some components of the valve.

since this technique successfully cryopumps close to 100% of the gas released by the foil into the cell. In this apparatus, we use the same gas-handling equipment used at TRIUMF for the nitrogen push to fill the optical pumping cells with the nitrogen buffer gas. We also used the same type of collection foil as in the TRIUMF xenon tests.

Optical Pumping Cells

In this first run at the NSL, the optical pumping cells were glass spheres of about 2.5 cm diameter featuring built-in glass jackets (see Fig. 6.1). The hose barbs on the jacket are for the connection of inlet and outlet tubes for the flow of hot air used to heat the cells to the temperatures desired for optical pumping. To prepare the cells for these measurements, we cleaned, coated, and loaded them with a small amount of natural rubidium at the University of Michigan. The cleaning and coating process, developed by Rosen [Ros99] begins with bathing the cells in piranha solution (30% H_2O_2, 70% H_2SO_4 by volume) for about one hour. We then rinse them sequentially

with deionized water, methanol, and deionized water a second time. We place them under a flow of dry nitrogen for a few hours before filling them with the coating solution. The coating solution contains, by volume, 80% hexane, 12% carbon tetrachloride, and 8% chloroform, with 0.788 cc octadecyltrichlorosilane (OTS) per Liter solution. After filling the cells with this solution such that it wets all surfaces that the radon could contact (except for the pull-off for the rubidium sidearm), we allow five minutes for the coating to bond to the glass. We then drain the solution from the cells, rinse them with chloroform, and place them in an oven at 200°C for at least 16 hours. At this point the cell walls are coated with a thin layer of OTS, which has been shown to be beneficial for the polarization lifetime of species including xenon [Ros99, Bre00].

After the cells have been coated, we mount them on a vacuum system used as a dedicated cell filling station. For each cell, we break open a rubidium ampoule and drop it in the sidearm. We then use an oxy-propane torch to seal off the sidearm, begin pumping on the cell, and use the torch to drive out the impurities created in the rubidium during its exposure to air. Once the vacuum in the cells is satisfactorily clean, we use the torch to chase a small amount of rubidium into the cells, coating the walls with a thin layer, and remove the sidearm at the pull-off. For safety during transport, we backfilled the cells for this run with about 1 atm of nitrogen before closing the glass valve and removing them from the filling station.

Ion Beam Bender

Given the layout of the target hall, to fit our equipment in the space available we were required to bend the francium beam 45° from its direction at the mini-CF flange. To accomplish this, we designed and constructed an electrostatic ion beam bender. Fig. 6.2 shows the schematic of the bender design. Two curved aluminum

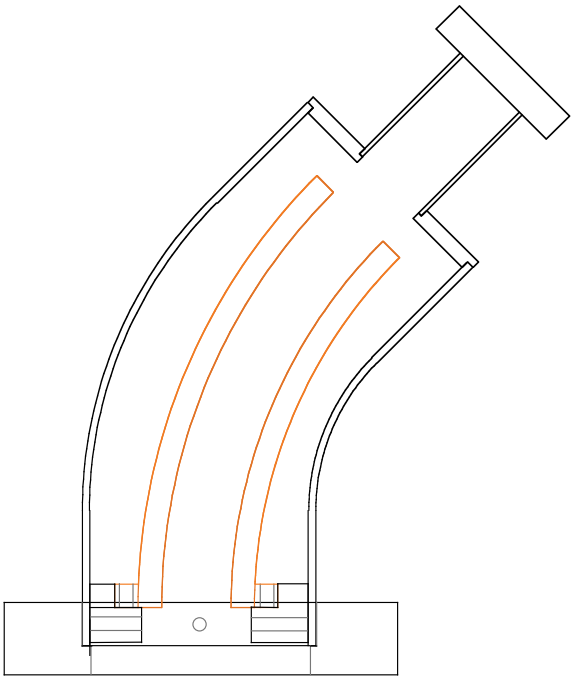

Figure 6.2: A schematic of the beam bender showing the curved electrodes and one of the ceramic spacers used to hold them in place. The spacer shown is designed to allow wires from the voltage supply to be connected to the electrodes without crossing the beam path.

bars held in place by ceramic spacers in a 2"-diameter stainless-steel tube with a 45° curve (MDC 403517) [MDC] provided the electric field used to alter the ion path appropriately. An electric feedthrough allowed these bars to be connected to a pair of high-voltage power supplies (SRS PS300) [Sta].

To determine the expected magnitude of the required voltage difference between the plates, we assume a beam of singly ionized 10 keV francium atoms. If we neglect all edge effects, the field between the electrodes is the same as that between two infinitely long cylindrical shells. For a voltage difference ΔV, this electric field between the plates at a radius r from the central axis is

$$E_r = \left(\frac{\Delta V}{\log(b/a)}\right) \cdot \frac{1}{r}, \tag{6.1}$$

where a and b are the radii of the inner and outer cylinders, respectively. For a

charged particle to travel in a circle, the electric force, qE_r, must equal the centripetal force mv^2/r. For a non-relativistic kinetic energy K, the centripetal force can be rewritten as $2K/r$ and so the voltage difference must be

$$\Delta V = \frac{2K}{q} \log(b/a). \tag{6.2}$$

This provided a starting point for the bender electrode voltages in the beam tuning procedure.

To reach our foil, the francium beam must be directed from the target through the mini-conflat port and around the bender to the collection foil. In order to optimize the transmission to the foil, we tuned the beam optics using rubidium ions. A rubidium source near the target generated a stable beam that followed the path the francium would take. We connected a picoammeter to the foil and adjusted the voltages of the various electrostatic lenses and benders upstream of the mini-conflat port as well as the voltages of the electrodes in our bender to maximize the current reading.

Data Collection

The extrema of the angular distributions of the four main gamma rays (see Table 6.1) emitted following the electron capture decay of polarized ^{209}Rn to excited states of ^{209}At will be at 0° and 90° with respect to the polarization direction (the magnetic

Table 6.1: The four main ^{209}Rn gamma ray lines [Shi96] (from the Table of Isotopes) listed together with the corresponding absolute intensity I_γ, spin transition, intensity distribution equation, and multipole mixing ratio (δ).

E_γ (keV)	I_γ (%)	Spin Transition	Eqn. #	δ (Ref. [Shi96])
337.45	14.5	7/2→7/2	7.16	∞
408.32	50.3	7/2→9/2	7.11	0
689.26	9.7	7/2→7/2	7.16	>3.57
745.78	22.8	7/2→9/2	7.11	>2.86

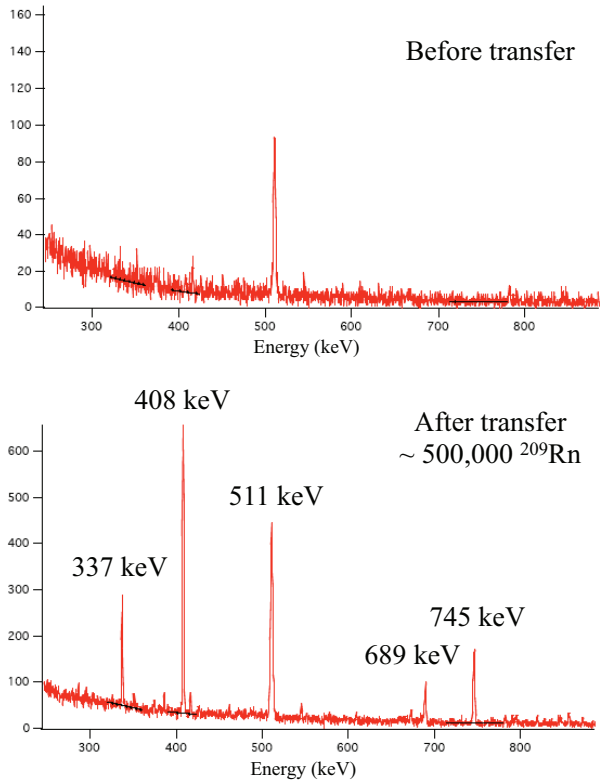

Figure 6.3: Gamma ray spectra from a detector observing the cell, before (a) and after (b) transferring ^{209}Rn.

field direction). Thus, we placed high-purity germanium (HPGe) detectors at those angles, a few inches from the cell. We collimated the detectors with lead. The francium creation process produces a large amount of neutrons in the target hall, so in order to protect the detectors we shielded them from the target with blocks of paraffin and borated lead. Also, the neutron activity made it impossible for us to remain in the target hall during the implantation process. We tuned the beamline to our foil, left the target hall, initiated francium production, and implanted the francium in the foil for about two half-lives of ^{209}Rn ($T_{1/2}$ = 28.5 min). At that point we ceased francium production and reentered the target hall to make use of the collected ^{209}Rn sample.

The transfer process was essentially the same as the calibration transfers in the

TRIUMF xenon studies, the only differences being a more complicated cell geometry and a horizontal transfer tube. We oriented the cells such that one of the hose barbs on the jacket faced downward. This allowed us to place a liquid nitrogen container around the lower half of the oven such that the LN2 would flow into it through the hose barb, cooling the bottom of the cell. As before, we resistively heated the foil to drive out the ^{209}Rn and cryopumped it into the cell. As illustrated by Fig. 6.3, we could easily confirm the presence of ^{209}Rn in our measurement cells following this process. After the ^{209}Rn transfer, we filled the cells with a few hundred torr N_2 (measured with half the cell immersed in liquid nitrogen) from the gas handling system, removed the LN2, and heated the cell to about 130°C.

A pair of helmholtz coils centered on the cell provided an acceptably uniform magnetic field of about 10 gauss. A fiber optic cable carried laser light from a Coherent FAP system to a polarization module. This module was developed by Todd Smith [Smi98]. The components of the module were a collimation lens, a polarizing beamsplitter cube, a mirror, and two quarter-wave plates. These were arranged such that collimated laser light was split into two linearly polarized beams by the cube. One of these passed through the first $\lambda/4$-plate, becoming circularly polarized. The other reflected off the mirror at a 90° angle, switching the orientation of its linear polarization such that, after passing through the second $\lambda/4$-plate, it had the same circular polarization as the first half. We directed both of these beams such that the entire optical pumping cell was illuminated with circularly polarized light centered at the Rb-D1 frequency of 794.8 nm. This was meant to polarize the ^{209}Rn in the cell through the spin-exchange process discussed in Chapter III.

For each ^{209}Rn sample, we collected gamma-ray spectra from both detectors monitoring the measurement cell for periods with the laser on and the laser off. This

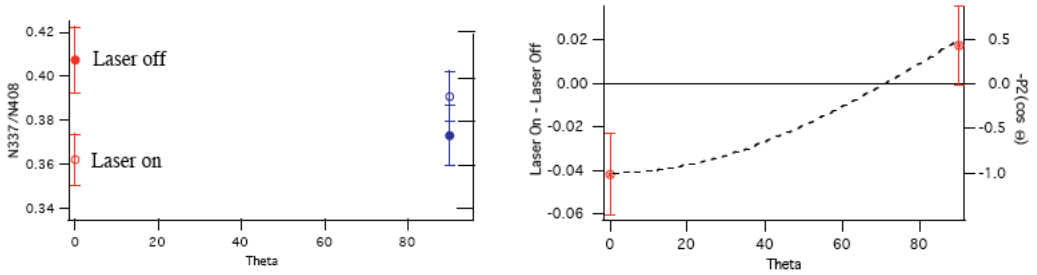

Figure 6.4: The polarization signal in the 337 keV gamma-ray line (relative to the 408 keV line) from the first Stony Brook run, showing a difference in the signal when the optical pumping laser was on or off. The angular gamma-ray intensity would be expected to have a $P_2(\cos\theta)$ dependence.

provided gamma-ray rates for polarized and unpolarized ^{209}Rn. If we successfully polarized the ^{209}Rn, we should be able to see a change in the 0° and 90° rates when the laser was on or off.

6.3.2 Conclusions

The gamma-ray statistics in this run were such that only the 337 keV line showed evidence of ^{209}Rn polarization. This is shown in Fig. 6.4. We normalized the 337 keV line to the 408 keV counts, since earlier measurements [Kit88] showed that the 408 keV gamma rays had no significant anisotropy. In order to study the relaxation of ^{209}Rn polarization, we need to be able to measure different anisotropies at different temperatures, which requires more precision than is possible with the statistics generated by the first run. Increasing the francium production at the gold target was a possibility, but that depends on the individual gold target used and a willingness to increase the ^{16}O current and the target temperature to the point where we would be in danger of destroying the gold target. The use of more efficient HPGe detectors could provide a significant improvement, but would require the exposure of these more-valuable detectors to the high neutron backgrounds of the target hall, possibly damaging them.

The beam optics for the path from the target to the Francium Lab had been well developed by the time we made these measurements. By comparing the rubidium current at our foil during the tuning procedure with what could be observed at a collector in the Francium Lab, we concluded that we were transporting between 1/5 and 1/3 of the francium produced at the target to our foil. Thus, one of the main avenues for increasing our statistics was seen to be to improve the transport efficiency. A scan of the francium beam's path from the target to our collector foil using a geiger counter revealed two locations with approximately equal deposited activity: the collection foil and the mini-conflat port. In order to improve our transport efficiency, we would need to move the apparatus to a position where the francium beam would not have to pass through such small restrictions in order to reach the collection foil.

6.4 Second Stony Brook Run

By December of 2005, the experiments using the francium trap at Stony Brook had been completed and the equipment removed, providing a beamline access point for our apparatus with optimized francium beam optics. Since the apparatus would be located in the Francium Laboratory instead of the target hall, we could use more efficient HPGe detectors without worrying about possible neutron damage. Thus we expected a significant improvement in our gamma-ray statistics in this second run.

6.4.1 Apparatus and Techniques

We built the apparatus shown in Fig. 6.5 at the end of the francium beamline in the Stony Brook Francium Laboratory. In this run, the optical pumping cell was an uncoated glass sphere of about 2.5 cm radius preloaded with a small amount of rubidium. Studies of the relaxation of ^{131}Xe [Wu90] indicated that wall coatings

shorten the polarization lifetimes of atoms that experience quadrupole interactions with the cell walls (atoms with $I \geq 1$), so for this run we prepared the cells without undertaking the OTS-coating step. The HPGe detectors in this run were a 120%-efficient (vs 3"×3" NaI) Eurisys Clover $4 \times 50 \times 80$ Seg 2 at 0° and a 50% efficient Ortec Model GMX50-S at 90° with respect to the magnetic field direction.

The built-in oven in the previous cell design had proved inconvenient for the cryopumping process in the first run, so we built a glass clamshell oven to fit around the cell in the second one. This was essentially a cylinder cut in two, with an opening for the cell neck and two hose barbs for heated air flow. It was removed to allow us to immerse the cell in liquid nitrogen, and oriented such that the cylinder's axis was along the magnetic field direction. Thus, during the optical pumping process, the circularly polarized light would enter through one of the flat plates at either end of the oven, minimizing beam distortion.

As a general diagnostic test of our optical pumping system, we performed an adiabatic fast passage (AFP) NMR measurement on each cell used for these polarization studies when they were first mounted on the apparatus. We filled the cells with about 100 torr natural xenon and about 1 atm N_2 (pressures measured at about 20°C). We placed pick-up and RF coils around the cell, with both pairs of coils perpendicular to each other and to the magnetic field axis. We applied a 10 kHz signal to the RF coils and swept the magnetic field through the ^{129}Xe resonance, obtaining an AFP spectrum like that shown in Fig. 6.6. After this check, we pumped out the nitrogen and xenon in the cell before proceeding to the radon polarization measurement procedure.

When the francium trap was in place, the francium beam was tuned using a faraday cup that could be moved into and out of the beam path. An α-detector below

the cup allowed the isotopic composition of the beam to be monitored. We used this cup in our tuning procedure, optimizing the transmission of a stable rubidium beam, then moving the cup out of the beam path and tuning to the collection foil.

As before, we implanted the francium beam for about two half-lives of ^{209}Rn. Once we had collected a sample, we transferred it into the optical pumping cell by the following procedure. We moved the faraday cup back into the beam path, blocking the francium, and closed valve V1 (see Fig. 6.5). We closed the valve above the turbopump, resistively heated the foil to above 1000°C, and immersed the cell in liquid nitrogen. We left the foil and the cell at these temperatures for 2 minutes to ensure that all of the released ^{209}Rn would freeze into the cell. Afterwards, we ceased heating the foil, closed valve V2, and opened valve V6 to introduce about 500 torr purified N_2 gas into the cell, which remains immersed in LN2. We then close valve V4, remove the liquid nitrogen, place the clamshell oven around the cell, and heat it to the desired temperature.

To make the most out of each ^{209}Rn sample, we began collecting laser-off data with the HPGe detectors while heating the cell, as the 0° and 90° gamma-ray rates should be unaffected by the rubidium density. Once the cell was at the desired temperature, we began alternating between laser-on and laser-off spectra. We attempted to set the lengths of these segments such that they each contained the same number of ^{209}Rn decays, as determined by the number of counts in the 408 keV peak. A single ^{209}Rn sample usually generated four such segments.

6.4.2 Data and Conclusions

The various improvements made for the second run resulted in a better than two-fold improvement in the count rates seen by the HPGe detectors. Fig. 6.7 shows spectra from the 0° detector before and after the transfer of ^{209}Rn from the foil to

the cell, demonstrating the successfulness of this process. It also illustrates that, although we placed some lead shielding between the foil and the detectors, we could still observe activity located at the foil during the implantation process. The 719 keV line in the upper panel of Fig. 6.7 indicates the presence of ^{205}At. Since this is a product of ^{209}Fr α-decay (89% b.r.) and the small amount of ^{209}Fr remaining in the foil by the time we began heating it would not diffuse out with the ^{209}Rn, we conclude that the observed ^{205}At must be imbedded in the foil.

The details of the data analysis will be covered in Chapter VII, but part of the motivation for the third Stony Brook run is best illustrated using the results of the second run, shown in Fig. 6.8. The 337 and 745 keV gamma-ray count-rate ratios deviate from unity in the expected directions, but they appear to be increasing with temperature. As we increase the cell temperature the rubidium polarization should, at some point, begin decreasing rapidly (see Chapter V), leading to a corresponding decrease in the ^{209}Rn polarization. Quadrupole relaxation should have the opposite effect, decreasing (to a non-zero value) as the cell temperature increases. So, we would expect the ^{209}Rn polarization to increase with temperature up to the point that the effect of the decreasing rubidium polarization outweighs that of the weakening quadrupole wall interactions. The polarization would turn over at some temperature, and the ratio calculated for Fig. 6.8 would return to one as the cell temperature increased beyond that point. It should be easier to extract information on the ^{209}Rn relaxation parameters if the polarization data turns over in this manner. Based on the second-run data, we concluded that we would need to reach higher cell temperatures to see this effect.

These measurements used only uncoated cells, so we could not verify that the conclusions of Ref. [Wu90] for ^{131}Xe apply to ^{209}Rn as well. The possibility of deter-

mining for ourselves whether or not cell coatings are beneficial for radon polarization in isotopes experiencing quadrupole wall interactions provided further motivation for a third data run.

6.5 Third Stony Brook Run

We returned to Stony Brook in June of 2006 for a third data run incorporating the changes discussed above. The equipment we used in this run was, for the most part, identical to that used in the second run (see Fig. 6.5). Instead of using one Eurisys and one Ortec HPGe detector as in the second run, we used two 100% Ortec detectors. Alterations to the mounting platforms for these detectors allowed us to place them closer to the cell (about 2 inches away for both the 0° and 90° detectors), increasing the count rates.

We obtained data (presented in Chapter VII) for both coated and uncoated cells using the same procedure as in the second run. Due to concerns about the possibility of damaging the coatings at high temperatures, we began collecting coated-cell data at a lower temperature (130°C) than had been used for the uncoated cells and increased the temperature in 10°C increments for subsequent runs. This resulted in the collection of coated-cell data from 130°C to 180°C during our scheduled beamtime. We performed uncoated-cell measurements from 150°C to 220°C in the hope of seeing the polarization signal turn over.

A few alterations to the oven heating apparatus were necessary in order to reach the higher temperatures used in the uncoated-cell measurements. In the second run, a silicon rubber tube connected the air heater to the oven, attaching at both ends with hose barbs. This material melts at around 200°C, an effect evinced in the second run by the ejection of small bits of rubber from the tube into the oven when

operating at 200°C. It was clear that the tube could not sustain higher temperatures, so we switched to a stainless steel bellows running from the air heater to the oven. We built a new oven identical to that used in the second run except that the air inlet and outlet were 1/2-inch diameter glass tubes instead of hose barbs. We connected the bellows to the inlet tube with a compression fitting with a Kalrez O-ring, which could sustain the temperatures we wished to achieve.

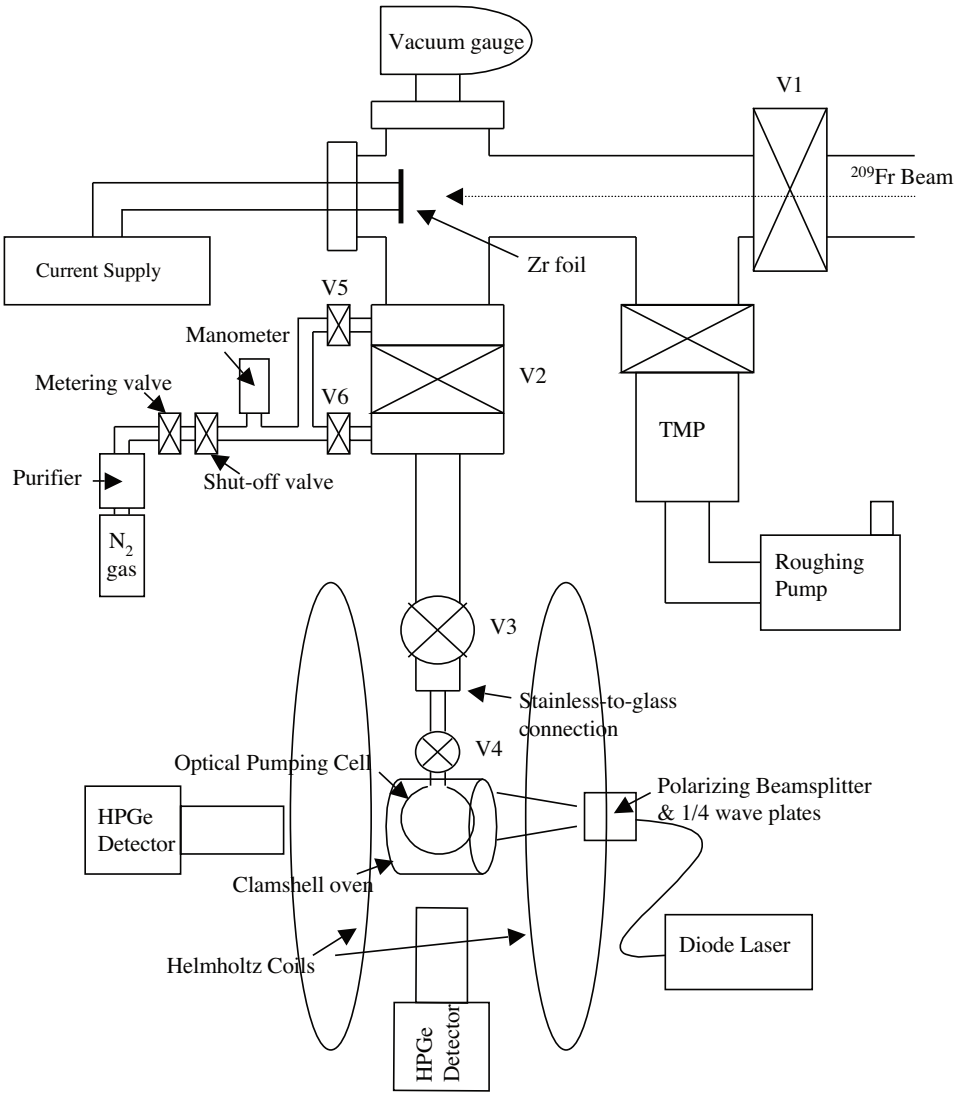

Figure 6.5: A sketch of the apparatus used in the second and third radon polarization runs at Stony Brook.

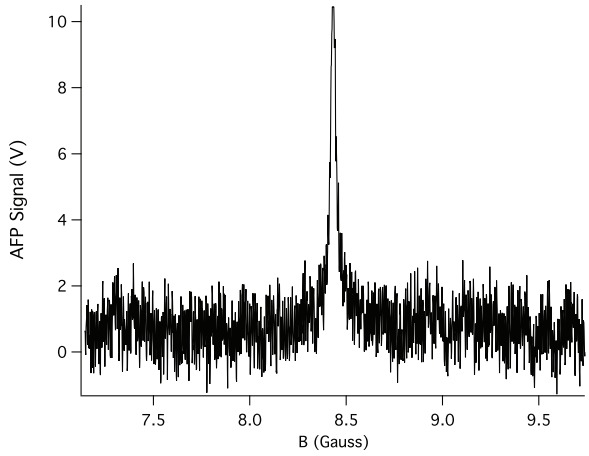

Figure 6.6: An example AFP diagnostic sweep, demonstrating the successful polarization of ^{129}Xe using our optical pumping apparatus.

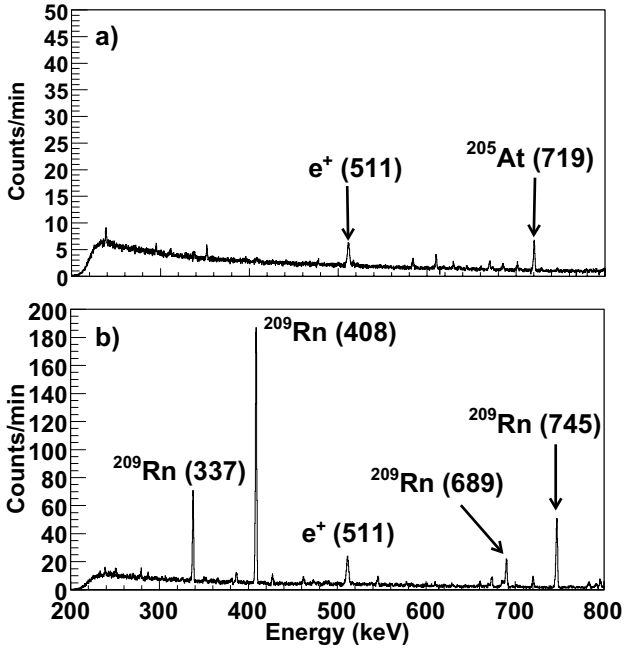

Figure 6.7: Gamma-ray spectra from the 0° detector. Spectrum a) was taken over about an hour during the implantation of the ^{209}Fr beam in the Zr foil and b) was taken over the first ten minutes after transfer of the ^{209}Rn to the optical pumping cell. Note the different vertical scales.

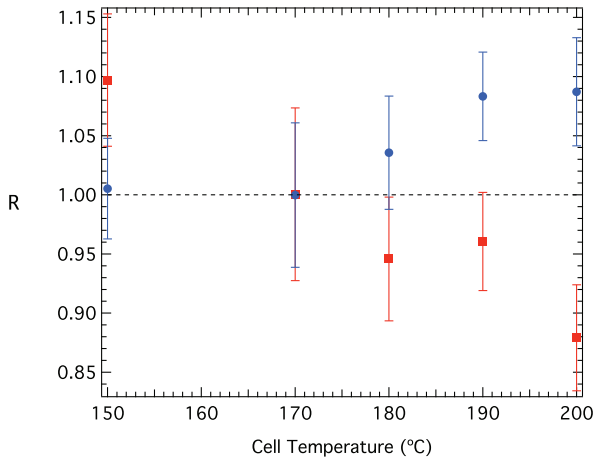

Figure 6.8: A plot of the laser-on to laser-off ratios of the 0°/90° count-rate ratios for the 337 keV line (red squares) and the 745 keV line (blue circles) vs. optical pumping cell temperature.

CHAPTER VII

Radon Polarization Data Analysis

7.1 Introduction

We used the gamma-ray spectra obtained in the second and third Stony Brook runs, described in Chapter VI, to obtain information on the polarization and relaxation properties of ^{209}Rn. The data from the first run was taken at one cell temperature only, since the main goal of that run was to obtain a ^{209}Rn polarization signal. This prevents it from being used in the later polarization and relaxation studies, which require an investigation of the temperature dependence of the polarization signal. Due to the fact that the experimental procedure and apparatus for the second and third Stony Brook runs were almost identical, and that the method of analysis for the anisotropies was such that any differences in detector positioning and sensitivity could be canceled out, we combined the data from these two runs in the following analysis. We construct a model that connects the observed anisotropy signal to a set of polarization and relaxation parameters, and perform a grid search over a reasonable range of these parameters to find the corresponding best-fit relaxation rates. Taking this rate as an indicator of the properties we could expect for ^{223}Rn, we can estimate the expected polarization coherence lifetime, T_2, of ^{223}Rn. This allows us to predict the expected precision of a ^{223}Rn EDM experiment.

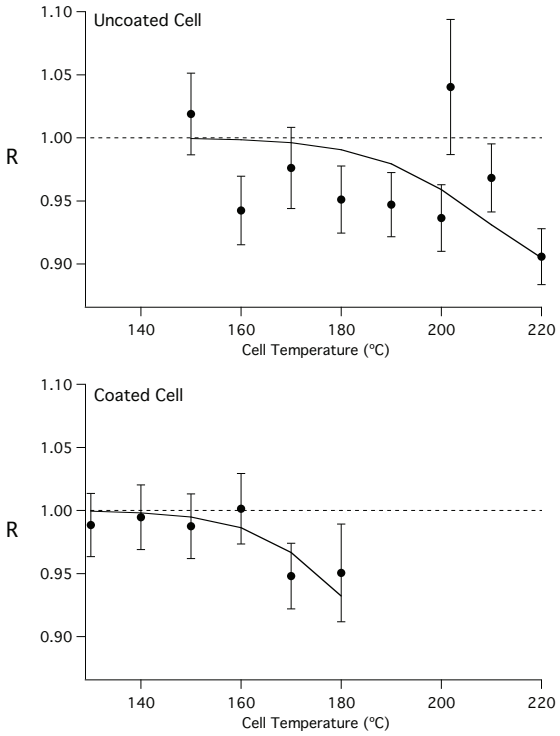

Figure 7.1: Anisotropy data from the coated and uncoated cells for the 337 keV ^{209}Rn gamma ray. For the uncoated cell the average of Runs 2 and 3 is displayed. R is the ratio defined in Eq. 7.1, and the solid curves represent the fits, described in the text, from which a value for Γ_2^∞ is obtained.

7.2 Radon Polarization Data

As was discussed in Chapter VI, we split the data from each sample of ^{209}Rn into alternating laser-on and laser-off segments. For each gamma-ray line, we combine the data at 0° and 90° into an anisotropy ratio

$$R = \frac{(N_{0^\circ}/N_{90^\circ})_{\mathrm{LON}}}{(N_{0^\circ}/N_{90^\circ})_{\mathrm{LOFF}}}. \tag{7.1}$$

N_{0° (N_{90°) is the number of gamma rays detected at the 0° (90°) detector and LON (LOFF) indicates data taken with the laser on (off). This ratio is independent of the relative solid angles and efficiencies of the two detectors, assuming that they don't change over the course of a data-collection segment. We use the data from one

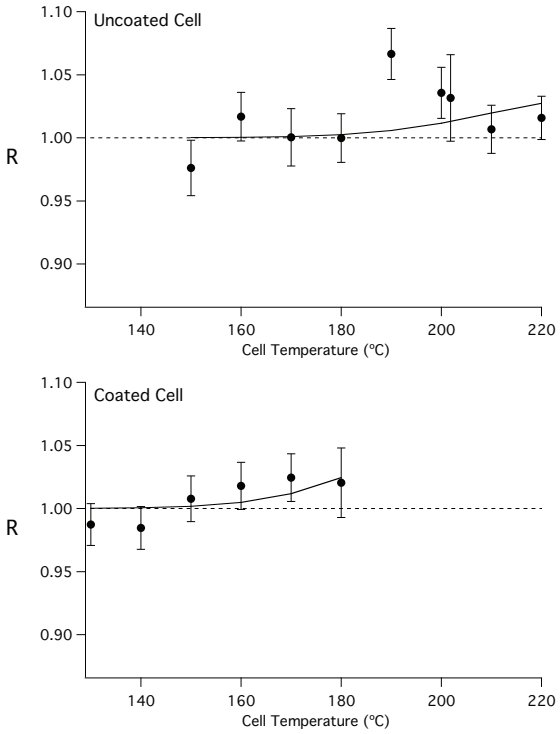

Figure 7.2: Anisotropy data for the 745 keV ^{209}Rn gamma ray displayed in the same manner as the 337 keV data in Fig. 7.1. The solid curves represent fits to the mixing ratio δ given the value of Γ_2^∞ obtained from the 337 keV data in the corresponding cell type, as described in the text.

sample to obtain an R value for each of the gamma-ray lines under investigation, then average these results with those from all other samples measured at the same temperature in the same cell type (*i.e.*, coated or uncoated). The results of this process for the 337 and 745 keV lines are the data presented in Figs. 7.1 and 7.2.

We used a simple counts-above-background method to determine the number of 337 and 745 keV gamma rays detected in each segment. The data for these segments were contained in spectra like that shown in Fig. 7.3. Aside from a few peaks, the backgrounds around these two ^{209}Rn gamma-ray peaks were essentially linear. So, we fit the region from 320 to 370 (710 to 820) keV to a line to determine the background level around the 337 (745) keV peak. We excluded the bins in the peak

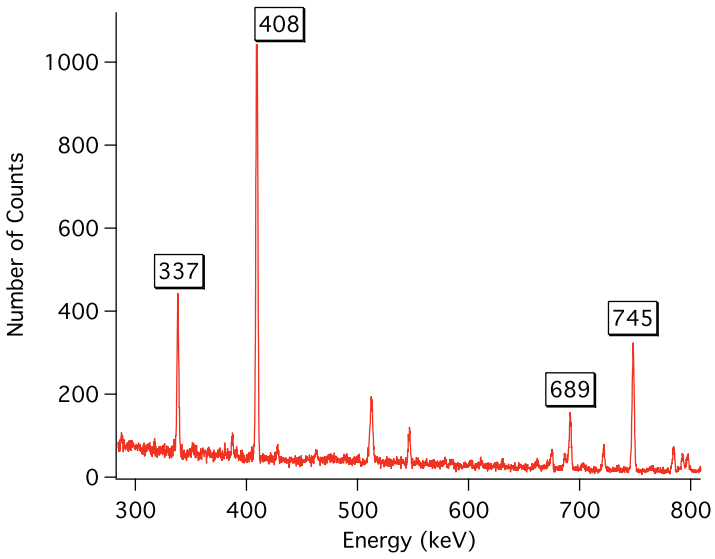

Figure 7.3: An HPGe spectrum with the four main ^{209}Rn gamma-ray lines labeled. This data is from the 0° detector in the first 10 minutes after transferring ^{209}Rn into the cell during the June run.

regions (including both the ^{209}Rn peaks of interest and other background peaks) from the background fit. We defined a peak region as all points within 3.5σ from the center of a peak, where the peak centroid and σ were determined by a fit to a gaussian function on a linear background. We performed a background subtraction in the ^{209}Rn peak regions using the value of the background function at the center of each bin, then summed the counts in the peak region to determine the total number of gamma rays detected. The errors in these numbers are a combination of the errors in the two background fit parameters and the poisson statistical error in the gamma-ray counts per energy bin. In order to accurately model the shape of a gamma-ray peak in an HPGe detector, the Radware [Rad] program uses a function with three components, a Gaussian, a skewed Gaussian, and a smoothed step function. While we could remove the second and third parts of this function and just fit our peaks to a Gaussian on a linear background, this would still introduce three more fitting parameters than the counts-above-background method. We are only interested in

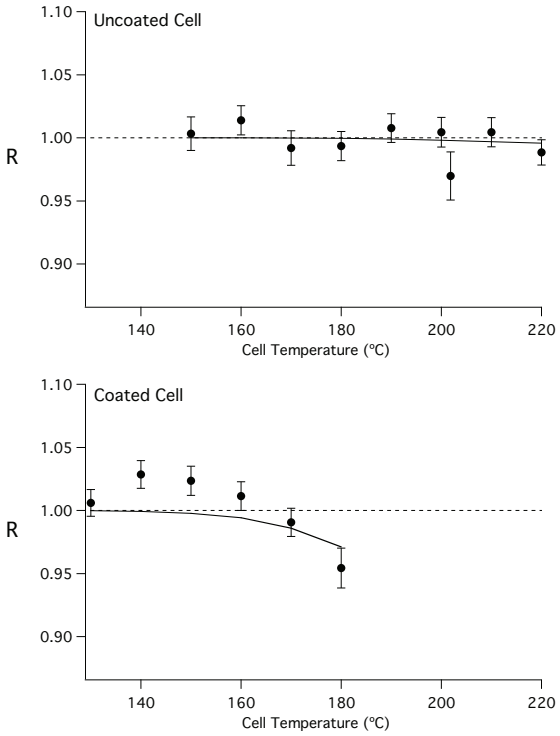

Figure 7.4: Anisotropy data for the 408 keV ^{209}Rn gamma ray. The solid curves represent fits to the mixing ratio δ given the value of Γ_2^∞ obtained from the 337 keV data in the corresponding cell type, as described in the text.

the total number of gamma-rays detected, so a more complex fit is unnecessary.

As illustrated by Fig. 7.4, the 408 keV line displayed no anisotropy in our measurements. This is clear in the uncoated cell data, where the data points never stray significantly from the $R = 1$ null-signal value. While the coated-cell data has multiple points located more than 1σ from $R = 1$, they exist on both sides of the null-signal line. This is physically impossible for a gamma-ray anisotropy, so these deviations cannot be attributed to an effect of ^{209}Rn polarization. Further complications in the analysis of the 408 keV data arose from the presence of a ^{152}Eu calibration source in the Francium Laboratory in the second Stony Brook run. It was intended to provide a benchmark that could be used to determine whether or not the detector

efficiencies were changing over the course of a data collection segment. ^{152}Eu has gamma ray lines at energies near the main ^{209}Rn lines (344, 411, 679, and 779 keV), allowing us to look for energy-dependent changes in detection efficiency. Since we saw no evidence of this, we performed the third run without the ^{152}Eu source. The proximity of the 411 keV line to the ^{209}Rn 408 keV line introduced a complication to the data analysis, since the peaks overlapped the second-run spectra. Thus, we were forced to perform a two-peak fit to be able to subtract both the background and 411 keV gamma rays from the 408 keV peak. This introduced more uncertainty to the determination of the number of 408 keV gamma rays detected in those spectra.

The fact that the 411 keV peak was very small relative to the 408 keV peak allowed it to be treated as part of the background, and any error in the determination of the number of counts to attribute to the 411 keV peak was a small fraction of the total number of 408 keV gamma-ray counts. The presence of a large ^{208}At peak at 686 keV made it impossible to accurately determine the number of counts in the double peak to attribute to ^{208}At versus the 689 keV ^{209}Rn gamma ray. In addition to ^{209}Fr, the other main component of the francium beam implanted in the collection foil to generate our ^{209}Rn samples was ^{208}Fr, which undergoes electron capture decay to ^{208}Rn with a 10% branching ratio and a 59.1 sec half-life. When we transfer the noble gas from the foil to the measurement cell, ^{208}Rn ($T_{1/2}$ = 24.35 min) is transferred along with the ^{209}Rn, and as it decays the ^{208}At ($T_{1/2}$ = 1.63 h) daughter atoms are deposited on the cell walls. These atoms remain when we pump out the gas in the cell between radon samples, so as the run progressed the 686 keV peak increased in size. Thus, we did not attempt to calculate R values for the 689 keV peak, focussing only on the 337, 408, and 745 keV peaks.

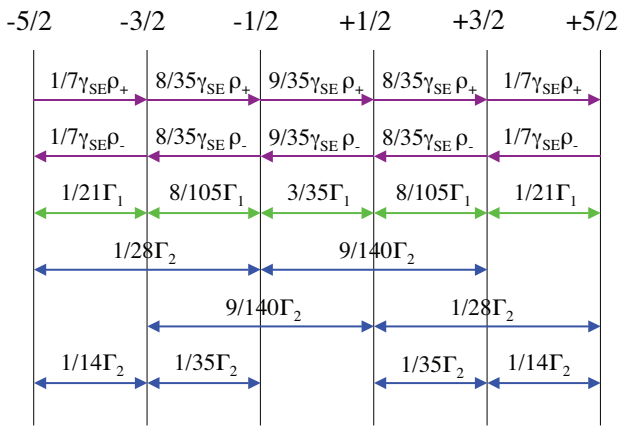

Figure 7.5: A diagram of the rates that determine the populations of the ^{209}Rn nuclear sublevels, labeled by their spins. The quantities $\rho_{\pm}$ are the functions of the rubidium polarization defined in Eq. 7.5.

7.3 Radon Polarization Model

The model used to interpret the radon polarization data depends on the following parameters: the quadrupole relaxation rate Γ_2^{∞}, the wall binding temperature T_0, the spin-exchange cross section σ_{SE}, the rubidium polarization $\bar{P}_{\mathrm{Rb}}$, the multipole mixing ratio δ, and the cell temperature T. A set of rate equations determine the equilibrium radon sublevel populations from the combined effects of spin-exchange collisions with polarized rubidium and quadrupole relaxation processes. We insert these population expressions into the angular distribution functions corresponding to the observed gamma ray transitions.

7.3.1 Spin Exchange

Collisions between alkali-metal and noble gas atoms result in the transfer of polarization from one species to the other [Wal97], characterized by the spin-exchange rate [App98]

$$\gamma_{\mathrm{SE}} = [\mathrm{Rb}]\langle \sigma_{\mathrm{SE}} v \rangle. \tag{7.2}$$

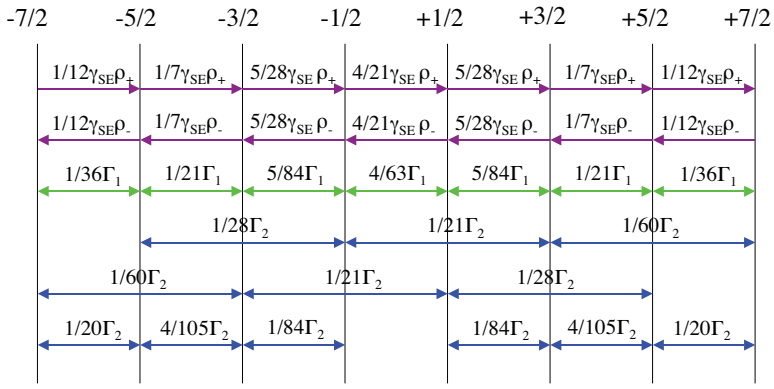

Figure 7.6: A diagram of the rates that determine the populations of the ^{223}Rn nuclear sublevels, labeled by their spins. The quantities $\rho_{\pm}$ are the functions of the rubidium polarization defined in Eq. 7.5.

Using Eq. 5.9 for the number density of rubidium atoms as a function of cell temperature, we find

$$\gamma_{\mathrm{SE}} = \frac{(\sigma_{\mathrm{SE}} * 2.8141 \times 10^{33}) \times 10^{-\frac{4040}{T}}}{\sqrt{T}}. \tag{7.3}$$

The spin-exchange cross section, σ_{SE}, for the Rb-^{209}Rn system has been estimated by Walker [Wal89] to be 2.5×10^{-5}Å^2 but is left as a free parameter in this model. No estimates for σ_{SE} for the Rb-^{223}Rn system currently exist.

The populations of the radon nuclear sublevels are affected by dipole (Γ_1) and quadrupole (Γ_2) wall relaxation rates as illustrated in Figs. 7.5 and 7.6. We normalize these rates so that the sum of all transitions of the same multipolarity add to the corresponding relaxation rate. The spin-exchange transition is a dipole transition that always results in a change of sublevel, and collisions with spin-up rubidium atoms are considered distinct from those with spin-down atoms. Studies of ^{131}Xe and ^{21}Ne [Wu90, Chu90] have shown that quadrupole relaxation induces a much stronger effect on the polarization than does dipole relaxation, so we set Γ_1 to zero for simplicity. The rate equations define a set of first-order linear differential equations for the sublevel populations, p_i, of the form $dp_i/dt = R_{ij}p_j$. For ^{209}Rn, the matrix

R_{ij} to be solved is

(7.4)
$$\begin{pmatrix} -\frac{1}{7}\gamma_{\rm SE}\rho_- - \frac{3}{28}\Gamma_2 & \frac{1}{7}\gamma_{\rm SE}\rho_+ + \frac{3}{42}\Gamma_2 & \frac{3}{84}\Gamma_2 & 0 & 0 & 0 \\ \frac{1}{7}\gamma_{\rm SE}\rho_- + \frac{3}{42}\Gamma_2 & -\gamma_{\rm SE}\rho_1 - \frac{23}{140}\Gamma_2 & \frac{8}{35}\gamma_{\rm SE}\rho_+ + \frac{1}{35}\Gamma_2 & \frac{9}{140}\Gamma_2 & 0 & 0 \\ \frac{3}{84}\Gamma_2 & \frac{8}{35}\gamma_{\rm SE}\rho_- + \frac{1}{35}\Gamma_2 & -\gamma_{\rm SE}\rho_2 - \frac{9}{70}\Gamma_2 & \frac{9}{35}\gamma_{\rm SE}\rho_+ & \frac{9}{140}\Gamma_2 & 0 \\ 0 & \frac{9}{140}\Gamma_2 & \frac{9}{35}\gamma_{\rm SE}\rho_- & -\gamma_{\rm SE}\rho_3 - \frac{9}{70}\Gamma_2 & \frac{8}{35}\gamma_{\rm SE}\rho_+ + \frac{1}{35}\Gamma_2 & \frac{3}{84}\Gamma_2 \\ 0 & 0 & \frac{9}{140}\Gamma_2 & \frac{8}{35}\gamma_{\rm SE}\rho_- + \frac{1}{35}\Gamma_2 & -\gamma_{\rm SE}\rho_4 - \frac{23}{140}\Gamma_2 & \frac{1}{7}\gamma_{\rm SE}\rho_+ + \frac{3}{42}\Gamma_2 \\ 0 & 0 & 0 & \frac{3}{84}\Gamma_2 & \frac{1}{7}\gamma_{\rm SE}\rho_- + \frac{3}{42}\Gamma_2 & -\frac{1}{7}\gamma_{\rm SE}\rho_+ - \frac{3}{28}\Gamma_2 \end{pmatrix},$$

where

(7.5)
$$\rho_\pm = (1 \pm \bar{P}_{\rm Rb})/2,$$

(7.6)
$$\rho_1 = \frac{1}{70}(13 - 3\bar{P}_{\rm Rb}),$$

(7.7)
$$\rho_2 = \frac{1}{70}(17 - \bar{P}_{\rm Rb}),$$

(7.8)
$$\rho_3 = \frac{1}{70}(17 + \bar{P}_{\rm Rb}),$$

and

(7.9)
$$\rho_4 = \frac{1}{70}(13 + 3\bar{P}_{\rm Rb}).$$

A similar matrix could be constructed for ^{223}Rn. Wall relaxation is modeled by an Arrhenius-type temperature dependence [Hap72] such that

(7.10)
$$\Gamma_2(T) = \Gamma_2^\infty e^{T_0/T},$$

where T_0 is the wall-binding energy of the noble gas divided by Boltzmann's constant. The equilibrium solution provides each sublevel population in terms of $\bar{P}_{\rm Rb}$, $\sigma_{\rm SE}$, T_0, and Γ_2^∞.

7.3.2 Gamma Ray Anisotropies

In this work, the observed gamma rays are emitted from transitions between excited states of ^{209}At following the electron-capture decay of the polarized ^{209}Rn. Given p_i, we can write expressions for the angular distribution of the gamma rays emitted following the decay of the noble gas. As given by Ref. [Har54], the gamma-ray intensity as a function of the angle with respect to the direction of the nuclear spin for $J_f = J_i + 1$ is

$$W(\theta) = 1 + \frac{1}{14}\left(21\frac{\delta^2}{1+\delta^2} - 42A\frac{\delta}{1+\delta^2} + 15\frac{J_i+6}{J_i}\frac{1}{1+\delta^2}\right) M_2 f_2 P_2 + 10\frac{2J_i+5}{J_i}\frac{1}{1+\delta^2} M_4 f_4 P_4, \tag{7.11}$$

where $M_2 = J_i^2/((J_i+1)(2J_i+3))$, $M_4 = J_i^4/((J_i+1)(J_i+2)(2J_i+3)(2J_i+5))$,

$$A = \sqrt{\frac{15(J_i+2)}{J_i}},$$

and the moments of the populations enter through the f_n's,

$$f_2 = \frac{1}{J_i^2}\left(\sum_i m_i^2 a_i - \frac{1}{3}J_i(J_i+1)\right) \tag{7.12}$$

and

$$f_4 = \frac{1}{J_i^4}\left(\sum_i m_i^4 a_i - \frac{1}{7}(6J_i^2+6J_i-5)\sum_i m_i^2 a_i + \frac{3}{35}J_i(J_i-1)(J_i+1)(J_i+2)\right). \tag{7.13}$$

Here a_i and m_i are the population of the ith sublevel and the spin of that sublevel, respectively. The a_i's are related to the p_i's through the appropriate Clebsh-Gordan coefficients. The P_n's are legendre polynomials:

$$P_2 = \frac{1}{2}(3\cos^2\theta - 1) \tag{7.14}$$

and

$$P_4 = \frac{1}{8}(35\cos^4\theta - 30\cos^2\theta + 3). \tag{7.15}$$

The distribution is normalized such that $\int W(\theta)d\Omega = 4\pi$. The multipole mixing ratio δ is defined by the equation $\delta^2 = \mathrm{A}_1^2/\mathrm{A}_2^2$, where $\mathrm{A}_1 = 1$ in a pure dipole transition, $\mathrm{A}_2 = 1$ in a pure quadrupole transition, and $\mathrm{A}_1^2 + \mathrm{A}_2^2 = 1$. For $J_f = J_i$,

$$W(\theta) = 1 + \frac{1}{14}\left(-21\frac{\delta^2}{1+\delta^2} + 126B\frac{\delta}{1+\delta^2} + 15C\frac{1}{1+\delta^2}\right)K_2 f_2 P_2 - \frac{30}{(2J_i+3)(2J_i-1)}\frac{1}{1+\delta^2}K_4 f_4 P_4, \tag{7.16}$$

where

$$B = \sqrt{\frac{5}{(2J_i+3)(2J_i-1)}},$$

$$C = \frac{(2J_i+5)(2J_i-3)}{(2J_i+3)(2J_i-1)},$$

$K_2 = J_i/(J_i+1)$, and $K_4 = J_i^3/(J_i+1)$.

As shown in Table 6.1, all transitions of interest in ^{209}At have $J_i = 7/2$. The intensity of the 745 and 337 keV lines is almost entirely accounted for by direct feeding from the ^{209}Rn electron capture decay, so we use only that transition in calculating the a_i's for those gamma rays. The 408 keV level is fed by a mixture of the 337 keV transition, higher-energy ^{209}At levels, and direct electron-capture from ^{209}Rn. Each transition between levels mixes the populations, so the population of the 408 keV level is approximated as a sum of three parts: direct population from ^{209}Rn ($5/2 \rightarrow 7/2$), indirect population through the 337 keV transition ($5/2 \rightarrow 7/2 \rightarrow 7/2$), and unaligned parent states from all other feeding mechanisms. We construct theoretical anisotropy parameters of the form

$$R_{theory} = \frac{W(\theta = 0^\circ)}{W(\theta = 90^\circ)} \tag{7.17}$$

for each gamma-ray, corresponding to the method of analysis of the gamma-ray data discussed in section 7.4. The excited state structure of ^{223}Fr has not been extensively

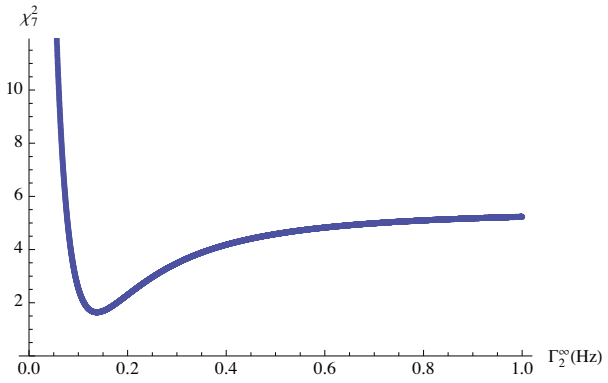

Figure 7.7: The reduced χ^2 curve for the fit to the uncoated-cell 337 keV data, with $\sigma_{\rm SE} = 2.5 \times 10^{-5}$Å^2 and $T_0 = 350$ K.

studied and the δ's are not well known, so one cannot at this time say with certainty what angular distribution function to use for each gamma ray line or what spin sequence determines the values of the a_i's for that isotope.

7.4 Polarization and Relaxation Results

As defined in section 7.3, the theoretical anisotropy values depend on three unknown polarization and relaxation parameters (in addition to the cell temperature and rubidium polarization values). These are the quadrupole relaxation parameter Γ_2^∞, the wall-binding energy parameter T_0, and the spin-exchange cross section $\sigma_{\rm SE}$. In cases where the multipole mixing ratio, δ, of a gamma-ray transition is unknown, we must treat that as an additional variable parameter. We developed a procedure to study the dependence of our measured anisotropy values on these parameters.

7.4.1 337 keV Anisotropy Fitting Procedure

The 337 keV gamma ray is known to be the result of a pure dipole transition [Shi96], and our anisotropy data for this line is consistent with the value of δ for such a transition (*i.e.*, $\delta = \infty$). In the case of the 745 keV line, Ref. [Shi96] shows that only an upper limit on δ for that transition has been determined thus far,

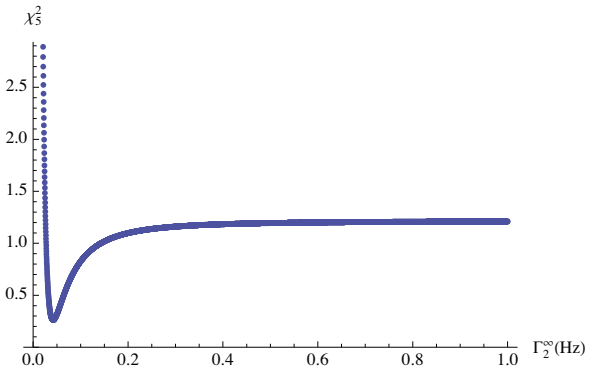

Figure 7.8: The reduced χ^2 curve for the fit to the coated-cell 337 keV data, with $\sigma_{\rm SE} = 2.5{\times}10^{-5}$Å^2 and $T_0 = 350$ K.

so when analyzing that data we must allow δ to remain a variable parameter in the theoretical anisotropy function. For the 408 keV line, on the other hand, Ref. [Shi96] lists the transition as pure electric quadrupole, which would result in an anisotropy for polarized ^{209}Rn. This contradicts our anisotropy observations (see Fig. 7.4) and those of Ref. [Kit88], in which no anisotropy signal for this line was observed, and so we retain δ as a variable parameter in our analysis of our 408 keV data as well. Our overall strategy is then to use the 337 keV data to obtain values for the spin-exchange and relaxation parameters, and use these values as inputs in fits to δ for the 408 and 745 keV data.

As mentioned in section 7.3, the anisotropy expression R_{theory} depends on the rubidium polarization, $\bar{P}_{\rm Rb}$, as well as the polarization and relaxation parameters $\sigma_{\rm SE}$, T_0, and Γ_2^∞. We measured the rubidium polarization in the optical pumping cells under the conditions they experienced at Stony Brook (see Chapter V). We insert the eight uncoated-cell rubidium polarization values and six coated-cell values obtained in this way into the R_{theory} expression (Eq. 7.17) for the 337 keV line. This results in a conversion of the R_{theory} expression from a continuous form to a discrete form with points at cell temperatures corresponding to those in the anisotropy measurements

Table 7.1: The reduced χ^2 for the best-fit value of Γ_2^∞ from the 337 keV uncoated-cell data for all of the values of T_0 (rows, K) and $\sigma_{\rm SE}$ (columns, Å^2) investigated.

	1.0×10^{-4}	7.5×10^{-5}	5.0×10^{-5}	2.5×10^{-5}	1.0×10^{-5}	7.5×10^{-6}	5.0×10^{-6}
100	1.60735	1.60735	1.60735	1.60735	1.60735	1.60736	1.60735
150	1.61422	1.61422	1.61422	1.61422	1.61423	1.61423	1.61423
200	1.62106	1.62106	1.62106	1.62106	1.62107	1.62106	1.62107
250	1.62787	1.62787	1.62787	1.62787	1.62787	1.62787	1.62789
300	1.63464	1.63464	1.63464	1.63464	1.63465	1.63467	1.63467
350	1.64138	1.64138	1.64139	1.64139	1.64139	1.64140	1.64146
400	1.64810	1.64810	1.64810	1.64810	1.64811	1.64811	1.64811
450	1.65477	1.65477	1.65477	1.65477	1.65479	1.65479	1.65479
500	1.66142	1.66142	1.66142	1.66143	1.66145	1.66142	1.66148
550	1.66803	1.66803	1.66803	1.66804	1.66803	1.66805	1.66821
600	1.67461	1.67461	1.67461	1.67461	1.67463	1.67462	1.67476
650	1.68116	1.68116	1.68116	1.68116	1.68117	1.68117	1.68135
700	1.68768	1.68768	1.68768	1.68768	1.68770	1.68768	1.68788
750	1.69416	1.69416	1.69416	1.69416	1.69420	1.69421	1.69420

(with the exception of the point at 201.75°C, which was not used in the fits). Each point in the R_{theory} set had error bars calculated by propagating the uncertainties in the rubidium polarization measurements through Eq. 7.17. The fitting method used to compare the value of R_{theory} to R_{expt} (the experimental ratio defined in Eq. 7.1) for the 337 keV line involves the calculation of the χ^2 for the difference between them for a range of possible values of the free parameters of R_{theory}.

We performed a grid search over a reasonable range of the three unknown R_{theory} parameters. Since the radon polarization coherence lifetime, which influences the precision of an EDM measurement performed using NMR techniques (see section 8.1), is related most directly to the value of Γ_2^∞, we focused our attention on that parameter. For every combination of the set of values for T_0 and $\sigma_{\rm SE}$ listed in Tables 7.1 and 7.2, we calculated R_{theory} for values of Γ_2^∞ from 0.0002 to 1.0000 Hz in increments of 0.0002 Hz. For each of these 5000 values of Γ_2^∞, we calculated the numerical value of R_{theory} and the corresponding error (as described above) at the temperatures for which we had measured R_{expt} values. Denoting these model and

Table 7.2: The reduced χ^2 for the best-fit value of Γ_2^∞ from the 337 keV coated-cell data for all of the values of T_0 (rows, K) and $\sigma_{\rm SE}$ (columns, Å^2) investigated.

	1.0×10^{-4}	7.5×10^{-5}	5.0×10^{-5}	2.5×10^{-5}	1.0×10^{-5}	7.5×10^{-6}	5.0×10^{-6}
100	0.25697	0.25697	0.25697	0.25697	0.25698	0.25698	0.25698
150	0.25799	0.25799	0.25799	0.25799	0.25799	0.25799	0.25799
200	0.25902	0.25902	0.25902	0.25903	0.25903	0.25906	0.25903
250	0.26007	0.26007	0.26007	0.26007	0.26008	0.26010	0.26008
300	0.26112	0.26112	0.26112	0.26113	0.26117	0.26113	0.26121
350	0.26219	0.26219	0.26219	0.26220	0.26225	0.26231	0.26231
400	0.26327	0.26327	0.26327	0.26327	0.26331	0.26331	0.26331
450	0.26436	0.26436	0.26437	0.26437	0.26441	0.26441	0.26441
500	0.26547	0.26547	0.26547	0.26548	0.26559	0.26567	0.26567
550	0.26658	0.26658	0.26658	0.26661	0.26661	0.26676	0.26661
600	0.26771	0.26771	0.26771	0.26771	0.26793	0.26793	0.26793
650	0.26884	0.26884	0.26884	0.26887	0.26900	0.26932	0.26932
700	0.26999	0.26999	0.26999	0.26999	0.27005	0.27001	0.27099
750	0.27115	0.27115	0.27116	0.27116	0.27130	0.27115	0.27213

experimental errors as $R_{theory}E$ and $R_{expt}E$, respectively, the difference between the theoretical and experimental R-values, ΔR, is

$$\Delta R = (R_{theory} - R_{expt}) \pm \sqrt{R_{theory}E^2 + R_{expt}E^2}. \tag{7.18}$$

We can then define a χ^2 for this fit as

$$\chi^2 = \sum \frac{\Delta R}{\sqrt{R_{theory}E^2 + R_{expt}E^2}}, \tag{7.19}$$

where the sum is taken over the experimental points in the fit. Figs. 7.7 and 7.8 show one of the discretized χ^2-curves obtained in this manner for the uncoated- and coated-cell 337 keV data, respectively. The best-fit value is the value of Γ_2^∞ at the minimum of the χ^2 function. The error in a fit for some parameter x is given by

$$\sigma_x^2 = 2\left(\frac{\partial^2\chi^2}{\partial x^2}\right)^{-1}_{x_0}, \tag{7.20}$$

where the second derivative of the discrete χ^2 function at the value of x at the minimum of the χ^2 function (x_0) can be estimated using the equation

$$\frac{\partial^2\chi^2}{\partial x^2}(x_0) \simeq \frac{\chi^2(x_0 - \delta x) + \chi^2(x_0 + \delta x) - 2\chi^2(x_0)}{\delta x^2}, \tag{7.21}$$

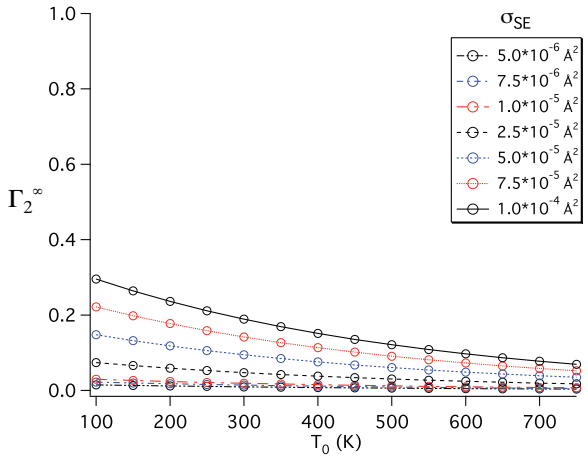

Figure 7.9: The value of Γ_2^∞ that minimizes χ^2 as a function of T_0 for various values of $\sigma_{\rm SE}$ in OTS-coated cells.

where δ_x is the step size in the discrete χ^2 function. We use this method to calculate the uncertainty in our best-fit value for Γ_2^∞.

7.4.2 337 keV Anisotropy Fit Results

The results for the 337 keV coated- and uncoated-cell data are shown in Figs. 7.9 and 7.10, respectively. As one can see by inspection of Tables 7.1 and 7.2, the minima of the χ^2 generated by each calculation had nearly the same magnitude for all of these fits. This made it impossible to determine a single best-fit value for any one of the parameters individually (i.e., as $\sigma_{\rm SE}$ is changed a corresponding change in Γ_2^∞ produces a similar temperature dependence of the R_{theory}). As a comparison of Figs. 7.9 and 7.10 makes clear, however, the radon polarization measurements presented in this work indicate slower relaxation rates (smaller Γ_2^∞) in OTS-coated cells. This provides motivation for further studies of the relaxation times of atoms sensitive to quadrupole wall interactions in coated and uncoated cells.

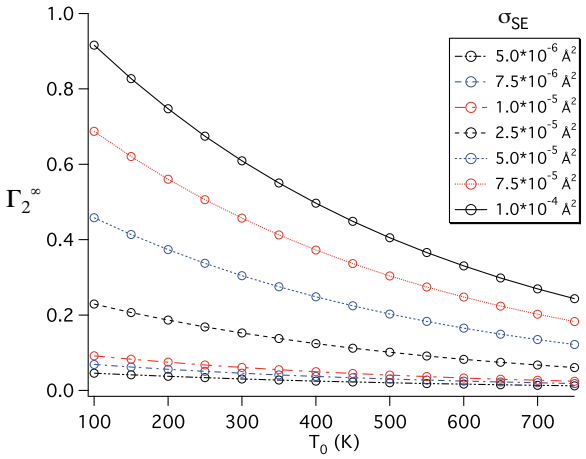

Figure 7.10: The value of Γ_2^∞ that minimizes χ^2 as a function of T_0 for various values of $\sigma_{\rm SE}$ in the uncoated cells.

7.4.3 408 and 745 keV Mixing Ratios

An extension of the polarization measurements discussed above would be to use the measured gamma-ray anisotropies to determine the multipole mixing ratio δ for the observed gamma-ray transitions. Since the angular distribution of the gamma rays from the four main lines in ^{209}Rn have known dependence on δ (see Eqs. 7.11 and 7.16), it should be possible to determine the values of Γ_2^∞ and T_0 from the 337 keV gamma ray, then use those values in the fits of the data for lines where the value of δ is unknown.

In order to analyze the 408 and 745 keV data, we used the Γ_2^∞ best-fit values and errors from the analysis of the 337 keV data for fits to δ, with the fitting procedure structured analagously to that used for the 337 keV fits. These fits included the contribution of the errors in the 337 keV Γ_2^∞ best-fit values to the error in R_{theory} in addition to the contribution from the rubidium polarization measurements. For the uncoated-cell 745 keV data (see Fig. 7.2), we fit to δ, with a step size of 0.002, over the range [0,100]. Since the χ^2 curves are shaped such that no best-fit value for δ can

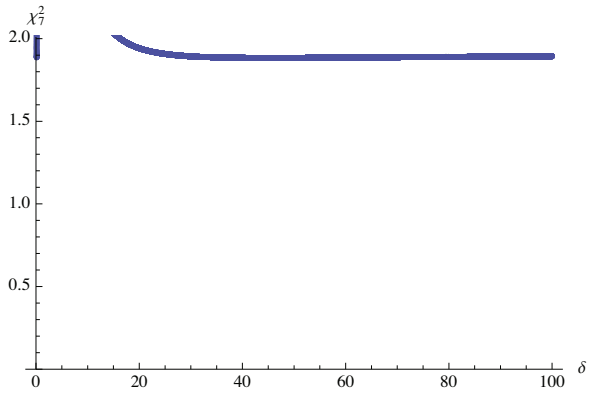

Figure 7.11: The reduced χ^2 curve for the fit to the uncoated-cell 745 keV data, with $\sigma_{\rm SE} = 2.5 \times 10^{-5}\text{Å}^2$, $\Gamma_2^\infty = 0.14 \pm 0.02$ Hz, and $T_0 = 350$ K. Only points with $\chi^2_7 < 2.010$ are shown.

be extracted, we instead structure the analysis in order to extract a limit on possible values of the mixing ratio. The plot in Fig. 7.11 shows the values of δ for one of the fits for which $\chi^2_7 < 2.010$, corresponding to a probability of 0.05 of exceeding that χ^2 value. Since the small-δ values allowed by our fits are already excluded by the limit given by the Table of Isotopes [Shi96], we conclude that our data allows $\delta > 15.5$ for the 745 keV gamma ray. As can be seen by inspection of Fig. 7.12, the fits to the coated-cell data resulted in a much weaker limit than that given by the uncoated-cell data.

The analysis of the 408 keV data (see Fig. 7.4) was performed similarly. The Table of Isotopes lists the 408 keV transition as pure E2, corresponding to $\delta = 0$. We fit the uncoated-cell 408 keV data to 1000 values of δ between 0 and 1. Figs. 7.13 and 7.14 show an example χ^2 curve for these fits, with Fig. 7.14 displaying only the region allowed by the criteria described above for the 745 keV limits. The best-fit value of δ for these fits was only very weakly dependent on the value of Γ_2^∞, so we can conclude that this data implies a mixing ratio of $\delta = 0.23 \pm 0.05$ for the 408 keV transition.

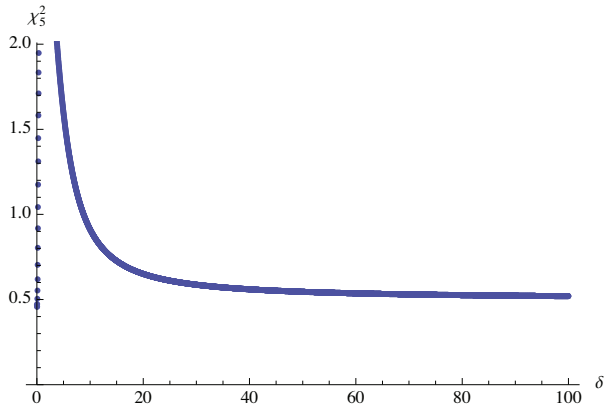

Figure 7.12: The reduced χ^2 curve for the fit to the coated-cell 745 keV data, with $\sigma_{\rm SE} = 2.5 \times 10^{-5}\text{Å}^2$, $\Gamma_2^\infty = 0.042 \pm 0.012$ Hz, and $T_0 = 350$ K. Only points with $\chi^2_7 < 2.010$ are shown.

For the coated-cell 408 keV data, the aberrant points (see Fig. 7.4 and discussion in section 7.2) affected the quality of the fits, as seen in the example χ^2 curves in Figs. 7.15 and 7.16. These fits were performed for 10,000 values of δ between 0 and 10. The minimum value of χ^2 was located at $\delta \simeq 4$, but was only slightly lower than the local minimum for $\delta < 2$ (for the fit shown in Figs. 7.15 and 7.16, these are $\chi^2_5 = 3.051$ and $\chi^2_5 = 3.055$, respectively). Given the large χ^2 and the indication from the Table of Isotopes than the value of δ should be small, we consider the local minimum to indicate the coated-cell 408 keV best-fit δ value and find $\delta = 0.35 \pm 0.07$. This value is within 2σ of the uncoated-cell-data result, indicating a weak agreement between the two data sets.

7.4.4 Effect of Finite Cell and Detector Sizes

The definition of R_{theory} given in Eq. 7.17 implicitly assumes that every gamma-ray detected by the $0°(90°)$ detector was emitted at a $0°(90°)$ angle with the direction of the parent atom's spin. Since they both have finite sizes, the gamma-rays detected actually came from a range of angles. The angular distribution functions (Eqs.

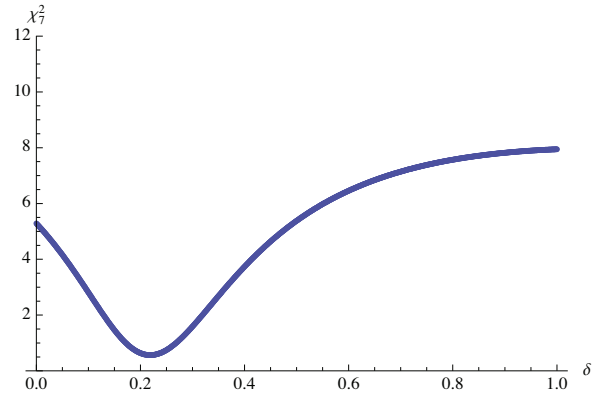

Figure 7.13: The reduced χ^2 curve for the fit to the uncoated-cell 408 keV data, with $\sigma_{\rm SE} = 2.5 \times 10^{-5}\text{Å}^2$, $\Gamma_2^\infty = 0.14 \pm 0.02$ Hz, and $T_0 = 350$ K.

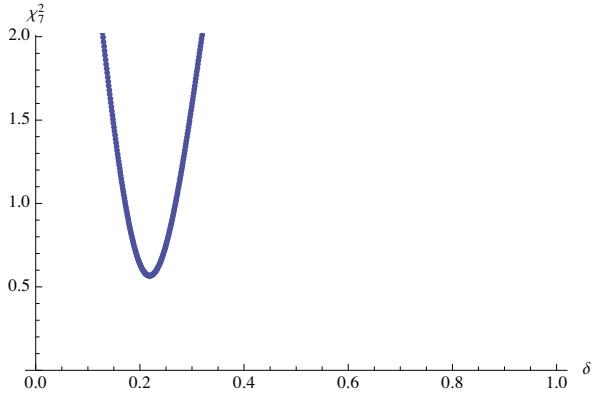

Figure 7.14: The reduced χ^2 curve for the fit to the uncoated-cell 408 keV data, with $\sigma_{\rm SE} = 2.5 \times 10^{-5}\text{Å}^2$, $\Gamma_2^\infty = 0.14 \pm 0.02$ Hz, and $T_0 = 350$ K. Only points with $\chi^2_7 < 2.010$ are shown.

7.11 and 7.16) have their extrema at 0 and 90°, so any gamma-ray detected from a slightly different angle would have a slightly smaller maximum possible R_{theory} value. Since Eqs. 7.11 and 7.16 can be written as linear functions of $\cos(2\theta)$ and $\cos(4\theta)$, the average gamma-ray intensity at the 0° detector is the value of the distribution function at the average values of $\cos(2\theta)$ and $\cos(4\theta)$ for the gamma-rays detected by that detector (similarly for the 90° detector). Thus,

$$R'_{theory} = \frac{W\left(\cos(2\theta) = \overline{\cos(2\theta_i)}, \cos(4\theta) = \overline{\cos(4\theta_i)}\right)_{0°\text{detector}}}{W\left(\cos(2\theta) = \overline{\cos(2\theta_i)}, \cos(4\theta) = \overline{\cos(4\theta_i)}\right)_{90°\text{detector}}}, \tag{7.22}$$

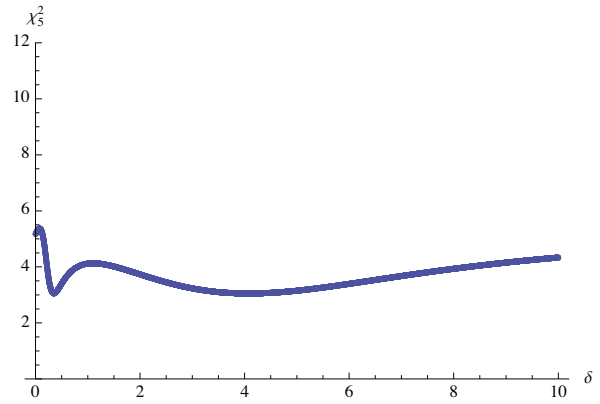

Figure 7.15: The reduced χ^2 curve for the fit to the coated-cell 408 keV data, with $\sigma_{\mathrm{SE}} = 2.5 \times 10^{-5}\text{Å}^2$, $\Gamma_2^{\infty} = 0.042 \pm 0.012$ Hz, and $T_0 = 350$ K.

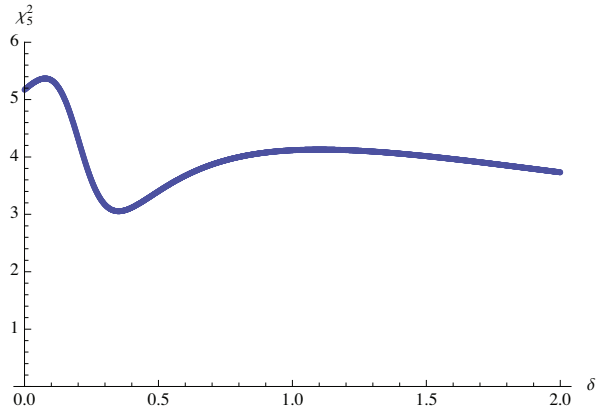

Figure 7.16: The reduced χ^2 curve for the fit to the coated-cell 408 keV data, zoomed in on the lower values of δ, with $\sigma_{\mathrm{SE}} = 2.5 \times 10^{-5}\text{Å}^2$, $\Gamma_2^{\infty} = 0.042 \pm 0.012$ Hz, and $T_0 = 350$ K.

where θ_i is the emission angle of an individual detected gamma ray.

As a simple way of determining an upper limit on how much our assumption affected our results, we used a Monte Carlo method to determine the cosine averages for detected gamma rays. We set the cell radius to 1 inch, and the front surfaces of the detectors were 1.875 inch radius circles 2 inches from the surface of the cell. We generated a uniform distribution of emitted gamma rays throughout the volume of the cell and kept track of the emission angle for (and total number of) the ones that hit a detector. Under the assumption that the detectors were infinitely efficient (*i.e.*,

every gamma ray that passed through the front surface of a detector was detected), the cosine averages for the detected gamma rays were $\overline{\cos(2\theta_i)} = 0.66$ and $\overline{\cos(4\theta_i)} = -0.02$ for the 0° detector, and $\overline{\cos(2\theta_i)} = -0.831$ and $\overline{\cos(4\theta_i)} = 0.449$ for the 90° detector. We ran the Monte Carlo multiple times to determine how many significant digits to use. For example, in two sets of 1×10^7 gamma rays generated, the 0° detector had $\overline{\cos(2\theta_i)} = 0.662$ and $\overline{\cos(2\theta_i)} = 0.661$.

Our fit of R'_{theory} to the 337 keV data, using the same procedure as discussed in subsection 7.4.1, resulted in slightly lower relaxation rates than did the original fit. For example, the result for $T_0 = 350$ K and $\sigma_{\rm SE} = 2.5 \times 10^{-5}\text{Å}^2$ in the uncoated-cell data was $\Gamma_2^\infty = 0.109 \pm 0.017$ Hz, while the corresponding value for R_{theory} was $\Gamma_2^\infty = 0.138 \pm 0.020$ Hz. For the coated-cell data, those T_0 and $\sigma_{\rm SE}$ values gave $\Gamma_2^\infty = 0.038 \pm 0.011$ Hz instead of $\Gamma_2^\infty = 0.042 \pm 0.012$ Hz. The R'_{theory} fits had slightly better reduced χ^2's, ranging from 1.55 to 1.64 instead of 1.61 to 1.69 as in the R_{theory} fits (see Table 7.1) for the uncoated-cell data. The reduced χ^2's for the coated-cell data ranged from 0.25 to 0.26 instead of 0.26 to 0.27 (see Table 7.2).

While the shift in Γ_2^∞ is, at most, about 1σ, the shift is towards smaller relaxation rates for all wall-binding energies and spin-exchange cross sections considered. Thus the neglect of the finite cell- and detector-sizes results in a small systematic shift in our relaxation results. As a percentage of the results from the original R_{theory} fits, these shifts amount to 20-21% for the uncoated-cell data and 17-18% for the coated-cell data. For comparison, the statistical uncertainties in the original Γ_2^∞ values were 14-15% and 30-31% for the uncoated- and coated-cell data, respectively. Since the simplified Monte Carlo above does not take into account the dependence of the gamma-ray detection probabilities on the length of their path through a germanium crystal, it only gives an upper limit on the systematic shift. Further, the direction

of the shift means that the prediction of the achievable EDM measurement precision in section 8.1 is conservative.

We also fit the 408 and 745 keV data to R'_{theory} in order to see how the finite size effect would change our multipole mixing ratio results. For the 745 keV data, there was a shift in the limit on δ similar to that in the best-fit values for Γ_2^∞ from the 337 keV data, but towards a slightly weaker limit. The uncoated-cell data gave a lower limit of $\delta > 14.8$ for the 745 keV transition, which is still much stronger than the $\delta > 2.86$ from the Table of Isotopes [Shi96]. The fits of the uncoated- and coated-cell 408 keV data to R'_{theory} were almost identical to the fits to R_{theory}. This is unsurprising, since there was no detected anisotropy in the 408 keV gamma-ray rates. The finite-size effect reduces the detected magnitude of an anisotropy, so the signal from an isotropic gamma-ray distribution is unaffected by the size of the detectors or cell. The fit of the uncoated-cell data to R'_{theory} gave $\delta = 0.22 \pm 0.03$, so the value from the fit to R_{theory} ($\delta = 0.23 \pm 0.05$) holds.

CHAPTER VIII

Conclusion

In this dissertation, I have discussed the development of techniques enabling a measurement of the CP-violating EDM of radon isotopes using gamma-ray anisotropies to measure the precession frequency. The search for new sources of CP violation is an essential component in explaining the observed matter-antimatter asymmetry in the universe. A permanent EDM in a quantum mechanical system would violate CP symmetry, and since the standard model (SM) background is so low, a nonzero EDM measurement would be a signal of beyond the standard model (BTSM) physics. As discussed in more detail in Chapter II, many hypothetical CP-odd interactions could exist, each with different contributions from the various models of CKM-mechanism-independent CP violation, including both BTSM sources and strong CP violation. Thus, EDM measurements in multiple systems will be required to determine the strength of each type of interaction and trace it back to a particular CP-violation model.

In the search for the first non-zero EDM measurement, certain atomic systems have built-in advantages. Octupole deformations and vibrations can enhance the collective effect of CP-odd nuclear interactions, leading to a greater sensitivity to CP violation in certain isotopes. The current best limit on an atomic EDM is for the

diamagnetic atom ^{199}Hg: $d_{\mathrm{Hg}} \leq 3.1 \times 10^{-29} e \cdot \mathrm{cm}$ [Gri09]. The noble gas ^{223}Rn has certain advantages that make it an attractive system for an EDM experiment. Earlier noble-gas EDM experiments [Ros01] demonstrated the advantages of noble gases for these studies due to the long polarization lifetimes achievable through spin-exchange optical pumping techniques.

The relatively straightforward nature of the NMR techniques used to measure a noble gas atomic EDM are complicated somewhat by the fact that ^{223}Rn is a radioactive isotope with a half-life of about 23 minutes. This precludes the production of large enough quantities of ^{223}Rn to obtain the NMR signal from the electromagnetic effect of the spins precessing coherently, so we have developed the technology and techniques necessary to use the radiation distribution to determine the precession frequency. We must be able to see a polarization signal by detecting an anisotropy in the emitted radiation, we must have a system with the ability to observe the change in the size of this signal in each detector as the atoms precess. Another complication arises from the nuclear spin of ^{223}Rn, an $I = 7/2$ isotope. With this spin, ^{223}Rn will experience quadrupole wall interactions which will limit our ability to polarize it and have that polarization remain coherent long enough to obtain accurate precession frequency measurements. The development work contained in this thesis moves the Radon EDM experiment closer to measuring the EDM of ^{223}Rn using anisotropies in gamma radiation.

8.1 Conclusions from the Development Work

As discussed in Chapter IV, we developed an apparatus that allows us to collect a sample of a noble gas in a thin zirconium foil and transfer the sample, with high efficiency, to a glass optical pumping cell. We successfully polarized ^{209}Rn in such cells

and studied the temperature dependence of the resulting gamma-ray anisotropies in measurements discussed in Chapters VI and VII. Coupled with rubidium polarization measurements discussed in Chapter V, we were able to use this anisotropy data to study the dependence of the anisotropy signal on a set of spin-exchange and relaxation parameters. These results indicate slower relaxation rates in OTS-coated cells for isotopes experiencing quadrupole relaxation.

As discussed in more detail in Chapters II and III, in atomic systems the EDM is proportional to the Schiff moment [Fla02], a function of the charge distribution of the nucleus. The Schiff moment is linearly proportional to the atomic number, so it would be expected that, aside from the technical difficulties involved in using radioactive atoms for an EDM measurement, the radon isotopes could provide an attractive candidate for a noble gas EDM experiment. In addition to that advantage, heavy nuclei can be subject to varying degrees of octupole deformation [Eng00], which enhances the Schiff moment. The isotopes ^{221}Rn and ^{223}Rn have spins suitable for the measurement of their polarization using their gamma-ray angular distributions and are expected to have large octupole deformations. Calculations indicate a sensitivity to fundamental EDMs for ^{223}Rn 400-600 times that of ^{199}Hg [Spe97], for which the current most-sensitive limit on an atomic EDM has been made. With $|d(^{199}\mathrm{Hg})| < 2.10 \times 10^{-28} e \cdot \mathrm{cm}$ [Rom01], the enhancement factor implies that a measurement of the ^{223}Rn EDM with a sensitivity between 8×10^{-26} and $1 \times 10^{-25} e \cdot \mathrm{cm}$ would have the same sensitivity to CP violation as the ^{199}Hg result. A recent improvement of the ^{199}Hg limit to $|d(^{199}\mathrm{Hg})| < 3.1 \times 10^{-29} e \cdot \mathrm{cm}$ [Gri09] moves the equal-sensitivity measurement level to about $1 \times 10^{-26} e \cdot \mathrm{cm}$.

If we use $T_0 = 350$ K and $\sigma_{SE} = 2.5 \times 10^{-5} \text{Å}^2$ (corresponding to the wall-binding energy of ^{131}Xe from Ref. [Wu90] and the Rb-^{209}Rn spin-exchange cross section from

Ref. [Wal89]), the best-fit values for Γ_2^∞ for the uncoated and coated cells become 0.14 ± 0.02 Hz and 0.04 ± 0.01 Hz, respectively. For a coated cell at 200°C, this implies a coherence time of $T_2 \simeq 12$ s. The precision of an atomic EDM measurement is given by the formula

$$\delta_d = \frac{\hbar}{2\mathrm{E}\,T_2}\sqrt{\frac{1}{A^2(1-B)^2N}}, \tag{8.1}$$

where E is the magnitude of the electric field across the measurement cell, A is the analyzing power for the method of detection (for the gamma-ray method described in this thesis, this is the maximum level of anisotropy achieved), N is the number of gamma rays detected, and B is the fraction of those due to background. Using the coherence time inferred from the coated cell data and setting $A = 0.1$, $B = 0.01$, and E= 10 kV/cm, collecting 10^{12} gamma rays will make possible an EDM sensitivity of $\delta_d \simeq 2.8 \times 10^{-26} e \cdot \mathrm{cm}$. Given the enhancement to fundamental EDM sensitivity in octupole-deformed nuclei like ^{223}Rn and the conservative estimate of T_2, this indicates that the gamma-ray anisotropy technique should have about the same sensitivity to CP violation as the new ^{199}Hg measurement. The second phase of the Radon EDM experiment, which would use the beta anisotropy, will allow significantly improved statistics and thus has the potential to have improved sensitivity to CP-violation compared to the current ^{199}Hg result.

In addition to studying the ^{209}Rn polarization and relaxation mechanisms, we were able to use the gamma-ray anisotropy data to measure improved limits on multipole mixing ratios of some of the main ^{209}Rn gamma-ray lines. We used a conservative model of the cell and detector geometry to find mixing-ratio limits of $\delta > 14.8$ for the 745 keV transition and $\delta = 0.23 \pm 0.05$ for the 408 keV transition, as compared to the Table of Isotopes [Shi96] values of $\delta > 2.86$ and $\delta = 0$, respectively.

8.2 Future Work

While we have made significant progress towards measuring the ^{223}Rn EDM, there is still much work left to be done. We need to develop the shielded magnetic field that will be able to generate the small, very uniform magnetic fields required for the slow precession rates and long coherence times necessary to measure the NMR signal using gamma-ray anisotropies. We need to further study the temperature dependence of the polarization signal from isotopes with quadrupole moments (*e.g.*, ^{131}Xe) in order to determine the optimum cell temperature for ^{223}Rn EDM measurements. We also need to determine what species to use as a comagnetometer. One possibility is ^{211}Rn, which could be produced, stored, and periodically replenished without any major alterations to the experimental apparatus.

As mentioned in Chapter III, the second phase of the Radon EDM experiment will use anisotropies in the beta emission from ^{223}Rn decay to extract a precession frequency. This will require specially designed measurement cells that feature thin windows to minimize the beta attenuation while still maintaining structural stability. We are considering the possibility of incorporating silicon detectors into the cells themselves. The development work for these cells is ongoing.

Finally, if we are able to develop a deep UV laser and generate enough ^{223}Rn to produce optically thick samples in the measurement cells, we could could eliminate the spin-exchange aspect of the polarization process and drive the transitions in ^{223}Rn directly. This would produce a much higher ^{223}Rn polarization than is possible with the rubidium spin-exchange method, resulting in larger anisotropy signals. In turn, these larger signals would allow for a more precise EDM measurement. The absence of rubidium from the cells might make it possible to use sulfur hexafluoride as the

optical pumping buffer gas, allowing us to use even larger electric fields.

APPENDIX

APPENDIX A

Xe Polarization Measurements

A.1 Introduction

As we have seen, quadrupole interactions dominate the relaxation of a noble gas when present. A narrow-band laser should be able to maximize the rubidium polarization in an optical pumping cell, eliminating one of the limiting factors in the radon polarizations achieved at Stony Brook. Natural xenon is an excellent medium for this investigation. Since these xenon isotopes are stable, repeated adiabatic fast passage (AFP) NMR measurements can be done to optimize the polarization signal. Also, the cells would contain species experiencing both quadrupole and dipole relaxation (^{131}Xe, $I = 3/2$) and only dipole relaxation (^{129}Xe, $I = 1/2$). A comparison of their respective polarization signals would isolate the effect of quadrupole relaxation on the maximum achievable polarization for a noble gas.

A.2 Narrow-Band Diode Laser

We constructed an external cavity narrowed diode laser of the type developed by Babcock [Bab05]. The diode laser was a 100 W n-Light CASCADES C1-795-100 [nLi], cooled with deionized water pumped by an OptiTemp water chiller [Opt]. Fast-axis collimation was achieved using a lens installed by the manufacturer. As

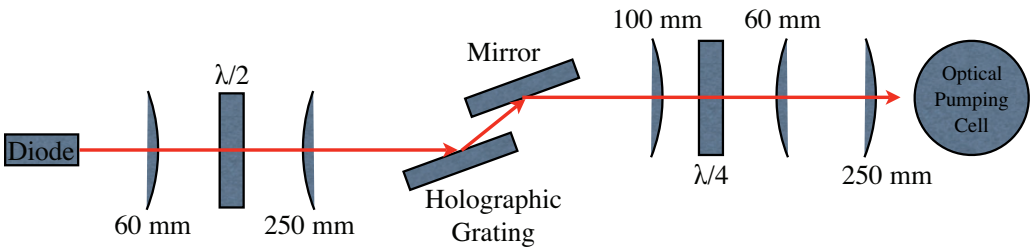

Figure A.1: A diagram of the optical components of the external cavity narrowed diode laser. The first set of lenses expand the beam to cover as much of the grating as possible, and the second set of lenses allow the beam to be shaped to illuminate the entirety of the cell.

illustrated in Fig. A.1, the external cavity consisted of a 60mm lens (Thorlabs LA1401-B [Tho]), a $\lambda/2$ plate (CVI QWP0-795-10-2-R15 [CVI]), a 250 mm lens (Thorlabs LA1301-B [Tho]), and a holographic grating (Edmund Optics NT43-223 [Edm]). The two lenses act as a telescope to adjust the size of the output beam to the size of the grating. The grating is mounted with all three rotation angles adjustable. This allows us to adjust its position so that the first-order reflection illuminates the diode emitters (driving them all at a single frequency) and adjust the tilt and yaw to optimize the feedback for narrowest bandwidth. We mount a mirror (Thorlabs BB2-E03 [Tho]) parallel to the grating so that the output beam travels in the same direction regardless of any adjustments in the tuning of the laser frequency. A second set of lenses, consisting of another 60 mm/250 mm lens pair and a 100 mm cylindrical lens (CVI 01 LCP 011/076 [CVI]), allows us to shape the output beam to illuminate the entire optical pumping cell, and a $\lambda/4$ plate (CVI QWP0-795-10-4-R15 [CVI]) circularly polarizes the output light.

The power output of the diode laser increases linearly with the driving current, provided by a Lambda ZUP6-132 [TDK] power supply. The power measurements shown in Fig. A.2 illustrate this trend and demonstrate that the narrowed laser outputs about 80% as much power as the un-narrowed laser at the same diode current.

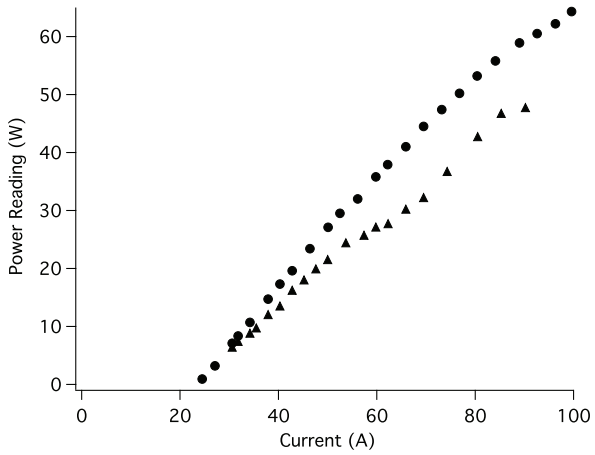

Figure A.2: Measurements of the laser power output dependence on the current applied to the diode with (triangles) and without (circles) using the external cavity to narrow the frequency spectrum.

Fig. A.3 shows the linewidths we were able to achieve at various diode currents. As the current increases, the diode temperature increases as well, causing the center of the un-narrowed spectrum to shift towards larger wavelengths. We readjust the position of the grating to optimize the narrowed output at each diode current. Above 75 A diode current, these adjustments become less and less effective and the laser runs at two or more modes simultaneously, resulting in wider laser profiles.

A.3 Xe AFP Measurements

We performed a series of AFP measurements using natural xenon in uncoated and coated cells to see if the temperature dependence of the ^{131}Xe polarization behaves similarly to what we observed in our ^{209}Rn measurements. The ^{209}Rn polarization signal was most noticeable at the highest temperatures investigated, and the fits to Γ_2^∞ indicated longer polarization lifetimes for coated cells (see Chapter VII). A comparison of the size of the AFP signal for ^{129}Xe to that of ^{131}Xe should indicate similar trends.

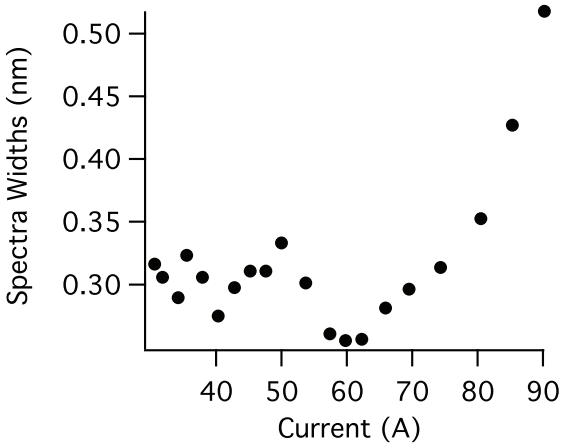

Figure A.3: The linewidth of the narrowed laser achieved at various diode currents.

A.3.1 Experimental Setup

Fig. A.4 shows the AFP measurement apparatus. We illuminate the cells with circularly polarized light from the narrow band laser, with a diode current of 100.8 A, tuned to the Rb D1 line (795 nm). This polarizes the xenon through spin-exchange collisions (see Chapter III). We generate an RF field of 10.5 kHz over the cell using a signal generated by one of the function generators (SRS DS345 [Sta]) and amplified by an RF amplifier (Crown D-75A [Cro]). We chose this RF frequency so that the magnet power supply (Kepco BOP 50-8M [Kep]) would be able to reach the resonances of both odd-A xenon isotopes. In a 10.5 kHz RF field, the ^{129}Xe resonance is located at a magnetic field of $B_z = 8.85$ Gauss and the ^{131}Xe resonance is at $B_z = 29.87$ Gauss. If we sweep B_z (generated by the Helmholtz coils) through the xenon NMR resonance slowly enough that the spins are able to follow the field but quickly enough that the spins maintain their coherence while passing through the resonance, the rotating spins will drive a small current in the pickup coils. These coils were designed such that their peak Q-value is near the ^{129}Xe resonance frequency.

The signal from the pickup coils passes through a pre-amp (SRS SR560 [Sta]), and

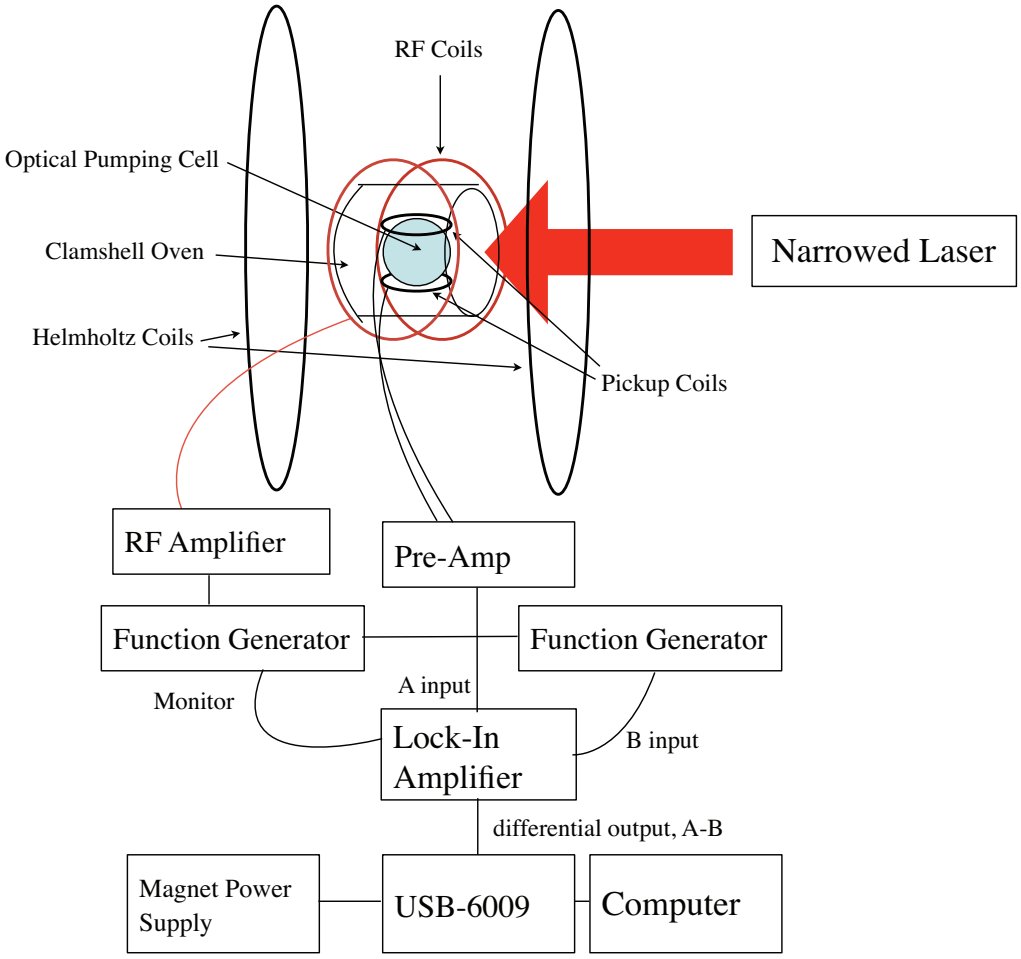

Figure A.4: The AFP measurement apparatus. The Helmholtz, RF, and pickup coils are all perpendicular to each other. For details of the narrowed laser, see Fig. A.1

the pre-amp output is connected to one of the inputs of the lock-in amplifier (SRS SR530 [Sta]), which is locked to the RF frequency. The second function generator is frequency-locked to the first function generator, and its output is connected to the other lock-in input. Since the RF and pickup coils are not perfectly perpendicular to each other, some of the RF signal will always be picked up by the pickup coils. We use the second function generator to cancel this part of the signal in the lock-in, sending the differential output from the lock-in to the data acquisition device (NI USB-DAQ 6009 [Nat]) controlled by a computer.

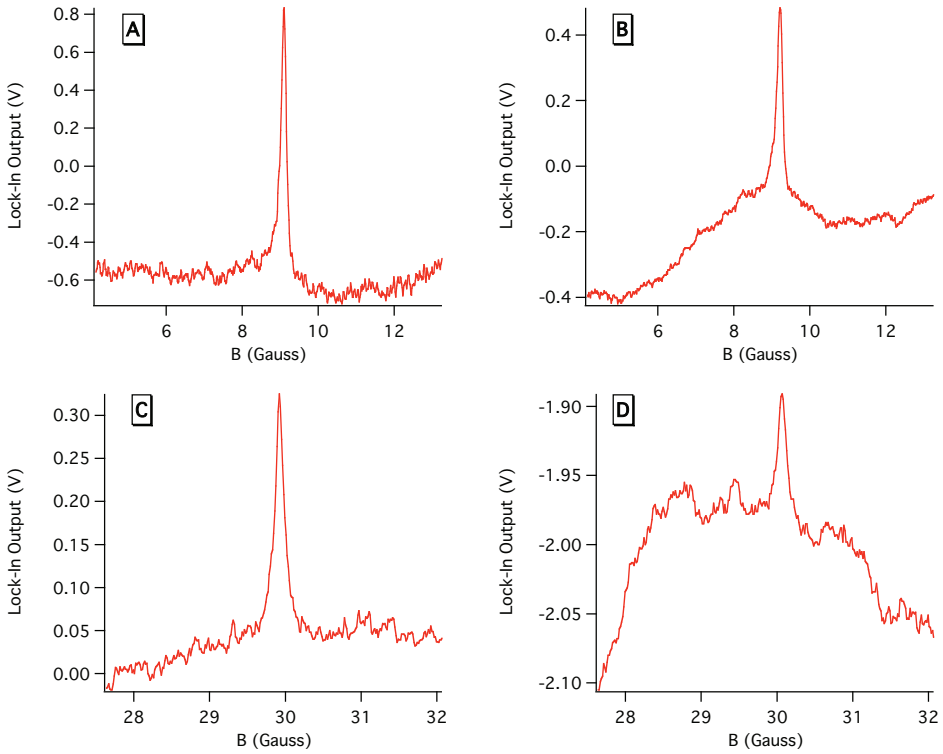

Figure A.5: **A**: A ^{129}Xe AFP signal in the uncoated cell at 150°C with a 20 sec delay before beginning the sweep. **B**: A ^{129}Xe AFP signal in the coated cell at 140°C. This is the average of 10 sweeps with a pre-sweep delay of 60 sec. **C**: A ^{131}Xe AFP signal in the uncoated cell at 170°C. This is the average of 10 sweeps with an inter-sweep delay of 60 sec. **D**: A ^{131}Xe AFP signal in the coated cell at 150°C. This is the average of 25 sweeps with an inter-sweep delay of 30 sec. The background variations arise due to drifts in the lock-in output signal that do not average out over the course of the set of AFP sweeps.

A.3.2 Data and Analysis

We wished to compare the relative magnitude of the ^{129}Xe and ^{131}Xe polarization signals in coated and uncoated cells, with special attention paid to the cell temperatures used in the Stony Brook ^{209}Rn measurements. The xenon polarization builds up with a time constant T_1, so for each cell type and temperature investigated we performed an AFP sweep after allowing the polarization to build for various lengths of time. For the ^{129}Xe data, we moved the magnetic field to the resonance for 15 sec, enough time for the RF to destroy the polarization. We then moved the mag-

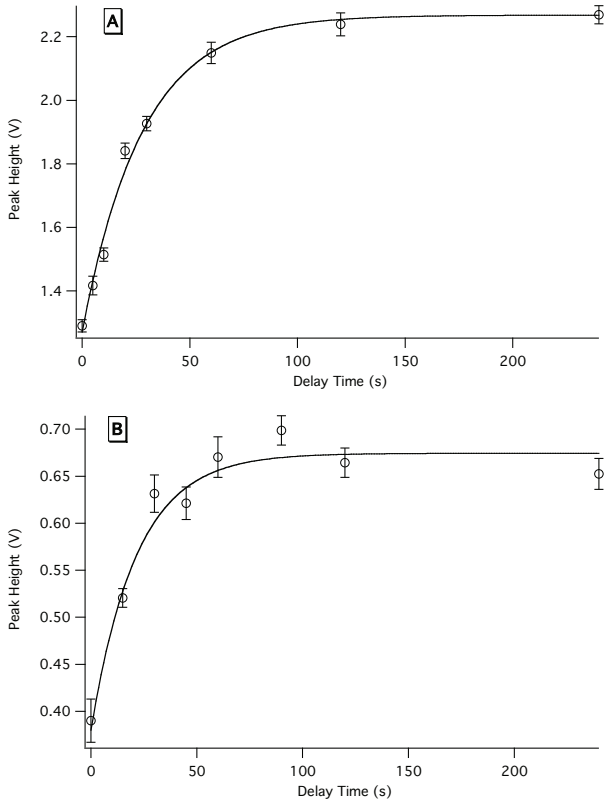

Figure A.6: **A**: The ^{129}Xe AFP peak heights as a function of the pre-sweep delay time in the uncoated cell at 140°C. The solid line is the exponential fit described in the text. **B**: The ^{129}Xe AFP peak heights as a function of the pre-sweep delay time in the coated cell at 140°C.

netic field away from the resonance and waited a set time before performing an AFP sweep. Fig. A.5 plots **A** and **B** show examples of the ^{129}Xe AFP data for uncoated and coated cells, respectively. The coated cell contained less xenon than did the uncoated cell, so the ^{129}Xe signal in the coated cell was weak enough that it was necessary perform the above procedure multiple times and average the results.

The ^{131}Xe was always small enough compared to the level of background noise that an average of multiple sweeps was necessary. For these, we set the magnetic field to just below the resonance, waited for a set time, swept through the resonance, and returned to the starting point. We averaged all but the first sweep in a set so

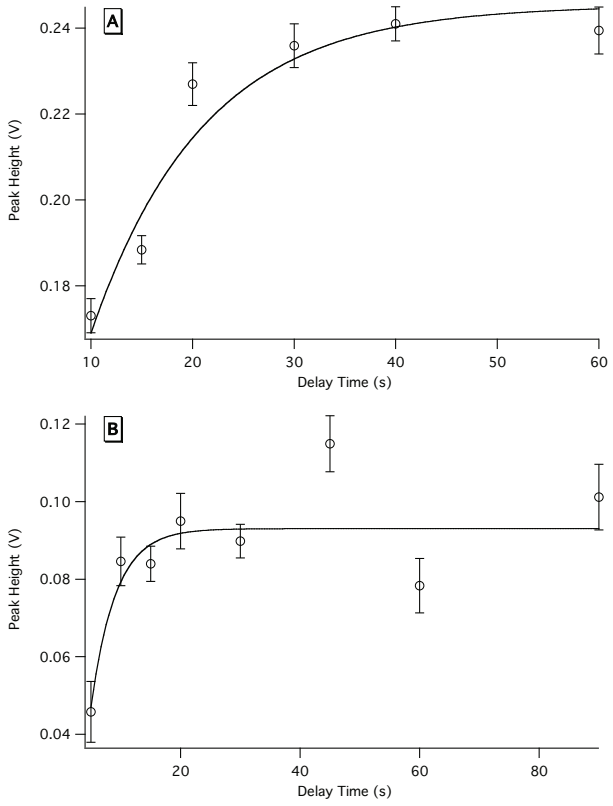

Figure A.7: **A**: The ^{131}Xe AFP peak heights as a function of the inter-sweep delay time in the uncoated cell at 140°C. The solid line is the exponential fit described in the text. **B**: The ^{131}Xe AFP peak heights as a function of the inter-sweep delay time in the coated cell at 140°C.

that every sweep should have begun with the same level of ^{131}Xe polarization. Fig. A.5 plots **C** and **D** show examples of the ^{131}Xe AFP data for uncoated and coated cells, respectively. We swept the magnetic field at the same rate in the ^{129}Xe and ^{131}Xe measurements.

Following the derivation in Ref. [Wag91], if we write the magnetic field from the Helmholtz (z-direction) and RF coils (x-direction) in the laboratory frame as

$$\mathbf{B}_{lab} = B_x \cos(2\pi\nu)\hat{\mathrm{x}} + B_z\hat{\mathrm{z}}, \tag{A.1}$$

then the equation of motion for a magnetization $\mathbf{M}$ in a frame rotating around $\hat{\mathrm{z}}$ at

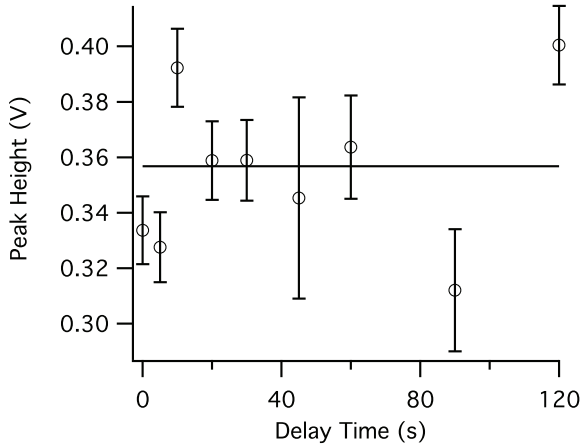

Figure A.8: The ^{129}Xe AFP peak heights as a function of delay time in the coated cell at 160°C. The solid line is the weighted average of the points.

the RF frequency ν is given by

$$\frac{d\mathbf{M}}{dt} = \gamma \mathbf{M} \times (\mathbf{B} + (\nu/\gamma)\hat{\mathrm{z}}). \tag{A.2}$$

Here γ is the gyromagnetic ratio. Thus, we can approach the magnetization as being in an effective static magnetic field

$$\mathbf{B}_{eff} = B_x \hat{\mathrm{x}} + (B_z + \nu/\gamma)\hat{\mathrm{z}}. \tag{A.3}$$

The AFP signal S will be proportional to the projection of the precessing magnetization onto the x-axis. The magnetization will make an angle θ with the z-axis such that $\tan\theta = B_x/(B_z + \nu/\gamma)$, and since $S \propto M \sin\theta$,

$$S \propto M \frac{B_x}{\sqrt{(B_z + \nu/\gamma)^2 + B_x^2}}. \tag{A.4}$$

Given this form for the AFP signal, we fit each AFP sweep to a function consisting of the square root of a Lorentzian function on a linear background. The statistical fluctuation of a 100-point region of the background determined the uncertainty in each point of an AFP signal. We used the peak height from each fit as our measure of the polarization signal in the cell type and temperature under investigation.

After collecting a set of AFP signals over a range of polarization-building delay times for a particular cell, temperature, and isotope, we fit the data to the function

$$y(t) = y_0 + A \exp^{-(t-t_0)/\tau} . \tag{A.5}$$

We extract from this the magnitude of the peak height with an infinite delay time, y_0, and the time constant for the polarization build-up, τ. Fig. A.6 plots **A** and **B** show examples of the build-up of the ^{129}Xe AFP signal in the uncoated and coated cells, respectively, and Fig. A.7 plots **A** and **B** show the same for the ^{131}Xe AFP signal. Due to the combined effects of the smaller overall strength of the AFP signals measured in the coated cell and the shortening of the ^{129}Xe polarization time constant as the cell temperature increases, at 160°C and above we were unable to measure the ^{129}Xe time constant. Fig. A.8 shows the data obtained in the coated cell at 160°C with multiple delay times, displaying no evidence of an exponential build-up. So, we obtained the ^{129}Xe AFP signals in the coated cell at 170 and 180°C by averaging 20-25 sweeps all with the same delay time (30 sec) and considered the result to be the $t = \infty$ signal.

We were able to obtain peak-height and time-constant data for ^{129}Xe and ^{131}Xe in coated and uncoated cells at most of the temperatures used in the ^{209}Rn measurements. Figs. A.9 and A.10 show the peak-height results in the coated and uncoated cells, respectively, and Figs. A.11 and A.12 show the coated- and uncoated-cell time-constant results, respectively. During the process of generating these results, after each fit the uncertainties in the fit parameters were multiplied by the square root of the reduced χ^2. This was intended to correct for any possible errors in the weighting of the points in the AFP signals due to non-linearities in the background.

The ^{129}Xe data display the expected qualitative temperature dependence of a system experiencing only dipole relaxation mechanisms, as both the measure of the

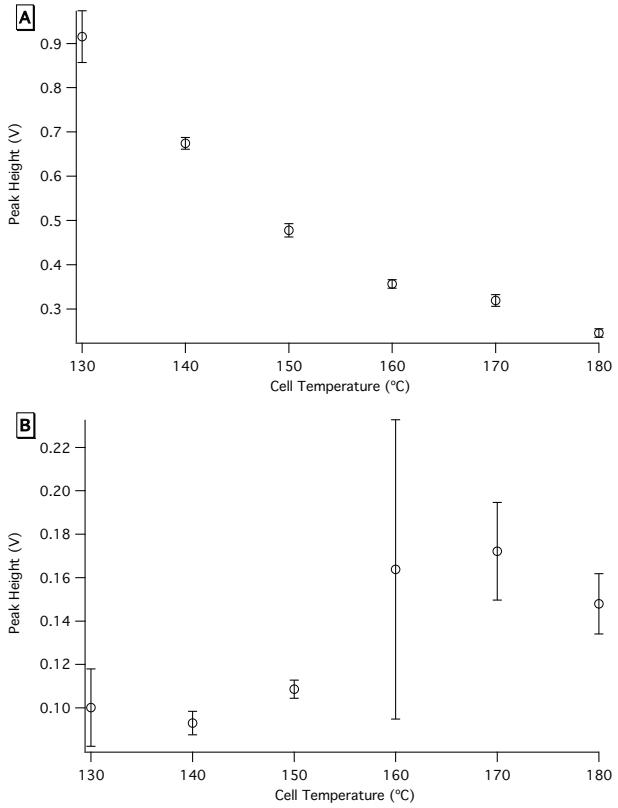

Figure A.9: The coated-cell ^{129}Xe (**A**) and ^{131}Xe (**B**) AFP peak heights at $t = \infty$ as a function of cell temperature. For some of the points, the combination of small signal size and large background drifts resulted in very large error bars after the χ^2 error correction (see text).

overall polarization achievable (the peak height) and the polarization time constant decrease exponentially with increasing temperature. As can be seen in Fig. A.12, the uncoated-cell ^{129}Xe polarization time constant appears to decay to a value of about 10 sec rather than zero. Further investigation would be required to determine whether this is a systematic effect or a result of real features of the relaxation mechanisms. While we obtained uncoated-cell ^{209}Rn polarization data at temperatures up to 220°C, the presence of the pickup coils inside the oven in the AFP measurements prevented us from performing these studies at temperatures above 200°C. The solder used to connect the leads to the pickup coils has a listed melting point of 179°C,

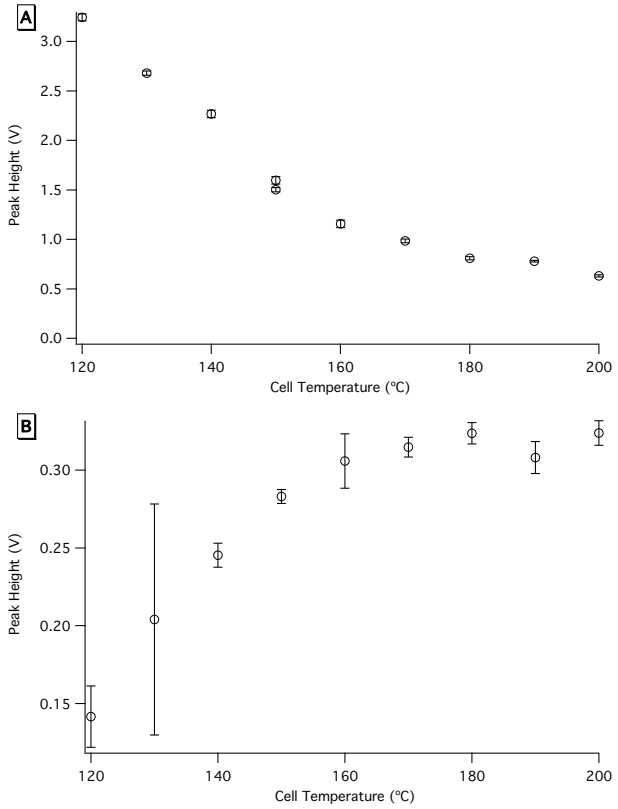

Figure A.10: The uncoated-cell ^{129}Xe (**A**) and ^{131}Xe (**B**) AFP peak heights at $t = \infty$ as a function of cell temperature.

so that would have to be replaced with a high-temperature solder to allow AFP measurements beyond those we obtained.

If quadrupole wall interactions have the Arrhenius temperature dependence [Hap72] used in the analysis of the ^{209}Rn data (see Eq. 7.10), we would expect the quadrupole relaxation rate to decrease with increasing temperature. The rubidium polarization, which limits the maximum achievable xenon polarization, will begin to decrease above some temperature as well (see Chapter V). So, we would expect the decreasing quadrupole relaxation rate to cause the total polarization signal to increase with increasing temperature until we reach a turn-over point (a temperature at which the decreasing rubidium polarization overcomes this effect). Our ^{131}Xe polarization data

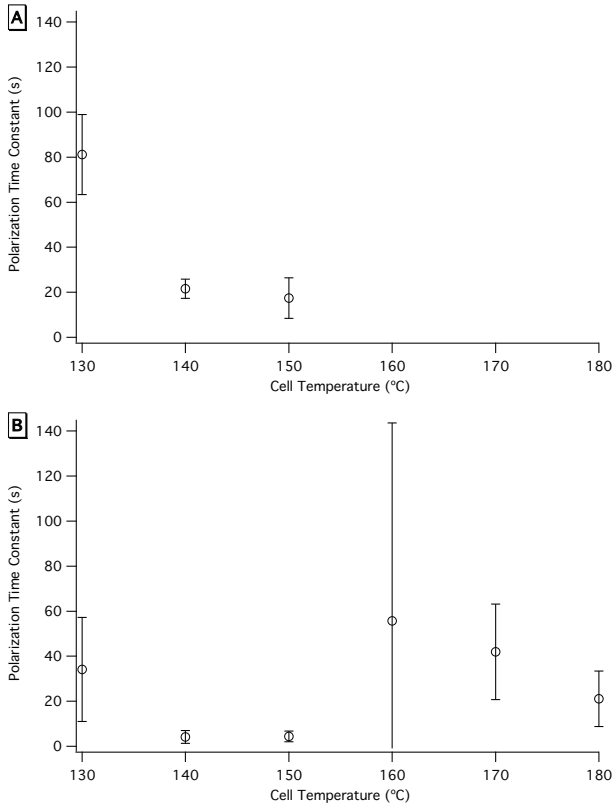

Figure A.11: The coated-cell ^{129}Xe (**A**) and ^{131}Xe (**B**) polarization time constants as a function of cell temperature. As discussed in the text, we were unable to measure the build-up of the ^{129}Xe signal above 150°C. For some of the points, the combination of small signal size and large background drifts resulted in very large error bars after the χ^2 error correction (see text).

(see Figs. A.9 and A.10) follow this pattern. The ^{131}Xe data does not turn over in the temperature range investigated, corroborating our observations in the ^{209}Rn system. The uncertainties in some of the ^{131}Xe time-constant data (see Figs. A.11 and A.12) are too large to allow us to make judgements on their overall temperature dependence. However, the higher-temperature uncoated-cell ^{131}Xe time constants do appear to be independent of cell temperature, perhaps indicating a balance between the competing effects of decreasing quadrupole and increasing dipole relaxation rates.

Since there were different amounts of xenon in the coated and uncoated cells, we

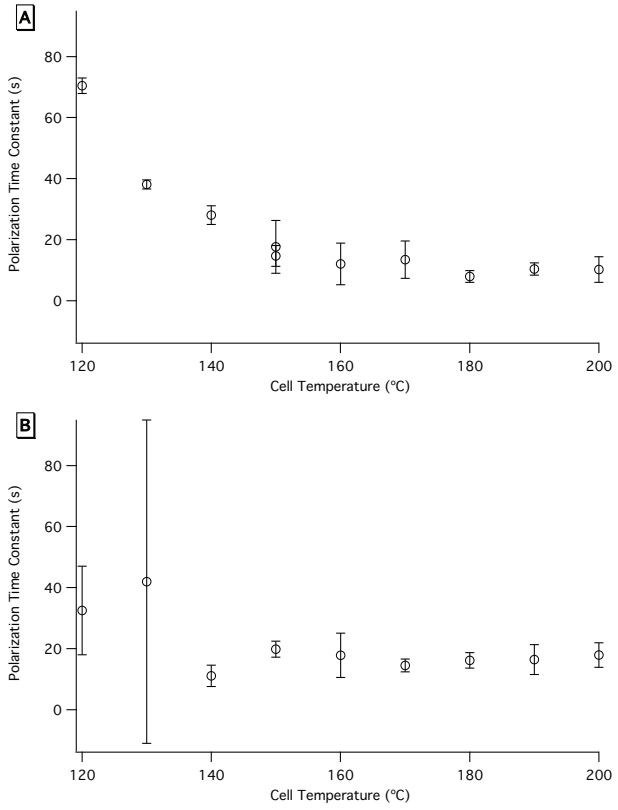

Figure A.12: The uncoated-cell ^{129}Xe (**A**) and ^{131}Xe (**B**) polarization time constants as a function of cell temperature.

cannot make a direct comparison of the ^{131}Xe peak heights in the two cell types to determine which cell type optimizes the achievable polarization for an isotope experiencing quadrupole relaxation. We thus normalize the ^{131}Xe peak heights to the ^{129}Xe values in each cell type, giving the results shown in Fig. A.13. Although there are large errors in some of the coated-cell points, the trends for the two sets of data indicate that the ^{131}Xe polarization signal in OTS-coated cells is larger relative to the ^{129}Xe signal than it is in an uncoated cell at the same temperature. Earlier work [Ros99] has demonstrated improved ^{129}Xe polarization in OTS-coated cells. Thus, our data indicates that, over the temperature range investigated, OTS-coatings improve the achievable polarization in isotopes experiencing quadrupole relaxation

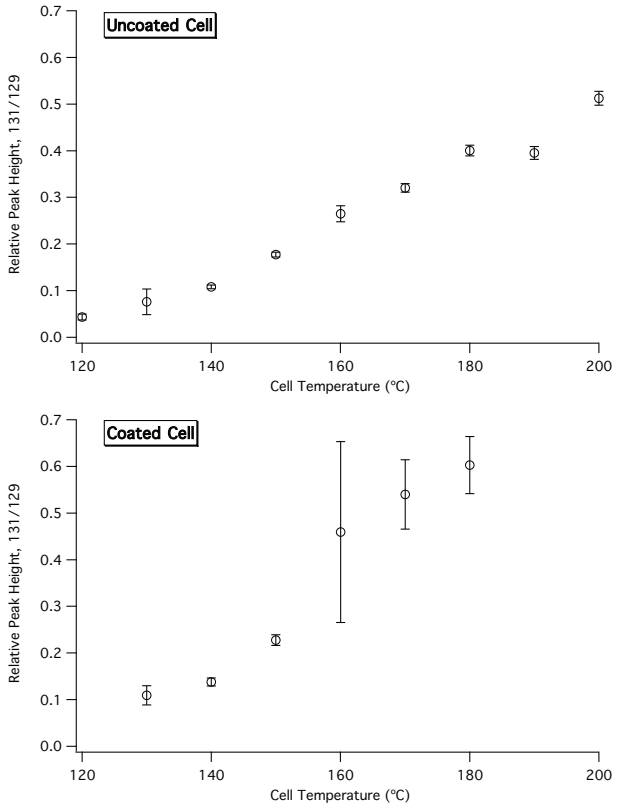

Figure A.13: The ratio of the ^{131}Xe peak height to that of ^{129}Xe as a function of temperature in the coated and uncoated cells.

mechanisms. Further work to more accurately measure the high-temperature coated-cell ^{131}Xe AFP signal would be necessary to determine an optimum cell temperature.

A.4 Conclusions from the Xenon AFP Measurements

We constructed a high-power narrow-band laser capable of maintaining a high rubidium polarization at higher temperatures than could the Coherent FAP system used in the ^{209}Rn measurements. Our measurements of the achievable ^{129}Xe and ^{131}Xe polarization signals in uncoated and OTS-coated optical pumping cells demonstrate an advantage in using cell coatings for isotopes sensitive to quadrupole relaxation mechanisms. These results are consistent with our observations of the

temperature dependence of the ^{209}Rn polarization, which showed no definitive evidence of turning over even up to cell temperatures of 220°C.

These results provide motivation for a more thorough study of natural xenon polarization in coated and uncoated cells. The lower power and wider bandwidth of the Coherent laser used in the ^{209}Rn measurements could lead one to expect that the polarization would turn over at a lower temperature than in the xenon/narrowed laser system. However, unlike in the ^{209}Rn measurements the amount of noble gas in the cells in the AFP studies was enough to have a significant effect on the rubidium spin destruction rate. Rubidium ESR measurements using the narrowed laser at a range of output powers could allow the model discussed in Chapter V to be tested more thoroughly. This would also allow the relation between the temperature dependences of the rubidium and ^{131}Xe polarizations to be investigated in detail, if the effect of the presence of xenon on the rubidium polarization can be experimentally measured.

With improvements to the experimental apparatus (especially pickup coils that will function at higher temperatures) it should be possible to determine at what cell temperature (for a given laser power) the ^{131}Xe polarization signal reaches its maximum. The use of a higher ratio of xenon to nitrogen in the cells could improve the signal strength considerably. We filled the cells with a smaller amount of xenon relative to the nitrogen than we had in the past since we were unable to observe a Rb ESR signal with 100 torr of natural xenon and 500 torr nitrogen. We observed that the coated cell, which was loaded with less xenon than the uncoated cell, had a barely detectable ESR signal while the uncoated cell had none. This could be due the increase in the spin-destruction collisions and widening of the rubidium hyperfine transitions caused by the presence of xenon, an effect that could be overcome by using the RF amplifier in the ESR measurements as well.

BIBLIOGRAPHY

BIBLIOGRAPHY

[Alc84] Alcock, C.B., Itkin, V.P., and Horrigan, M.K., *Vapour pressure equations for the metallic elements: 298-2500 K*, Can. Metal. Quart. **23** (1984), 309–313.

[And60] Anderson, L.W., Pipkin, F.M., and Baird, J.C., *Hyperfine Structure of Hydrogen, Deuterium, and Tritium*, Phys. Rev. **120** (1960), 1279–1289.

[And64] Andersson, G., Rudstam, R., and Sörensen, G., *Decay data on some Xe, I, and Te isotopes*, Ark. Fys. **28** (1964), 37–43.

[App98] Appelt, S. *et al.*, *Theory of spin-exchange optical pumping of* ^{3}*He and* ^{129}*Xe*, Phys. Rev. A **58** (1998), 1412–1439.

[Arc04] Archambault, J.P., Czarnecki, A., and Pospelov, M., *Electric dipole moments of leptons in the presence of Majorana neutrinos*, Phys. Rev. D **70** (2004), 073006.

[Bab05] Babcock, Earl D., *Spin-Exchange Optical Pumping with Alkali-Metal Vapors*, Ph.D. thesis, University of Wisconsin-Madison, 2005.

[Bar93] Barr, S.M., *A Review of CP Violation in Atoms*, Int. J. Mod. Phys. A **8** (1993), 209–236.

[Bar98] Baranga, A.B. *et al.*, *Polarization of* ^{3}*He by Spin Exchange with Optically Pumped Rb and K Vapors*, Phys. Rev. Lett. **80** (1998), 2801–2804.

[Blo40] Bloch, F. and Siegert, A., *Magnetic Resonace for Nonrotating Fields*, Phys. Rev. **57** (1940), 522–527.

[Bre00] Breeze, S.R. *et al.*, *Coatings for optical pumping cells and short-term storage of hyperpolarized xenon*, J. Appl. Phys. **87** (2000), 8013–8017.

[Cha02] Chann, B., Babcock, E., Anderson, L.W., and Walker, T.G., *Skew light propagation in optically thick optical pumping cells*, Phys. Rev. A **66** (2002), 033406.

[Cha05] Charles, J. *et al.*, *CP violation and the CKM matrix: assessing the impact of the asymmetric B factories*, Eur. Phys. J. C **41** (2005), 1–131.

[Cho91] Cho, D., Sangster, K., and Hinds, E.A., *Search for time-reversal-symmetry violation in thallium fluoride using a jet source*, Phys. Rev. A **44** (1991), 2783–2799.

[Chu90] Chupp, T.E., and Hoare, R.J., *Coherence in freely precessing* ^{21}*Ne and a test of linearity of quantum mechanics*, Phys. Rev. Lett. **64** (1990), 2261–2264.

[Coh] Coherent, Inc., *http://www.coherent.com/Lasers/*.

[Cre79] Crewther, R.J., Di Vecchia, P., Veneziano, G., and Witten, E., *Chiral estimate of the electric dipole moment of the neutron in quantum chromodynamics*, Phys. Lett. B **88** (1979), 123–127.

[Cre80] ———, *Chiral estimate of the electric dipole moment of the neutron in quantum chromodynamics [erratum]*, Phys. Lett. B **91** (1980), 487.

[Cro] Crown Audio, Inc., *http://www.crownaudio.com/index.htm*.

[CVI] CVI Melles Griot, *http://www.cvilaser.com*.

[Cza97] Czarnecki, A. and Krause, B., *Neutron Electric Dipole Moment in the Standard Model – Complete Three-Loop Calculation of the Valence Quark Contributions*, Phys. Rev. Lett. **78** (1997), 4339–4342.

[Dzu85] Dzuba, V.A., Flambaum, V.V., and Silvestrov, P.G., *Bounds on electric dipole moments and T-violating weak interactions of the nucleons*, Phys. Lett. B **154** (1985), 93–95.

[Edm] Edmund Optics Inc., *http://www.edmundoptics.com*.

[Eng00] Engel, J., Friar, J.L., and Hayes, A.C., *Nuclear octupole correlations and the enhancement of atomic time-reversal violation*, Phys. Rev. C **61** (2000), 035502.

[Fal99] Falk, T., Olive, K.A., Pospelov, M., and Roiban, R., *MSSM predictions for the electric dipole moment of the ^{199}Hg atom*, Nucl. Phys. B **560** (1999), 3–22.

[Fis92] Fischler, W., Paban, S. and Thomas, S., *Bounds on microscopic physics from P and T violation in atoms and molecules*, Phys. Lett. B **289** (1992), 373–380.

[Fla86] Flambaum, V.V., Khriplovich, I.B., and Sushkov, O.P., *On the P- and T-nonconserving nuclear moments*, Nucl. Phys. A **449** (1986), 750–760.

[Fla02] Flambaum, V.V. and Ginges, J.S.M., *Nuclear Schiff moment and time-reversal violation in atoms*, Phys. Rev. A **65** (2002), 032113.

[Fla03] Flambaum, V.V. and Zelevinsky, V.G., *Enhancement of nuclear Schiff moments and time-reversal violation in atoms due to soft nuclear octupole vibrations*, Phys. Rev. C **68** (2003), 035502.

[Gin04] Ginges, J.S.M. and Flambaum, V.V., *Violations of fundamental symmetries in atoms and tests of unification theories of elementary particles*, Phys. Rep. **397** (2004), 63–154.

[Gri09] Griffith, W.C., *et al.*, *Improved limit on the permanent electric dipole moment of ^{199}Hg*, arXiv:0901.2328 (2009).

[Hap72] Happer, W., *Optical Pumping*, Rev. Mod. Phys. **44** (1972), 169–250.

[Hap84] Happer, W. *et al.*, *Polarization of the nuclear spins of noble-gas atoms by spin exchange with optically pumped alkali-metal atoms*, Phys. Rev. A **29** (1984), 3092–3110.

[Har54] Hartogh, C.D., Tolhoek, H.A., and de Groot, S.R., *Some explicit formulae for the angular distribution and polarization of gamma radiation emitted by oriented nuclei*, Physica **20** (1954), 1310–1313.

[Har99] Harris, P.G. *et al.*, *New Experimental Limit on the Electric Dipole Moment of the Neutron*, Phys. Rev. Lett. **82** (1999), 904–907.

[Jac95] Jacobs, J.P. *et al.*, *Limit on the electric-dipole moment of ^{199}Hg using synchronous optical pumping*, Phys. Rev. A **52** (1995), 3521–3540.

[Kep] Kepco, Inc., *http://www.kepcopower.com*.

[Khr82] Khriplovich, I.B. and Zhitnitsky, A.R., *What is the value of the neutron electric dipole moment in the Kobayashi-Maskawa model?*, Phys. Lett. B **109** (1982), 490–492.

[Kit88] Kitano, M. *et al.*, *Nuclear Orientation of Radon Isotopes by Spin-Exchange Optical Pumping*, Phys. Rev. Lett. **60** (1988), 2133–2136.

[Mar08] Martin, S.P., *A Supersymmetry Primer*, arXiv:hep-ph/9709356v5, 2008.

[MDC] MDC Vacuum Products, LLC, *http://www.mdc-vacuum.com/*.

[Nat] National Instruments Corporation, *http://www.ni.com/*.

[nLi] nLight Corporation, *http://www.nlight.net*.

[Nus04] Nuss-Warren, S.R. *et al.*, *On-line collection and transfer of radioactive noble gas isotopes*, Nucl. Instrum. Meth. A **533** (2004), 275–281.

[Opt] OptiTemp Inc., *http://www.optitemp.com*.

[Pes95] Peskin, M.E., and Schroeder, D.V., *An Introduction to Quantum Field Theory*, Basic Books, 1995.

[Phi06] Phillips, A.A. *et al.*, *Half-life of* ^{120}Xe, Phys. Rev. C **74** (2006), 027302.

[Pos91] Pospelov, M.E. and Khriplovich, I.B., *Electric dipole moment of the W boson and the electron in the Kobayashi-Maskawa model*, Sov. J. Nucl. Phys. **53** (1991), 638.

[Pos94] Pospelov, M.E., *CP-odd effective gluonic Lagrangian in the Kobayashi-Maskawa model*, Phys. Lett. B **328** (1994), 441–449.

[Pos05] Pospelov, M. and Ritz, A., *Electric dipole moments as probes of new physics*, Ann. Phys. **318** (2005), 119–169.

[Pur50] Purcell, E.M., and Ramsey, N.F., *On the Possibility of Electric Dipole Moments for Elementary Particles and Nuclei*, Phys. Rev. **78** (1950), 807.

[Rad] Radford, David, *Radware, http://radware.phy.ornl.gov*.

[Reg02] Regan, B.C., Commins, E.D., Schmidt, C.J., and DeMille, D., *New Limit on the Electron Electric Dipole Moment*, Phys. Rev. Lett. **88** (2002), 071805.

[Rom01] Romalis, M.V., Griffith, W.C., Jacobs, J.P., and Forston, E.N., *New Limit on the Permanent Electric Dipole Moment of* ^{199}Hg, Phys. Rev. Lett. **86** (2001), 2505–2508.

[Ros99] Rosen, M.S. *et al.*, *Polarized* ^{129}Xe *optical pumping/spin exchange and delivery system for magnetic resonance spectroscopy and imaging studies*, Rev. Sci. Instrum. **70** (1999), 1546–1552.

[Ros01] Rosenberry, M.A. and Chupp, T.E., *Atomic Electric Dipole Moment Measurement Using Spin Exchange Pumped Masers of* ^{129}Xe *and* ^{3}He, Phys. Rev. Lett. **86** (2001), 22–25.

[Sak67] Sakharov, A.D., *Violation of CP invariance, C asymmetry, and baryon asymmetry of the universe*, JETP Lett. **5** (1967), 24–27.

[Sak91] ———, *Violation of CP invariance, C asymmetry, and baryon asymmetry of the universe [reprint]*, Sov. Phys. Usp. **34** (1991), 392–393.

[Sch63] Schiff, L.I., *Measurability of Nuclear Electric Dipole Moments*, Phys. Rev. **132** (1963), 2194–2200.

[Sha78] Shabalin, E.P., *Electric dipole moment of the quark in a gauge theory with left-handed currents*, Sov. J. Nucl. Phys. **28** (1978), 75–77.

[Shi96] V.S. Shirley (ed.), *Table of Isotopes, 8th edition*, John Wiley & Sons, Inc., New York, 1996.

[Smi98] Smith, Todd B., *A Precision Measurement of the Neutron Spin Structure Functions Using a Polarized* ^{3}He *Target*, Ph.D. thesis, The University of Michigan, 1998.

[Spe97] Spevak, V., Auerbach, N., and Flambaum, V.V., *Enhanced T-odd, P-odd electromagnetic moments in reflection asymmetric nuclei*, Phys. Rev. C **56** (1997), 1357–1369.

[Sta] Stanford Research Systems, *http://www.thinksrs.com/*.

[Sve05] Svensson, C.E. *et al.*, *TIGRESS: TRIUMF-ISAC gamma-ray escape-suppressed spectrometer*, J. Phys. G: Nucl. Part. Phys. **31** (2005), S1663–S1668.

[Swa] Swagelok Company, The, *http://www.swagelok.com*.

[TDK] TDK-Lambda Americas Inc., *http://www.lambda.com*.

[Tho] Thorlabs, *http://www.thorlabs.com*.

[Wag89] Wagshul, M.E. and Chupp, T.E., *Optical pumping of high-density Rb with a broadband dye laser*, Phys. Rev. A **40** (1989), 4447–4454.

[Wag91] Wagshul, Mark Elliot, *Polarization of ^{3}He by Spin Exchange with High Density Laser Optically Pumped Rb Vapor*, Ph.D. thesis, Harvard University, 1991.

[Wal89] Walker, T.G., *Estimates of spin-exchange parameters for alkali-metal–noble-gas pairs*, Phys. Rev. A **40** (1989), 4959–4964.

[Wal97] Walker, T.G. and Happer, W., *Spin-exchange optical pumping of noble-gas nuclei*, Rev. Mod. Phys. **69** (1997), 629–642.

[War05] Warner, T. *et al.*, *Diffusion of Xe in Ta, Zr, and Pt*, Nucl. Instrum. Meth. A **538** (2005), 135–142.

[Wei89] Weinberg, S., *Larger Higgs-Boson-Exchange Terms in the Neutron Electric Dipole Moment*, Phys. Rev. Lett. **63** (1989), 2333–2336.

[Wu90] Wu, Zhen *et al.*, *Experimental studies of wall interactions of adsorbed spin-polarized ^{131}Xe nuclei*, Phys. Rev. A **42** (1990), 2774–2784.